
Open and Reduced Wilson Chains for Quantum Impurity Models

Master's Thesis
Nils-Oliver Linden

Chair of Theoretical Solid State Physics
Faculty of Physics
Ludwig-Maximilians-University Munich



Supervisors:

Prof. Dr. Jan von Delft and PD Dr. Andreas Weichselbaum

September 22, 2014

Contents

1	Introduction	1
2	Numerical Methods	3
2.1	Matrix Product States	3
2.1.1	Global and local picture	4
2.1.2	Update formalism	5
2.1.3	Reduced density matrix	6
2.2	Bosonic Numerical Renormalization Group	7
2.2.1	Spin-boson model	8
2.2.2	Logarithmic discretization	8
2.2.3	The chain-Hamiltonian	10
2.2.4	NRG iteration	10
2.2.5	Energy-level flow diagrams	12
2.2.6	The limitation of bosonic NRG	12
2.3	Variational Matrix Product State	14
2.3.1	Variational optimization scheme	14
2.3.2	Truncation and convergence	16
2.3.3	Optimal bosonic basis and variational shift	16
2.3.4	Analytic shift	18
2.3.5	Energy-level flow diagrams	19
2.3.6	Variational calculation of m lowest eigenstates	20
3	Open Wilson Chains	25
3.1	Iterative construction of an OWC	25
3.2	General implementation	28
4	Applications	30
4.1	Dissipative harmonic oscillator	30
4.1.1	Determination of critical coupling	30
4.1.2	Iteration details	31
4.1.3	Susceptibility calculation	34
4.1.4	Exact diagonalization	37
4.1.5	Calculation of the occupation number	40
4.1.6	Energy-level flow diagrams	42
4.2	Spin-boson model	46
4.2.1	Ground state phases	46
4.2.2	Determining the critical coupling strength	48
4.2.3	Critical exponents	50
4.2.4	Determination of ν with spin-projected displacements	52
4.2.5	Susceptibility calculation	54
5	Conclusion	58

CONTENTS

II

A	Appendices	60
A	NRG and RWCs	60
B	Critical exponents SBM	61
B.1	β	61
B.2	δ	62
B.3	ν	63
B.4	x	64
	List of Figures	65
	References	67

1 Introduction

The invention of quantum mechanics in the beginning of the last century has started one of the biggest changes of human life in modern history. It led to new types of microscopes, expanding the frontier of research to unexpected small scales and an exciting understanding of biological and chemical processes, and it was the foundation of the technological progress which resulted in society changing inventions such as the laser or the personal computer. Nowadays, the ongoing technological development causes electronic devices of our every day life being manufactured on the scale of nanometers. The same holds true for biological and chemical systems, which are investigated and manipulated on increasingly small length-scales. To understand and use the occurring physics of these systems, it becomes increasingly important to understand how solid state systems behave on a quantum mechanical scale when interacting with their surroundings.

To describe such systems with only a few degrees of freedom coupled to an environment with generally infinite number of degrees of freedom in theoretical physics, one resorts on so-called quantum impurity models. In such models, the environment is represented by a non-interacting bath consisting optionally of fermionic (e.g. the Kondo-model [1, 2]) or bosonic particles (e.g. spin-boson model [3, 4]) allowing to describe charged or non-charged environments.

However, only few quantum impurity models can be solved exactly due to the large number of degrees of freedom of the environment. In addition, describing such situations theoretically in terms of perturbation theories can fail to capture all physical properties since multiple energy scales can become important. Nowadays, the preferred methods to fully investigate the characteristics of such models are numerical schemes such as the Numerical Renormalization Group (NRG) [5, 6] and the Density Matrix Renormalization Group (DMRG) [7, 8].

In 1987 first introduced by Leggett [3], the spin-boson model came into focus because it is the easiest non-trivial quantum impurity model with a bosonic environment that can not be solved exactly. Nevertheless, this model poses a huge challenge to both numerical and analytical approaches, especially towards the understanding of the critical properties. The first numerical results investigating its critical phenomena were contradictory and lead to huge discussions in the scientific community. Although the outcome of bosonic NRG suggested a failure of quantum-to-classical correspondence [9, 10, 11], an analytic technique describing the quantum phase transition of the spin-boson model by mapping it onto the classical one-dimensional Ising chain, other numerical schemes confirmed its validity [12, 13, 14]. Until now, NRG and DMRG are not able to completely capture the physical behavior of the spin-boson model. More recent results showed that the reason seems to be the way the continuous bath modes are treated numerically [15], resulting in an incorrect description of thermal critical properties and implying wrong numerical predictions for bosonic impurity models in certain parameter regimes in the phase diagram.

Motivated by this conceptual problem, we present an alternative way of setting up the starting point of NRG or DMRG calculations, which allows us to keep track of all important quantities of the environment. We discuss how to implement the information

of these so-called "open Wilson chains" and verify that this approach leads to results in agreement with the theoretical predictions for the spin-boson model and the dissipative harmonic oscillator.

This thesis is structured as follows: In chapter 2 we start introducing the matrix product state formalism and then give an overview over bosonic NRG and DMRG, where the usage of open Wilson chains plays a crucial role to describe the investigated system correctly. Both methods are used in this thesis to obtain the numerical results.

In the beginning of chapter 3, we concentrate on the iterative construction of an open Wilson chain and show that we can keep track of all relevant quantities of the model when carrying out this construction. In the end of the chapter, we discuss a proper implementation of an open Wilson chain within NRG and DMRG, the so-called "reduced Wilson chains".

Using reduced Wilson chains, we investigate the dissipative harmonic oscillator (DHO) and the spin-boson model (SBM) in chapter 4. We show that the critical finite-temperature susceptibility of the DHO and SBM are now, in contrast to previous results, in agreement with theoretical predictions. Additionally, we take a look at the energy-flow diagram of the DHO and compare results obtained by diagonalizing the Hamiltonian exactly with results obtained with VMPS when optimizing not only the ground state but the m lowest levels.

In the last chapter 5, we summarize the main results of this thesis and give an outlook on possible topics for future research and improvements of the presented methods.

2 Numerical Methods

In this chapter, we introduce two numerical methods used to study quantum impurity models, which are the basic methods in this thesis: the Numerical Renormalization Group (NRG) [5, 6] and the Density Matrix Renormalization Group (DMRG) [7, 8]. Both methods can be formulated in terms of Matrix Product States (MPS) which lead to a deeper understanding of the methodology and modifications, hard to develop in the conventional framework [16, 17, 18].

This section is based on more extensive reviews on the topic [17, 19] without covering every detail and giving derivations. We first summarize the most important properties of MPS, focusing on applications to bosonic systems only. Afterwards, we discuss bosonic NRG [9, 20] and DMRG, pointing out the crucial differences [14] between these two methods.

2.1 Matrix Product States

The starting point of our introduction is an one-dimensional chain consisting of N equal sites with local and nearest-neighbor interaction only. On each site we have a local Hilbert space with dimension d and thus a total Hilbert space \mathcal{H} describing the whole system of dimension $\dim(\mathcal{H}) = d^N$. A generic quantum many body state $|\psi\rangle$ in \mathcal{H} can be written as

$$|\psi\rangle = \sum_{n_1 \dots n_N} \psi_{n_1 \dots n_N} |n_1\rangle \dots |n_N\rangle, \quad (2.1)$$

where $n_i = 1, \dots, d$ labels the local basis states of site i . By decomposing and reorganizing the coefficients in Eq. (2.1), we can write a quantum many body state as a product of matrices $A^{[n_k]}$

$$|\psi\rangle = \sum_{n_1 \dots n_N} A^{[n_1]} A^{[n_2]} \dots A^{[n_N]} |n_1\rangle \dots |n_N\rangle. \quad (2.2)$$

In doing so, $|\psi\rangle$ consists of $N \times d$ so-called A -tensors, because each of the d local states n_k on every site is described by one matrix $A^{[n_k]}$. Since we consider a chain with open boundaries, the first index of $A^{[n_1]}$ and the second index of $A^{[n_N]}$ are equal to one. Therefore $A^{[n_1]}$ and $A^{[n_N]}$ are normal row and column matrices.

If the dimension of the A -tensors is sufficiently large, the representation of $|\psi\rangle$ into an MPS is mathematically exact. However, an exact representation often is numerically not feasible but fortunately also not necessary. Even if we truncate the A -tensors with respect to some upper cutoff dimension D , we still can find a very good approximation of the ground state in one-dimensional systems. Since the entanglement entropy of the ground state scales according to an area law [21, 22, 23], which in case of of a one-dimensional chain with short-ranged interaction and a gapped spectrum predicts an even constant entropy, we only need a small partition of the total Hilbert space to describe the ground state accurately.

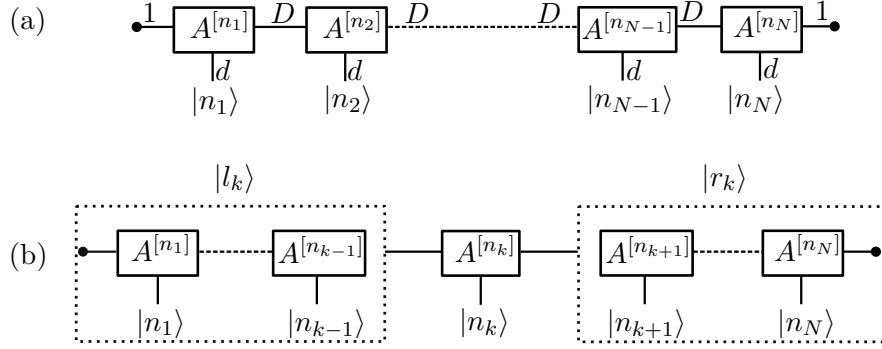


Figure 1: (a) Graphical representation of a matrix product state in the global picture. Every A -tensor $A^{[n_k]}$ describes the contribution of one local basis set $|n_k\rangle$, constituting of d elements, to the described state $|\psi\rangle$. The upper cutoff dimension D truncates the dimension of the indices connecting the A -tensors. The left index of $A^{[n_1]}$ and the right index of $A^{[n_N]}$ connect the state to the vacuum (indicated by a circle) which has by construction dimension one. (b) Matrix product state in the local picture, where site k is treated specially. All A -tensors to the left of site k are combined to an effective left basis $|l_k\rangle$. Similarly, the part of the MPS right of site k is described by the effective basis $|r_k\rangle$.

2.1.1 Global and local picture

If a matrix product state is written in the form of Eq. (2.2), where the state is stored in the A -tensors and described as product of the local Hilbert spaces, we speak of a MPS in the global picture. In this picture all sites are treated equally.

An alternative, yet equivalent way to depict a MPS is the so-called local picture, where one specific site is chosen as local site and all other sites are combined to effective basis sets $|l_k\rangle$ and $|r_k\rangle$ for the left and right part of the chain with respect to the local site k . The MPS state than can be written as

$$|\psi\rangle = \sum_{l_k r_k n_k} A_{l_k, r_k}^{[n_k]} |l_k\rangle |n_k\rangle |r_k\rangle, \quad (2.3)$$

where

$$|l_k\rangle = \sum_{n_1 \dots n_{k-1}} \left(A^{[n_1]} \dots A^{[n_{k-1}]} \right)_{l_k} |n_1\rangle \dots |n_{k-1}\rangle, \quad (2.4)$$

and

$$|r_k\rangle = \sum_{n_{k+1} \dots n_N} \left(A^{[n_{k+1}]} \dots A^{[n_N]} \right)_{r_k} |n_{k+1}\rangle \dots |n_N\rangle. \quad (2.5)$$

The A -tensor $A^{[n_k]}$ describes the complete state as linear combination of the orthonormal many-body basis sets $|l_k\rangle$, $|r_k\rangle$ and $|n_k\rangle$. In Fig. 1, the difference between the local and global picture is presented graphically.

This definition in mind, Eq. (2.4) and Eq. (2.5) can be reformulated to yield an iterative construction of the effective basis sets in terms of A -tensors and local state

spaces

$$\begin{aligned}
|l_k\rangle &= \sum_{n_{k-1}} \sum_{l_{k-1}} \underbrace{\sum_{n_1 \dots n_{k-2}} \left(A^{[n_1]} \dots A^{[n_{k-2}]} \right)_{l_{k-1}} |n_1\rangle \dots |n_{k-2}\rangle}_{|l_{k-1}\rangle} A_{l_{k-1}, l_k}^{[n_{k-1}]} |n_{k-1}\rangle \\
&= \sum_{n_{k-1}} \sum_{l_{k-1}} A_{l_{k-1}, l_k}^{[n_{k-1}]} |l_{k-1}\rangle |n_{k-1}\rangle, \tag{2.6}
\end{aligned}$$

and

$$|r_k\rangle = \sum_{n_{k+1}} \sum_{r_{k+1}} A_{r_k, r_{k+1}}^{[n_{k+1}]} |r_{k+1}\rangle |n_{k+1}\rangle. \tag{2.7}$$

Usually, numerical schemes such as NRG or DMRG strongly exploit the resulting orthonormality conditions we derive in the next section and treat every site of the chain iteratively in the local picture. For this case, Eqs. (2.6) and (2.7) provide the update formalism toward the next nearest neighbor.

2.1.2 Update formalism

In principle, only the local basis states $|n_k\rangle$ in Eq. (2.3) form an orthonormal basis but every state ψ can be transformed such that the effective basis sets also obey orthonormality conditions

$$\langle l_k | l'_k \rangle = \delta_{l, l'} \tag{2.8}$$

$$\langle r_k | r'_k \rangle = \delta_{r, r'}. \tag{2.9}$$

Applying the orthonormality conditions on Eqs. (2.6) and (2.7), it follows immediately that the A -tensors have to fulfill the following conditions

$$\sum_{n_i} A^{[n_i] \dagger} A^{[n_i]} = \mathbb{1} \text{ if } i < k \tag{2.10}$$

$$\sum_{n_i} A^{[n_i]} A^{[n_i] \dagger} = \mathbb{1} \text{ if } i > k. \tag{2.11}$$

If we now assume that a given state $|\psi\rangle$ in the local picture at site k has an orthonormal effective basis set $|l_k\rangle$, then we can switch the local site to $k+1$ by performing a singular value decomposition (SVD) of the tensor $A^{[n_k]}$

$$\begin{aligned}
A^{[n_k]} A^{[n_{k+1}]} &= \sum_i A_{l_k, i}^{[n_k]} A_{i, r_{k+1}}^{[n_{k+1}]} = \sum_i A_{(l_k n_k), i} A_{i, r_{k+1}}^{[n_{k+1}]} \\
&= \sum_{i, m} U_{(l_k n_k), m} \left[(S V^\dagger)_{m, i} A_{i, r_{k+1}}^{[n_k]} \right] = \tilde{A}^{[n_k]} \tilde{A}^{[n_{k+1}]}. \tag{2.12}
\end{aligned}$$

The SVD decomposes the A -tensor in the column-orthonormal U and V matrices and the diagonal matrix S consisting of real elements s_i called singular values. Therefore, U fulfills automatically the orthonormality condition Eq. (2.10) and can be interpreted as the new A -tensor $\tilde{A}^{[n_k]}$ which forms with Eq. (2.6) the new orthonormal effective

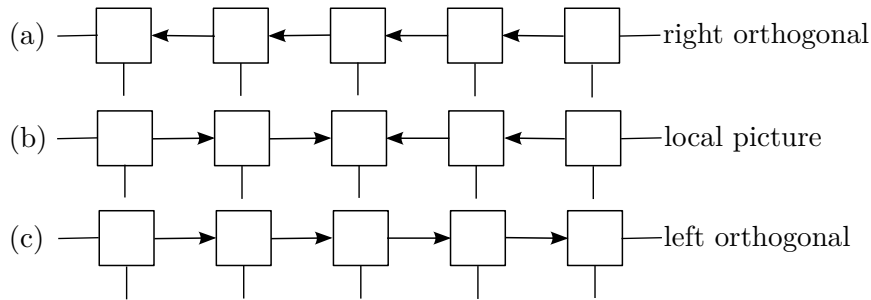


Figure 2: (a) MPS in right orthogonal form, obtained by performing a number of singular value decompositions, starting on the right end of the MPS and moving to the left end. The arrows indicate in which direction a contraction with the conjugate A -tensor yields the identity matrix according to the orthonormalization condition Eq. (2.10) and Eq. (2.11). Performing a number of singular value decompositions on the left end of the chain and moving to the right constructs a MPS in the local picture of an arbitrary site (b). Arriving at the end of the chain in this way, we construct a left orthogonal MPS (c).

basis set $|l_{k+1}\rangle$. SV^\dagger contracted onto $A^{[n_{k+1}]}$ yields the A -tensor $\tilde{A}^{[n_{k+1}]}$ of the new local site $k+1$. Note that the overall state $|\psi\rangle$ does not change when all singular values are kept. Applying this scheme iteratively starting at site 1, which by construction has the orthonormal vacuum state as left basis, we construct a *left-canonical* MPS.

In the same way, we can generate a right-canonical MPS with orthonormalized right basis set, starting at site N where the right basis is the orthonormal vacuum state by construction and sweeping to the left, as illustrated in Fig. 2.

2.1.3 Reduced density matrix

We already mentioned in this chapter that finding the exact ground state of a many-body system is not feasible from a numerical point of view because of the large Hilbert space \mathcal{H} . Nevertheless, for most cases finding a very good approximation is possible. This can be explained via the von-Neumann entropy, indicating the entanglement of the system

$$S(\rho^{red}) = -\text{tr}(\rho^{red} \ln(\rho^{red})) , \quad (2.13)$$

with ρ^{red} the reduced density matrix of a subsystem (i.e. a part of the chain). In contrast to a generic many-body state, where the entanglement and with it the size of the coefficient space ψ scales with the system size, the entropy of the ground state scales according to an area law [21, 22, 23]. In case of an one-dimensional chain with short-ranged interaction and a gapped spectrum, the entropy stays constant with increasing system size. Therefore, only a small part of the total Hilbert space is necessary to describe the ground state accurately. To use this fact, we start again in the local picture of site k and calculate the reduced density matrix $\rho_k^{red} = \rho_{n_1 \dots n_k}^l = \text{tr}_{r_k} |\psi\rangle\langle\psi|$. Using the orthonormality conditions in the local picture, we can write the reduced

density matrix as

$$\begin{aligned} \rho_k^{red} &= \sum_{n_1 \dots n_k} \sum_{n'_1 \dots n'_k} \left(A^{[n_1]} \dots A^{[n_k]} \right)^* \left(A^{[n_1]} \dots A^{[n_k]} \right) |n_1\rangle \langle n'_1| \dots |n_k\rangle \langle n'_k| \\ &= \sum_{ll'} \rho_{ll'} |l_{k+1}\rangle \langle l'_{k+1}|, \end{aligned} \quad (2.14)$$

and see that only its spectrum quantifies the entanglement of the left and right part of the chain at site k . If the spectrum is distributed equally, the von-Neumann entropy S is high, indicating a strongly entangled left and right part of the chain. On the other hand, one dominant eigenvalue implies a small von-Neumann entropy, i.e. an almost disentangled state. DMRG uses this fact as a truncation criterion by discarding the smallest eigenvalues of ρ_k^{red} and the corresponding state space, thus truncating only those parts of the Hilbertspace which are the less relevant for a accurate description of the ground state. Because of the orthonormality conditions, the spectrum of the reduced density matrix is equivalent to the squared singular values obtained by a SVD of $A^{[n_k]}$. This allows an effective combination of the truncation of the Hilbertspace with the update formalism when moving from one local site to the next via a systematic use of SVD [17].

2.2 Bosonic Numerical Renormalization Group

The Numerical Renormalization Group (NRG) was developed in the 1970s by Kenneth Wilson [5, 24] and proved to be a powerful numerical method for treating fermionic quantum impurity models. Its non-perturbative character allows the treatment of interacting quantum many-body systems with a continuum of excitations with energies spread over many orders of magnitude. This is one of its major advantages and has been used on numerous quantum impurity models, e.g. answering many questions regarding transport, dissipation or Kondo physics [25, 26, 27, 28, 29].

The only major restriction for the applicability of NRG is the assumption of non-interacting baths or reservoirs the impurity is coupled to, while many-body interactions affect only the impurity. However, there are no further constrains on the baths which can consists of bosonic or fermionic particles.

Bulla et al. [9] applied NRG 2003 for the first time to a bosonic model in order to calculate the critical properties of the spin-boson model. Prior to that, NRG was only applied to fermionic systems such as the single impurity Anderson model because bosonic baths are more challenging to treat numerically than fermionic ones and contain problems hard to deal with. Due to Pauli's principle, the local fermionic Hilbert spaces stay finite and small because two fermions are restricted from occupying the same state. However, such constraints do not exist for bosons, which can occupy a state infinitely often yielding infinitely large Hilbert spaces that are more challenging for numerical approaches.

Since we only consider bosonic quantum impurity models in this thesis, we introduce NRG in the context of bosonic baths only following the description in [20]. First, we describe the basic steps of the NRG algorithm, after which we discuss the connection between NRG and MPS [16]. We close this section by pointing out the main problem

of bosonic NRG [30] which lead directly to the method of Variational Matrix Product States (VMPS).

2.2.1 Spin-boson model

Since the focus of this thesis is on the SBM and the dissipative harmonic oscillator, we introduce bosonic NRG based on the spin-boson model, its first application. For the conceptual understanding of NRG we only need to introduce the basic properties of the model in this chapter. We will give a more detailed discussion on physical properties in chapter 4. The starting point is the continuous version of the spin-boson model Hamiltonian

$$\hat{H} = \underbrace{\frac{\epsilon}{2}\hat{\sigma}_x - \frac{\Delta}{2}\hat{\sigma}_z}_{\hat{H}_{imp}} + \underbrace{\sum_i \omega_i \hat{a}_i^\dagger \hat{a}_i}_{\hat{H}_{bath}} + \underbrace{\frac{\hat{\sigma}_z}{2} \sum_i \lambda_i (\hat{a}_i + \hat{a}_i^\dagger)}_{\hat{H}_{coupling}}, \quad (2.15)$$

where the impurity is a two state system with energy difference ϵ and tunneling amplitude Δ . The impurity is fully described by the Pauli matrices $\hat{\sigma}_x$ and $\hat{\sigma}_z$ and coupled via the last term with the bosonic bath. Each oscillator is coupled linearly with strength λ_i to the impurity spin. Thus, the effect of the bath on the impurity can be completely described by the bath spectral function

$$\Gamma(\omega) = \pi \sum_i \lambda_i^2 \delta(\omega - \omega_i), \quad (2.16)$$

consisting of the density of states in the bath $\rho(\omega) = \pi \sum_i \delta(\omega - \omega_i)$ and the coupling strength λ_i . For the study of the low-temperature properties, only the low-energy spectrum of the bath is important. Therefore a cutoff frequency ω_c is introduced and the spectrum above neglected, whereas the spectrum below is parametrized by a power law

$$\Gamma(\omega) = 2\pi\alpha\omega_c^{1-s}\omega^s, \quad 0 < \omega < \omega_c, \quad s > 0. \quad (2.17)$$

The dimensionless constant α describes the dissipation strength of the system and the bath exponent s distinguish between the *ohmic* ($s = 0$), *sub-ohmic* ($s < 1$) and *super-ohmic* ($s > 1$) dissipation, indicating different qualitative behavior. Typically, the cutoff frequency ω_c is set equal to one (also in this thesis).

2.2.2 Logarithmic discretization

Since the bath consists of an infinite number of oscillators, we need to discretize the system to make it numerically accessible. In the case of NRG, the discretization scheme must fulfill some crucial requirements. On the one hand, the physics of many quantum impurity models is influenced by exponentially small energy scales, therefore a high low-energy resolution is required. On the other hand, the discretization should separate consecutive energy intervals to enable a controlled numerical treatment within the iterative diagonalization procedure of NRG. A logarithmic discretization can meet both requirements and is therefore the method of first choice.

To discuss the discretization procedure, we start with the continuous version of Eq. (2.15) by replacing the discrete sum over frequencies by an integral over the energy variable ϵ

$$\hat{H} = \hat{H}_{imp} + \int d\epsilon (\epsilon \hat{a}_\epsilon^\dagger \hat{a}_\epsilon) + \frac{\hat{\sigma}_z}{2} \int d\epsilon \sqrt{\rho(\epsilon)} \lambda(\epsilon) (\hat{a}_\epsilon + \hat{a}_\epsilon^\dagger). \quad (2.18)$$

Here we introduce the new operators $\hat{a}_\epsilon = \sqrt{\rho(\epsilon)} \hat{a}_i$ as well as the density of states $\rho(\epsilon)$ and the coupling function $\lambda(\epsilon)$ which are related to the spectral function via

$$\frac{1}{\pi} \Gamma(\omega) = \rho(\epsilon(\omega)) |\lambda(\epsilon(\omega))|^2. \quad (2.19)$$

In contrast to fermionic baths, where the spectral function $\Gamma(\omega)$ is defined in general for positive (e.g. electrons) and negative frequencies (e.g. holes), the bosonic spectral function is restricted to positive frequencies in the interval $[0, \omega_c = 1]$ only. We define the dimensionless parameter $\Lambda > 1$ and divide the spectral function into intervals χ_k , whose boundaries are determined by $\omega_k = \Lambda^{-k}$ (see Fig. 3(a)), where $k \in \{0, 1, 2, \dots\}$. In each of the intervals we define a complete set of orthonormal functions

$$\Psi_{kp}(\epsilon) = \frac{1}{\sqrt{d_k}} e^{i\omega_k p \epsilon} \chi_k(\epsilon), \quad (2.20)$$

with $p \in \mathbb{N}$, $\omega_k = 2\pi/d_k$ and d_k the width of the interval given by $d_k = \Lambda^{-k}(1 - \Lambda^{-1})$. χ is the characteristic function of the respective interval

$$\chi_k(\epsilon) = \begin{cases} 1 & \text{if } \Lambda^{-(k+1)} < \epsilon < \Lambda^{-k} \\ 0 & \text{else} \end{cases}. \quad (2.21)$$

The annihilation and creation operators \hat{a}_ϵ and \hat{a}_ϵ^\dagger can be expanded in this basis corresponding to a Fourier expansion in each interval

$$\hat{a}_\epsilon = \sum_{kp} \hat{a}_{kp} \Psi_{kp}(\epsilon) \quad (2.22)$$

$$\hat{a}_\epsilon^\dagger = \sum_{kp} \hat{a}_{kp}^\dagger \Psi_{kp}^*(\epsilon) \quad (2.23)$$

Similar to the fermionic case, we impose that the impurity couples to the $p = 0$ component of the bosonic operators \hat{a}_{kp} and \hat{a}_{kp}^\dagger only. The other components $p \neq 0$ are still present through their coupling to the $p = 0$ component of the free bath. In the following step we define

$$\hat{a}_k = \frac{1}{\sqrt{N_k^2}} \int \sqrt{\frac{\Gamma(\epsilon)}{\pi}} \hat{a}_{k0} \Psi_{k0} d\epsilon \quad (2.24)$$

$$\hat{a}_k^\dagger = \frac{1}{\sqrt{N_k^2}} \int \sqrt{\frac{\Gamma(\epsilon)}{\pi}} \hat{a}_{k0}^\dagger \Psi_{k0}^* d\epsilon, \quad (2.25)$$

with N_k being a normalization constant such that the relation $[\hat{a}_k, \hat{a}_k^\dagger] = \delta_{k,k'}$ still holds

$$N_k^2 = \int_{\Lambda^{-(k+1)}}^{\Lambda^{-k}} \frac{\Gamma(\epsilon)}{\pi} d\epsilon . \quad (2.26)$$

Using the relations for \hat{a}_k and \hat{a}_k^\dagger in the continuous spin-boson Hamiltonian Eq. (2.18), we receive the discretized Hamiltonian (see Fig. 3(b)) in the *star*-geometry

$$\hat{H}_{star} = \hat{H}_{imp} + \sum_k \zeta_k \hat{a}_k^\dagger \hat{a}_k + \frac{\hat{\sigma}_z}{2\sqrt{\pi}} \sum_k \gamma_k (\hat{a}_k + \hat{a}_k^\dagger), \quad (2.27)$$

where the impurity is coupled linearly to all bosonic degrees of freedom, similar as the original Hamiltonian but with a discrete spectral function consisting of δ -peaks at energies ζ_k with weight γ_k^2 obtained from the bath spectral function Eq. (2.17)

$$\gamma_k^2 = \int_{\Lambda^{-k}}^{\Lambda^{-(k+1)}} d\omega \Gamma(\omega) = \frac{2\pi\alpha}{s+1} \omega_c^2 \left(1 - \Lambda^{-(s+1)}\right) \Lambda^{-k(s+1)} \quad (2.28)$$

$$\zeta_k = \frac{1}{\gamma_k^2} \int_{\Lambda^{-k}}^{\Lambda^{-(k+1)}} d\omega \omega \Gamma(\omega) = \frac{s+1}{s+2} \frac{1 - \Lambda^{-(s+2)}}{1 - \Lambda^{-(s+1)}} \omega_c \Lambda^{-k} . \quad (2.29)$$

From the proposed definition it is clear that every discrete bosonic degree of freedom in the star-Hamiltonian essentially represents the continuous spectrum of bosonic degrees of freedom in its energy interval.

2.2.3 The chain-Hamiltonian

The next step in standard NRG is the unitary transformation of the discretized star-Hamiltonian onto a semi-infinite chain with nearest-neighbor interaction only. Numerically, this is best achieved by a standard tridiagonalization procedure (e.g. Lanczos algorithm). In the resulting chain-Hamiltonian

$$\hat{H}_{chain} = \hat{H}_{imp} + \sqrt{\frac{\eta_0}{\pi}} \frac{\hat{\sigma}_z}{2} (\hat{b}_0 + \hat{b}_0^\dagger) + \sum_{k=0}^{\infty} \left[\epsilon_k \hat{b}_k^\dagger \hat{b}_k + t_k (\hat{b}_k^\dagger \hat{b}_{k+1} + \hat{b}_{k+1}^\dagger \hat{b}_k) \right] , \quad (2.30)$$

we define $\hat{b}_k = \sum_{m=0}^{\infty} U_{km} \hat{a}_m$, obtained from the unitary transformation U , and $\eta_0 = \int \Gamma(\omega) d\omega$ describing the overall coupling between bath and impurity. On this so-called Wilson chain, the impurity is located on the very first site and coupled only to one bosonic site, as illustrated in Fig. 3(c). Every site has an on-site energy ϵ_k and a hopping amplitude t_k which decay exponentially as Λ^{-k} and depend only on the spectral function $\Gamma(\omega)$. For the fermionic case, the approach works in a similar way resulting in hopping elements and on-site energies decaying with $\Lambda^{-\frac{k}{2}}$ because the spectral function is also defined for negative frequencies.

2.2.4 NRG iteration

The crucial idea of NRG is to solve the model iteratively by diagonalizing a series of Hamiltonians \hat{H}_N which in the limit $N \rightarrow \infty$ converge to the \hat{H}_{chain}

$$\hat{H}_{chain} = \lim_{N \rightarrow \infty} \Lambda^{-N} \hat{H}_N . \quad (2.31)$$

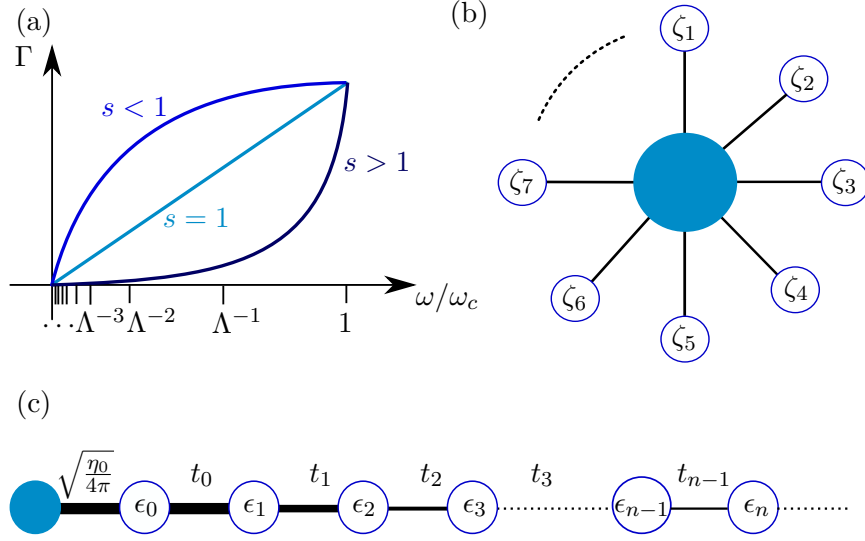


Figure 3: (a) Parametrized spectral function Γ of the spin-boson model in the super-ohmic ($s > 1$), ohmic ($s = 1$) and sub-ohmic ($s < 1$) case up to the cutoff frequency ω_c . The exponent s determines the number of states near $\omega = 0$. The logarithmic discretization ($\Lambda > 1$) generates the star-Hamiltonian illustrated in (b). The impurity is coupled linearly to an infinite number of discrete degrees of freedom. Mathematically, this can be mapped exactly to a semi-infinite chain with nearest-neighbor interaction only, where the impurity sits on the first site and couples only to the first bosonic site $k = 0$ (c). Because of the logarithmic discretization of Γ , both coupling strength t_k and on-site energies ϵ_k decrease exponentially with Λ . This is indicated by the thickness of the lines connecting the different sites.

Each Hamiltonian \hat{H}_N consists of $N + 2$ sites and is rescaled by Λ^N to improve the resolution of the the low-energy spectrum. From the form of \hat{H}_N

$$\hat{H}_N = \Lambda^N \left[\hat{H}_{imp} + \sqrt{\frac{\eta_0}{\pi}} \frac{\hat{\sigma}_z}{2} (\hat{b}_0 + \hat{b}_0^\dagger) + \sum_{k=0}^N \epsilon_k \hat{b}_k^\dagger \hat{b}_k + \sum_{k=0}^{N-1} t_k (\hat{b}_k^\dagger \hat{b}_{k+1} + \hat{b}_{k+1}^\dagger \hat{b}_k) \right], \quad (2.32)$$

we can deduce the relation between two successive Hamiltonians

$$\hat{H}_{N+1} = \Lambda \hat{H}_N + \Lambda^{N+1} \left[\epsilon_{N+1} \hat{b}_{N+1}^\dagger \hat{b}_{N+1} + t_N (\hat{b}_N^\dagger \hat{b}_{N+1} + \hat{b}_{N+1}^\dagger \hat{b}_N) \right]. \quad (2.33)$$

The NRG iteration starts with the Hamiltonian \hat{H}_0 describing the impurity and the first bosonic site

$$\hat{H}_0 = \hat{H}_{imp} + \sqrt{\frac{\eta_0}{\pi}} \frac{\hat{\sigma}_z}{2} (\hat{b}_0 + \hat{b}_0^\dagger) + \epsilon_0 \hat{b}_0^\dagger \hat{b}_0. \quad (2.34)$$

\hat{H}_0 is diagonalized and a set of eigenstates and eigenenergies is obtained. Next, we use Eq. (2.33) to obtain a rescaled new Hamiltonian in terms of the eigenstates $|s_0\rangle$ of the previous Hamiltonian and $|n_1\rangle$ of the new bosonic site and diagonalize it. The eigenstates obtained in each iteration are connected with the states of the previous iteration via a unitary transformation, described by the A -tensor $A^{[n_{N+1}]}$

$$|s_{N+1}\rangle = \sum_{n_{N+1}, s_N} A_{s_N, s_{N+1}}^{[n_{N+1}]} |s_N\rangle |n_{N+1}\rangle. \quad (2.35)$$

Because this connection shows the same structure as an MPS in the local picture Eq. (2.2), NRG can be formulated in matrix product states giving rise to many advantages [31, 18].

In each iteration step, we create a new product space $|s_N\rangle \otimes |n_{N+1}\rangle$, whose dimension grows exponentially with each added site. Without a truncation procedure, this leads to a numerically not feasible size of Hamiltonians to diagonalize. Because of the logarithmic discretization, the energy scales of the eigenstates of different Hamiltonians are separated sufficiently to have no influence on later iterations. That allows us to discard the high-energy eigenstates in each iteration and therefore keep the Hilbert space small enough, while describing the physics correctly. This truncation can either be accomplished with respect to a fixed number D of lowest-lying states or a rescaled energy E_{keep} up to which one wants to keep eigenstates. Which truncation criterion is best depends on the investigated model and has to be evaluated for each model with respect to the convergence of the NRG results, e.g. in terms of the discarded weight [32].

2.2.5 Energy-level flow diagrams

Typically, one focuses in a renormalization group procedure on transformations $R[H(\mathbf{r})] = H(\mathbf{r}')$ which leave the Hamiltonian invariant but rescale parameters or coordinates, leaving the physical features of the system invariant. Eventually, the sequence of transformations converges to one or more fixed points which are invariant in the sense that the parameters do not change under the transformation $R[H(\mathbf{r}^*)] = H(\mathbf{r}^*)$ anymore. These fixed points give information over possible macroscopic states and the physics driving the model.

In the case of NRG, the Hamiltonian changes after each iteration according to Eq. (2.33). Nevertheless, we can adapt the idea of the renormalization group and study the behavior of the rescaled eigenenergies E_N along the Wilson chain. The resulting diagram depicting the energy-level flow in the model allows us to distinguish different fixed points indicating different physical behavior of the model. Fig. 4 shows two examples of energy-level flow diagrams of the spin-boson model. In both cases, the spectrum does not change anymore after the first 20 iterations. In contrast to the case of a fermionic model, we do not have to distinguish between even and odd iterations.

2.2.6 The limitation of bosonic NRG

When dealing with bosonic systems, we encounter some systematic problems which impose a serious challenge to the NRG procedure.

First of all, the local bosonic basis $|n_k\rangle$ on each site of the Wilson chain is in principle infinitely large. Since local state spaces are no longer restricted by Pauli's principle, we have to truncate each local basis set to a finite number d_k of states, typically around 25. This can lead to a non-trivial truncation error in the NRG scheme.

The d_k states of each local Hilbert space have to be chosen a priori in a way that the lowest-lying eigenstates of the Hamiltonian \hat{H}_{N+1} in each iteration are approximated best. That is problematic especially in different fixed points regimes. To illustrate this, we consider a mean-field approach to the spin-boson Hamiltonian in Eq. (2.15) which

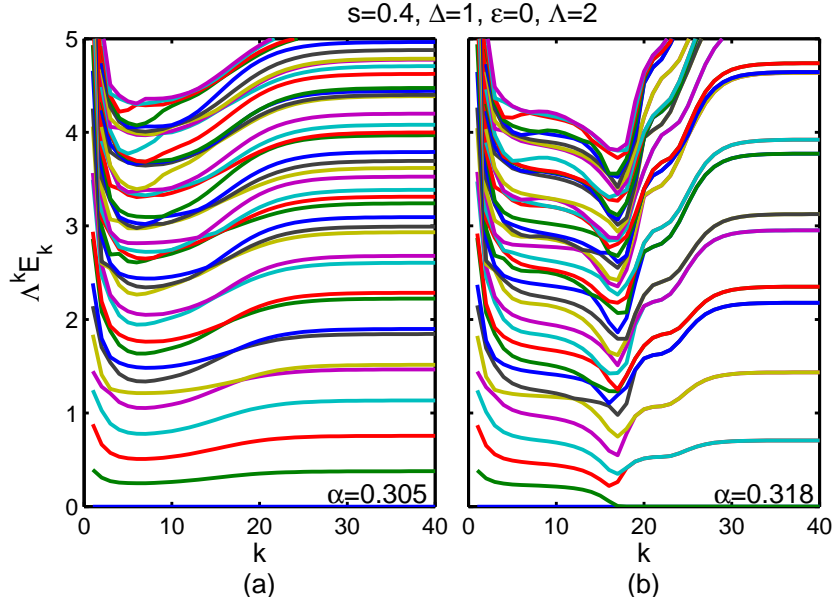


Figure 4: Energy-flow diagram of the spin-boson model calculated with NRG showing two different fixed points. In the left panel, after the first 20 iterations, the system converges in the fixed point corresponding to the delocalized regime, while in the right panel the dissipation is strong enough to localize the spin in one direction, resulting in a degenerate ground state. Not only the ground state but the whole spectrum of energy levels looks characteristic in different fixed point regimes.

lead to

$$\hat{H}_{MF} = \underbrace{\frac{\epsilon}{2}\hat{\sigma}_x - \frac{\Delta}{2}\hat{\sigma}_z + \frac{\hat{\sigma}_z}{2} \sum_i \lambda_i (\hat{a}_i + \hat{a}_i^\dagger)}_{\hat{H}_{imp}} + \underbrace{\frac{\langle \hat{\sigma}_z \rangle}{2} \sum_i \lambda_i (\hat{a}_i + \hat{a}_i^\dagger) + \sum_i \omega_i \hat{a}_i^\dagger \hat{a}_i}_{\hat{H}_{bath}}. \quad (2.36)$$

We concentrate on the two cases of a delocalized fixed point $\langle \hat{\sigma}_z \rangle = 0$ and a localized fixed point $\langle \hat{\sigma}_z \rangle \neq 0$. In the first case, the coupling term in \hat{H}_{bath} vanishes and thus the optimal basis to describe \hat{H}_{N+1} are the d_k lowest eigenstates $|n_i\rangle$ of every site. In the case of a localized fixed point, the coupling does not disappear and each mode is displaced by $\delta_i \propto \lambda_i \langle \hat{\sigma}_z \rangle / (2\omega_i)$. Therefore, the optimal basis choice to describe the system would be a set of displaced oscillators, but in general the displacements are not known a priori and grow exponentially along the chain. If not dealt with correctly, this leads to serious systematic errors, e.g. when calculating critical properties of the investigated models [30, 33]. Even though there were attempts within NRG [20], until now there exists no complete algorithm to form an optimal bosonic basis in the complete parameter spectrum of the spin-boson model. A way to deal with these problems is to use variational matrix product states, where the displacement is determined variationally and used to create the optimal bosonic basis in a controlled way. The next section gives an introduction to this method based on Guo et al. [14], who developed this approach in 2012.

2.3 Variational Matrix Product State

Even though NRG has been used successfully in the non-perturbative calculation of various static and dynamic properties on numerous quantum impurity models, it is limited in the sense that hopping amplitudes have to decrease exponentially. This led to the development of the Density Matrix Renormalization Group (DMRG) by Steven White [7, 34]. In contrast to NRG and despite of its name, DMRG does not contain the essential features of a renormalization group and is therefore able to solve one-dimensional lattice models which feature constant hopping amplitudes such as the Hubbard model.

DMRG allows not only the calculation of ground state properties of one-dimensional real-space interacting lattice models in a very efficient and accurate way, but was developed further to calculate dynamical [35, 36] and thermodynamical properties [37, 38] in one- as well as in higher-dimensional systems [39, 40, 41, 42]. Furthermore, DMRG can also be formulated in terms of matrix product states [43, 44, 17] where it works as a variational optimization scheme for the ground-state in the space of all matrix product states. Often the acronym DMRG is replaced in this context by the term variational matrix product states (VMPS).

Not only NRG but the VMPS procedure as well can be understood in terms of MPS, as Weichselbaum et al. [31] showed in 2005. Applied to a Wilson chain, both methods produce a similar MPS representation of the ground state of the model. Because VMPS and NRG use two different truncation criteria to keep the size of the bosonic Hilbert space feasible, the results are not fully equivalent. While VMPS truncates according to the singular-value decomposition of the matrices building up the MPS, NRG discards the highest-energy eigenstates of an effective Hamiltonian in each iteration step. That means, the energy-scale separation imbedded in NRG is in general not present in VMPS.

Depending essentially on the quantum impurity model of interest, the application of VMPS or NRG can have advantages with respect to numerical efficiency and accuracy. For systems with fermionic baths a comparison between the two methods is given in [45]. For bosonic systems, VMPS should be the method of first choice, since the corrections of open Wilson chains introduced in chapter 3 can so far only be incorporated correctly with the sweeping character of VMPS (see chapter 4). Additionally, VMPS allows the implementation of an optimal displace oscillator basis which gives access to parameter regimes not so easily available in NRG.

2.3.1 Variational optimization scheme

Again, we introduce the idea of VMPS in the context of an one-dimensional Hamiltonian \hat{H} , i.e. the chain-Hamiltonian Eq. (2.30) of the spin-boson model with a fixed length N . The VMPS scheme determines the ground state variationally in terms of matrix product states by iteratively optimizing each site in the local picture and thus sweeping several times back and forth the chain. We start at an arbitrary site of the chain with a random initialized state. To find the ground state of the system, we have to find the state fulfilling the minimization equation

$$E_0 := \min[E] = \min_{|\psi\rangle} (\langle\psi|\hat{H}|\psi\rangle - \lambda(\langle\psi|\psi\rangle - 1)) , \quad (2.37)$$

where λ is a Lagrange multiplier for the constraint of a proper normalization of the ground state. Switching into the local picture of site k , the non-linear minimization problem Eq. (2.37) reduces to a linear one

$$E_0 = \min_{A^{[n_k]}} \left(\sum_{lrn_k l' r' n'_k} A_{l' r'}^{[n'_k]*} \hat{H}_{l' r' n'_k l r n_k} A_{l r}^{[n_k]} - \lambda \left[\sum_{lrn_k} A_{l r}^{[n_k]*} A_{l' r'}^{[n'_k]} - 1 \right] \right), \quad (2.38)$$

where we have to optimize only one A -tensor, while all others are kept constant. Differentiating Eq. (2.38) with respect to $A_{l' r'}^{[n'_k]*}$, we obtain

$$\hat{H}_k \sum_{lrn_k} A_{l r}^{[n_k]} |l\rangle |n_k\rangle |r\rangle = \lambda \sum_{lrn_k} A_{l r}^{[n_k]} |l\rangle |n_k\rangle |r\rangle. \quad (2.39)$$

This local eigenvalue problem can be solved by standard techniques. Since we are only interested in the ground state of the system, we do not need to diagonalize the whole Hamiltonian but calculate $\hat{H}_k A_{l r}^{[n_k]}$ and determine the optimal A -tensor employing e.g. the Lanczos algorithm implemented in a normal sparse eigensolver. Thus, the eigenvalue λ takes the role of E_0 in Eq. (2.38), whereas the eigenvector gives the desired optimized version of the A -tensor. The last thing to do is to calculate the sparse Hamiltonian in the local picture, which can be written as

$$\begin{aligned} \hat{H}_k &= \hat{H}^l \otimes \mathbb{1}^k \otimes \mathbb{1}^r + \sum_{\alpha} \hat{O}_{\alpha}^l \otimes \hat{O}_{\alpha}^k \otimes \mathbb{1}^r \\ &+ \mathbb{1}^l \otimes \hat{H}^k \otimes \mathbb{1}^r + \sum_{\alpha} \mathbb{1}^l \otimes \hat{O}_{\alpha}^k \otimes \hat{O}_{\alpha}^r + \mathbb{1}^l \otimes \mathbb{1}^k \otimes \hat{H}^r, \end{aligned} \quad (2.40)$$

where the superscript indicates the space on which the operators act and $\mathbb{1}^l, \mathbb{1}^k, \mathbb{1}^r$ represent the identity matrices in the effective left, local and right basis, respectively. While the Hamiltonian \hat{H}^k and the operators \hat{O}_{α}^k are naturally given in the local space of site k , the other terms have to be calculated iteratively.

\hat{O}_{α}^l and \hat{O}_{α}^r can be constructed by an iterative transformation of their local basis sets to the effective basis sets $|l_k\rangle$ and $|r_k\rangle$ of site k . The most efficient way is therefore to calculate \hat{O}_{α}^l and \hat{O}_{α}^r in every iteration step out of \hat{O}_{α}^{k-1} and \hat{O}_{α}^{k+1} , which then can be combined with \hat{O}_{α}^k to construct the coupling Hamiltonian $\hat{H}^{l,k} = \sum_{\alpha} \hat{O}_{\alpha}^l \otimes \hat{O}_{\alpha}^k \otimes \mathbb{1}^r$ written in components

$$\begin{aligned} \hat{H}_{l_k, l'_k, n_k, n'_k}^{l,k} &= \sum_{\alpha} \sum_{n_{k-1}, n'_{k-1}, l_{k-1}} \left(A_{l_{k-1}, l'_k}^{[n_{k-1}]*} \hat{O}_{n_{k-1}, n'_{k-1}}^{k-1, \alpha} A_{l_{k-1}, l_k}^{[n_{k-1}]} \right) \hat{O}_{n_k, n'_k}^{k, \alpha} \\ &= \sum_{\alpha} \hat{O}_{l_k, l'_k}^{l, \alpha} \hat{O}_{n_k, n'_k}^{k, \alpha} \end{aligned} \quad (2.41)$$

and $\hat{H}^{k,r} = \sum_{\alpha} \mathbb{1}^l \otimes \hat{O}_{\alpha}^k \otimes \hat{O}_{\alpha}^r$

$$\begin{aligned} \hat{H}_{n_k, n'_k, r_k, r'_k}^{r,k} &= \sum_{\alpha} \hat{O}_{n_k, n'_k}^{k, \alpha} \sum_{n_{k+1}, n'_{k+1}, r_{k+1}} \left(A_{r_{k-1}, r'_k}^{[n_{k+1}]*} \hat{O}_{n_{k+1}, n'_{k+1}}^{k+1, \alpha} A_{r_{k+1}, r_k}^{[n_{k+1}]} \right) \\ &= \sum_{\alpha} \hat{O}_{n_k, n'_k}^{k, \alpha} \hat{O}_{r_k, r'_k}^{r, \alpha}. \end{aligned} \quad (2.42)$$

The parts of the Hamiltonian acting on the left and right part of the chain can then be constructed iteratively from the coupling Hamiltonians. For more details see the Appendix of [19].

We work in this thesis with NRG and VMPS on the same bosonic Wilson-chain Hamiltonians for which by construction the energy scales decay exponentially along the chain with Λ^{-k} . Because of the limited accuracy of computers (double precision), we apply the rescaling procedure presented in the context of NRG 2.2.4 also in the VMPS scheme, ensuring that the optimization always take place on the same energy scale. This can be done by multiplying \hat{H}_k by Λ^k before running the sparse eigensolver to determine the optimized version of $A^{[n_k]}$.

2.3.2 Truncation and convergence

Dealing with large many-body systems, VMPS also encounters the problem of an exponentially growing Hilbert space. However, the systematic truncation relies not on energy, as employed in NRG. We already mentioned in Section 2.1.2 that VMPS usually uses a SVD of the A -tensor of site k when switching to site $k \pm 1$ for truncation. Instead of performing an exact SVD, only the singular values with the most relevance are kept which are the largest ones as discussed in section 2.1.3. Arriving at the new site $k + 1$, we can optimize $A^{[n_{k+1}]}$ and move in this way to the end of the chain. Carrying the process out in the other direction, one can sweep back and forth along the chain until the state $|\psi\rangle$ converges in the ground state.

As convergence criterion we used in this thesis the variance of the unscaled ground state energies E_k calculated at each site of the length- N chain

$$\text{var}(E_k) = \frac{\sqrt{\frac{1}{N-1} \sum_k (E_k - \bar{E})^2}}{|\bar{E}|}, \quad (2.43)$$

where we defined the average value of the energy as \bar{E} . If after a sweep $\text{var}(E_k)$ drops below a lower bound $\epsilon \approx 10^{-13} - 10^{-15}$, we consider the calculated state $|\psi\rangle$ as a reliable approximation of the real ground state.

2.3.3 Optimal bosonic basis and variational shift

We introduced VMPS in this thesis because of the limitations of bosonic NRG regarding the choice of the optimal bosonic basis that can lead to severe errors for example in the localized regime of the spin-boson model. We now elaborate on how to solve this problem in the context of VMPS following Guo et al. [14]. The presented modification allows the study of bosonic quantum impurity models across the entire phase diagram. Since the originally introduced variational determination of the displacements of the bosonic basis is time-consuming, we also introduce another method developed by Güttinge [46], where all the local displacements are calculated simultaneously after one sweep, reducing the time of the VMPS calculation enormously.

In NRG the local basis of site k is immutable after the Hamiltonian is diagonalized and the next site is added. One of the main advantages of VMPS is the adaptability of the local basis on each site during the whole calculation.

This can be utilized in two steps. First of all, an optimal bosonic basis (OBB) $|\tilde{n}_k\rangle$ can be obtained from the original local harmonic oscillator basis $|n_k\rangle$ by a unitary transformation V first introduced by [47]

$$|\tilde{n}_k\rangle = \sum_{n_k=0}^{d_k-1} V_{\tilde{n}_k, n_k} |n_k\rangle, \quad (2.44)$$

where $\tilde{n}_k \in 0, \dots, d_{opt} - 1$ with d_k and d_{opt} giving the size of the original and optimal basis. The transformation matrix can be included in the structure of the A-tensors, preserving the MPS description of VMPS, as illustrated in Fig. 5(a),

$$A_{l_k, r_k}^{[n_k]} = \sum_{\tilde{n}_k=0}^{d_{opt}-1} \tilde{A}_{l_k, r_k}^{[\tilde{n}_k]} V_{\tilde{n}_k, n_k} \quad (2.45)$$

and allowing us to increase the size of the local bosonic basis drastically up to $d_k \leq 10^4$, while keeping the OBB small and thus the numeric in the optimization procedure feasible. The update procedure of site k has to be adapted in such a way that it consists of two steps, first optimizing the transformation matrix V and then the matrix $\tilde{A}_{l_k, r_k}^{[\tilde{n}_k]}$, again switching between the two local pictures by a SVD (see Fig. 5(b)).

To incorporate the natural shift of the bosonic basis in the set up of the basis itself, we follow [13] and introduce the unitary transformation

$$\hat{U}(\delta_k) = e^{\frac{\delta_k}{\sqrt{2}}(\hat{b}_k^\dagger - \hat{b}_k)}, \quad (2.46)$$

acting on the local bosonic operators \hat{b}_k^\dagger and \hat{b}_k as

$$\hat{b}'_k = \hat{U}^\dagger(\delta_k) \hat{b}_k \hat{U}(\delta_k) = \hat{b}_k + \frac{\delta_k}{\sqrt{2}}, \quad (2.47)$$

$$\hat{b}_k^{\dagger'} = \hat{U}^\dagger(\delta_k) \hat{b}_k^\dagger \hat{U}(\delta_k) = \hat{b}_k^\dagger + \frac{\delta_k}{\sqrt{2}}. \quad (2.48)$$

Since the oscillator coordinates can be written in terms of bosonic operators $\hat{x}_k = \frac{1}{\sqrt{2}}(\hat{b}_k + \hat{b}_k^\dagger)$, \hat{U} shifts the coordinate such that

$$\hat{x}'_k = \frac{1}{\sqrt{2}}(\hat{b}'_k + \hat{b}_k^{\dagger'}) = \hat{x}_k + \delta_k. \quad (2.49)$$

Therefore, Guo et al. proposed to calculate the equilibrium expectation value $\langle \hat{x}_k \rangle$ after the optimization procedure for site k described above and then apply the unitary transformation U on the chain-Hamiltonian $\hat{U}^\dagger \hat{H}(\hat{b}_k, \hat{b}_k^\dagger) \hat{U} = \hat{H}(\hat{b}'_k, \hat{b}_k^{\dagger'})$, resulting in a shift of the bosonic operators only. By choosing $\delta_k = -\langle \hat{x}_k \rangle$, the oscillator coordinates get shifted such that the OBB describes the quantum fluctuations near $\langle \hat{x}_k \rangle$, allowing us to simulate an effective local basis that would require a local dimension of $d_k^{eff} = 10^{10}$ with only $d_k = 10^2$ local basis states. After the shift, the optimization of the actual site k is repeated with the shifted basis until $\langle \hat{x}_k \rangle$ converges.

This is done for each site of the Wilson chain separately, thus additionally eliminating the problem of the exponentially growing shift to the end of the chain. In this thesis, $d_{opt} = 12$ and $D = 40$ are both chosen such that all singular values larger than 10^{-5} are kept.

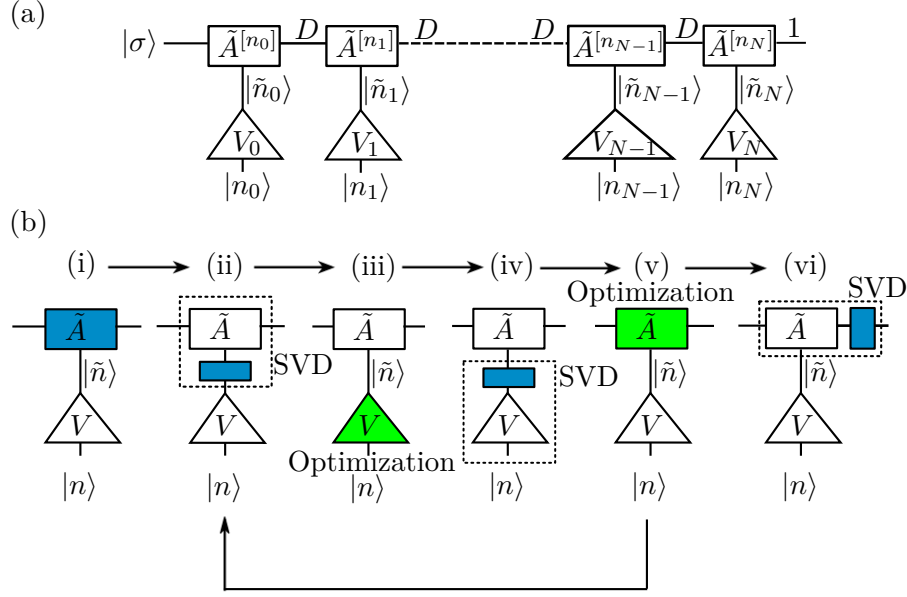


Figure 5: Diagram of a MPS with an optimal bosonic basis (a). The A -tensors of each site links the large local bases $|n_k\rangle$ to all other sites but only with a finite number of states D . The V_k matrices transform the local bases to smaller effective basis sets $|\tilde{n}_k\rangle$ used to optimize the \tilde{A} -matrices. This optimization procedure must be adapted slightly (b). We start at site k (i) and use a SVD (ii) to move the physical information to the corresponding V -matrix. After optimizing this matrix with respect to the ground state energy (iii), we use again a SVD (iv) to move back to the A -tensor and optimize it (v). We iterate the steps (ii)-(v) until convergence of local displacements is reached and then move to the next site using a SVD (vi), thus sweeping along the chain and optimizing the whole MPS.

2.3.4 Analytic shift

Instead of determining the displacement of the oscillators on each site variationally, Güttinge [46] showed that on the level of the Hamiltonian Eq. (2.30), the general idea to find a unitary transformation to a basis which minimizes the expectation value $|\langle \hat{b}_0^\dagger + \hat{b}_0 \rangle|$ yield the same displacements of the local bosonic bases as the variational approach.

We start with the chain Hamiltonian of the spin-boson model of length N and use the unitary transformation Eq. (2.46) to replace $\tilde{b}_k^\dagger = \hat{b}_k^\dagger + \delta'_k/\sqrt{2}$ and $\tilde{b}_k = \hat{b}_k + \delta'_k/\sqrt{2}$ such that the Hamiltonian takes the form

$$\tilde{H} = \hat{H}_{imp} + \sqrt{\frac{\eta_0}{\pi}} \frac{\hat{\sigma}_z}{2} (\tilde{b}_0 + \tilde{b}_0^\dagger) - 2 \frac{\delta'_0}{\sqrt{2}} \sqrt{\frac{\eta_0}{\pi}} \frac{\hat{\sigma}_z}{2} + E_0(\{\delta'_k\}) \quad (2.50)$$

$$+ \sum_{k=0}^{N-1} \epsilon_n \left(\tilde{b}_k^\dagger \tilde{b}_k - \frac{\delta'_k}{\sqrt{2}} (\tilde{b}_k + \tilde{b}_k^\dagger) + \frac{\delta'^2_k}{2} \right) \quad (2.51)$$

$$+ \sum_{k=0}^{N-2} t_k \left(\tilde{b}_k^\dagger \hat{b}_{k+1}^\dagger + \tilde{b}_{k+1}^\dagger \hat{b}_k^\dagger - \frac{\delta'_{k+1}}{\sqrt{2}} (\tilde{b}_k^\dagger + \tilde{b}_k) - \frac{\delta'_k}{\sqrt{2}} (\tilde{b}_{k+1}^\dagger + \tilde{b}_{k+1}) + 2 \frac{\delta'_k \delta'_{k+1}}{2} \right). \quad (2.52)$$

Note that we neglect $E_0(\delta'_k)$ because we are not interested in the shift of the ground state

energy. The resulting Hamiltonian can be divided into two parts $\tilde{H} = \tilde{H}_d + \tilde{H}_{no-d}$, where \tilde{H}_d contains all terms including the displacement operator $\tilde{b}_k^\dagger + \tilde{b}_k$ and \tilde{H}_{no-d} all others. Since the OBB is supposed to minimize $|\langle \hat{b}_0^\dagger + \hat{b}_0 \rangle|$, the displacement Hamiltonian must vanish

$$\tilde{H}_d \equiv 0 = \left(\sqrt{\frac{\eta_0}{\pi}} \frac{\hat{\sigma}_z}{2} - \frac{\delta'_0}{\sqrt{2}} \epsilon_0 - t_0 \frac{\delta'_1}{\sqrt{2}} \right) (\tilde{b}_0^\dagger + \tilde{b}_0) \quad (2.53)$$

$$- \sum_{k=1}^{N-1} \left(\epsilon_k \frac{\delta'_k}{\sqrt{2}} + t_k \frac{\delta'_{k+1}}{\sqrt{2}} (1 - \delta_{k,N-1}) + t_{k-1} \frac{\delta'_{k-1}}{\sqrt{2}} \right) (\tilde{b}_k^\dagger + \tilde{b}_k) . \quad (2.54)$$

These $N + 1$ coupled linear equations can be written as matrix equation where we replaced the operator $\hat{\sigma}_z$ by its expectation value

$$\begin{pmatrix} \epsilon_0 & t_0 & 0 & 0 & \dots \\ t_0 & \epsilon_1 & t_1 & 0 & \dots \\ 0 & t_1 & \epsilon_2 & t_2 & \dots \\ \vdots & \vdots & \ddots & \ddots & \ddots \end{pmatrix} \begin{pmatrix} \delta'_0 \\ \delta'_1 \\ \delta'_2 \\ \vdots \end{pmatrix} = \begin{pmatrix} \sqrt{\frac{\eta_0}{4\pi}} \langle \hat{\sigma}_z \rangle \\ 0 \\ 0 \\ \vdots \end{pmatrix} . \quad (2.55)$$

Inverting the matrix on the left hand side of the equation gives us the desired displacements

$$\delta'_k = -\delta'_{k-1} \frac{t_{i-1}^2}{\epsilon_i - \frac{t_i^2}{\epsilon_{i+1} - \frac{t_{i+1}^2}{\ddots}}} , \quad (2.56)$$

for $0 \leq i \leq N$ with $t_{-1}^2 = \sqrt{\frac{\eta_0}{4\pi}}$ and $\delta'_{-1} = \langle \hat{\sigma}_z \rangle$.

Because we replace $\hat{\sigma}_z$ by its expectation value, these equations have to be solved self consistently. Therefore, the expectation value $\langle \hat{\sigma}_z \rangle$ is determined after each VMPS sweep and the new displacements are calculated, which are used to perform the next DMRG run. This is done until convergence is reached, i.e. the ground state as well as $\langle \hat{\sigma}_z \rangle$ do not change anymore. Usually convergence of the magnetization is reached much faster than convergence of the ground state and occurs already after a few iterations. This can be seen in Fig. 6(a), where we pictured the magnetization for different values of s . In Fig. 6(b), we show the difference between the variational determined and the analytic shift which confirms that both methods yield the same shift.

2.3.5 Energy-level flow diagrams

We can also generate an energy-level flow diagram employing VMPS to a Wilson chain Hamiltonian. When sweeping from the left to the right end of the chain, we calculate in each iteration step the eigenvalues of the left block Hamiltonian \hat{H}_l , shift them such that the lowest eigenvalue $E_0 = 0$ and multiply them with the correct rescaling factor Λ^{k-1} . The resulting spectrum corresponds to the energy-level flow generated in NRG and contains the same information about the fixed points of the model. In Fig. 7, we show two energy-level flow diagrams calculated with VMPS using the same parameters as in

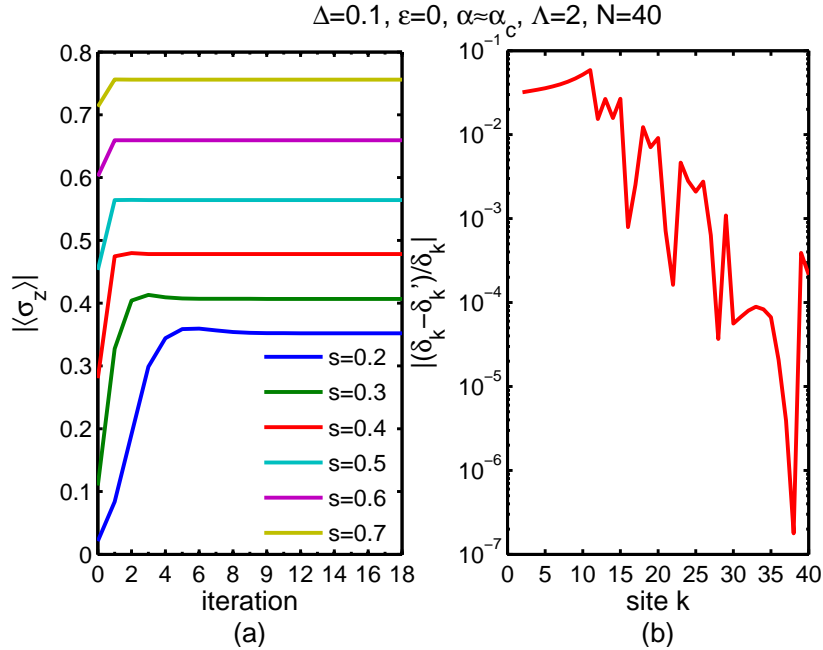


Figure 6: (a) Expectation value of the spin component $\hat{\sigma}_z$ for different values of s against the number of VMPS sweeps (iterations). After the first few iterations the expectation value converges to a constant value and thus also the displacements following from Eq. (2.56). Plotting the same data without the absolute value would show the alternating sign of the displacements. (b) Relative difference between the variational δ_k and analytic δ'_k determined displacements for $s = 0.4$, showing that both methods yield essentially the same shift.

Fig. 4, where the energy-level flow is generated via NRG. Since VMPS is optimized with respect to the ground state, the high-energy levels are not calculated exactly, resulting in discontinuities. This effect is even stronger in the localized regime since the problems concerning the local bosonic basis play a crucial role. It becomes even worse using a shifted bosonic basis, since the shift focuses only on the ground state, resulting in a basis not able to describe the high-energy levels correctly and breaking energy-scale separation. However, the qualitative cross-over of the fixed points behavior is nearly pictured correctly in both regimes.

2.3.6 Variational calculation of m lowest eigenstates

As discussed in the previous section, NRG is often not able to capture the physics of a bosonic system correctly. If we are only interested in ground state properties, VMPS is clearly the better choice. Going beyond ground state physics, it is possible to adapt the VMPS procedure to simultaneously describe the lowest m energy states exactly. We now present a simple modification of the procedure discussed in section 2.3.1, that allows us to calculate an arbitrary number of energy states. In our approach, we have neither used an optimal bases for the various levels nor any shift of the local bosonic basis. This is motivated by the fact that we want to calculate in section 4.1.6 the energy-level flow diagram of the dissipative harmonic oscillator in a regime where

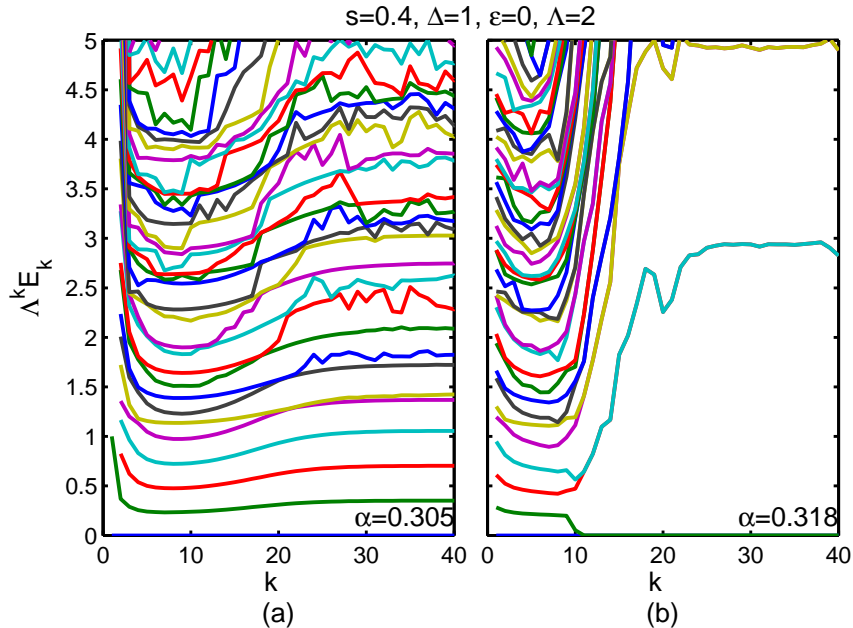


Figure 7: Energy-level flow diagram of the spin-boson model calculated with VMPS in delocalized (a) and localized (b) phase using the same parameters as in Fig. 4. Since the variational calculation focuses only on the ground state, the higher energy-levels are not determined correctly, resulting in non-smooth high-energy levels. The discrepancies to the NRG energy-level flow diagram are worse in the localized regime, because of the problems concerning the local bosonic bases.

neither a OBB nor a shift is necessary.

Our strategy will be as follows: we start again with a Wilson chain constituting of N sites and stay in the formulation of matrix product states. We describe all m states simultaneously in the local picture by defining on the local site k an array \mathbb{A}^k of m A -tensors (Fig. 8) where each tensor describes one state. We build up the Krylov subspace generated by the array \mathbb{A}^k and the Hamiltonian \hat{H}_k in the local picture of site k . We diagonalize the Hamiltonian in this subspace and construct from its eigenvectors an improved version of the array \mathbb{A}^k , whose components therefore are orthonormal by construction. To then move to site $k + 1$, we use a generalized version of a singular-value decomposition by contracting the A -tensors of \mathbb{A}^k with the A -tensor of site $k + 1$, tracing out the rest of the chain to obtain a reduced density matrix ρ , diagonalizing it with the transformation matrix U , retaining only the largest eigenvalues of the density matrix and using the truncated transformation matrix \tilde{U} to define the final version of the the A -tensor of site k and the array \mathbb{A}^{k+1} .

Let us now describe the procedure explicitly: To describe the m lowest states we define the array \mathbb{A}^k of site k as

$$\mathbb{A}^k = \{A_1^{[n_k]}, A_2^{[n_k]}, \dots, A_m^{[n_k]}\}. \quad (2.57)$$

Note that we use the same effective left $|l_k\rangle$ and right basis $|r_k\rangle$ for all A -tensors in the array to stay in formulation of matrix product states presented in section 2.1 for

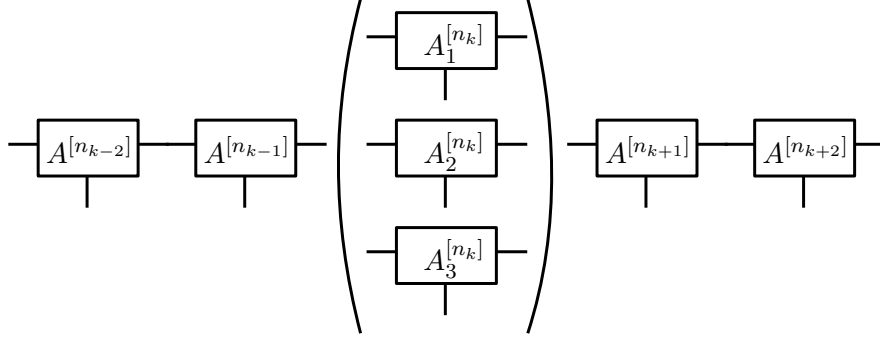


Figure 8: Illustration of the variation of a MPS to describe the m -lowest states. The A -tensor on site k is replaced by an array of m $A_i^{[n_k]}$ -tensors, each one describing one state. All other A -tensors remain unchanged. This makes an adaption of the optimization and update procedure necessary.

VMPS. This is equivalent to using an extra index with the local A^k , i.e. A^k becomes a four-dimensional tensor.

Similar to the procedure of optimizing one single A -tensor of site k described in section 2.3.1, in the next step we build up the Krylov subspace generated by the A -tensors of \mathbb{A}^k and the Hamiltonian \hat{H}_k in the local picture of site k . Note that the Hamiltonian is the same for all A -tensors, because we choose an effective common left basis for all states. We define the first m basis elements of the Krylov space as

$$|1\rangle = \mathbb{A}_1^k, \quad |2\rangle = \mathbb{A}_2^k, \quad \dots \quad |m\rangle = \mathbb{A}_m^k, \quad (2.58)$$

which are by construction orthonormal. The next m basis elements we obtain by application of \hat{H}_k and using the Gram-Schmidt process to form an orthonormal basis set

$$|\overline{m+j}\rangle = \hat{H}_k|j\rangle - \sum_{i=1}^{m+j-1} \langle i|\hat{H}_k|j\rangle|i\rangle, \quad j \in \{1, \dots, m\} \quad (2.59)$$

$$|m+j\rangle = \frac{|\overline{m+j}\rangle}{N_{m+j}}, \quad N_{m+j} = \sqrt{\langle \overline{m+j}|\overline{m+j}\rangle}. \quad (2.60)$$

Repeating the application of \hat{H}_k on the last m elements of the basis $n-1$ -times we can increase the Krylov space up to a chosen size nm . Since the Gram-Schmidt process is numerically unstable, we repeat the orthonormalization procedure a few times to ensure a orthonormal basis set. From Eq. (2.59) and Eq. (2.60) we can already deduce some information about the general structure of \hat{H}_k . Therefore, we assume $j \leq j'$ with $j, j' \in \{1, \dots, nm\}$ and obtain

$$\langle j|\hat{H}_k|j'\rangle = \left(\langle \overline{m+j}|\overline{m+j}\rangle + \sum_{i=1}^{j+m-1} \langle j|\hat{H}_k|i\rangle\langle i|\overline{m+j}\rangle \right) |j'\rangle \quad (2.61)$$

$$= \delta_{j+m,j'} N_{j'} + \sum_{i=1}^{j+m-1} \langle j|\hat{H}_k|i\rangle \delta_{i,j'}. \quad (2.62)$$

We conclude that the Hamiltonian is a sparse matrix with non-zero elements contained in form of block matrices of the size $m \times m$ located along the diagonal and first off-diagonal of \hat{H}_k which are calculated while building up the Krylov space basis. Eq. (2.63) shows \hat{H}_k in the Krylov space basis with $m = 3$ starting states and two iteration steps ($n = 3$).

$$\hat{H}_k = \left(\begin{array}{ccc|ccc|ccc} \langle 1|\hat{H}_k|1\rangle & \langle 1|\hat{H}_k|2\rangle & \langle 1|\hat{H}_k|3\rangle & N_4 & 0 & 0 & 0 & 0 & 0 \\ \langle 2|\hat{H}_k|1\rangle & \langle 2|\hat{H}_k|2\rangle & \langle 2|\hat{H}_k|3\rangle & \langle 2|\hat{H}_k|4\rangle & N_5 & 0 & 0 & 0 & 0 \\ \langle 3|\hat{H}_k|1\rangle & \langle 3|\hat{H}_k|2\rangle & \langle 3|\hat{H}_k|3\rangle & \langle 3|\hat{H}_k|4\rangle & \langle 3|\hat{H}_k|5\rangle & N_6 & 0 & 0 & 0 \\ \hline N_4 & \langle 4|\hat{H}_k|2\rangle & \langle 4|\hat{H}_k|3\rangle & \langle 4|\hat{H}_k|4\rangle & \langle 4|\hat{H}_k|5\rangle & \langle 4|\hat{H}_k|6\rangle & N_7 & 0 & 0 \\ 0 & N_5 & \langle 5|\hat{H}_k|3\rangle & \langle 5|\hat{H}_k|4\rangle & \langle 5|\hat{H}_k|5\rangle & \langle 5|\hat{H}_k|6\rangle & \langle 5|\hat{H}_k|7\rangle & N_8 & 0 \\ 0 & 0 & N_6 & \langle 6|\hat{H}_k|4\rangle & \langle 6|\hat{H}_k|5\rangle & \langle 6|\hat{H}_k|6\rangle & \langle 6|\hat{H}_k|7\rangle & \langle 6|\hat{H}_k|8\rangle & N_9 \\ \hline 0 & 0 & 0 & N_7 & \langle 7|\hat{H}_k|5\rangle & \langle 7|\hat{H}_k|6\rangle & \langle 7|\hat{H}_k|7\rangle & \langle 7|\hat{H}_k|8\rangle & \langle 7|\hat{H}_k|9\rangle \\ 0 & 0 & 0 & 0 & N_8 & \langle 8|\hat{H}_k|6\rangle & \langle 8|\hat{H}_k|7\rangle & \langle 8|\hat{H}_k|8\rangle & \langle 8|\hat{H}_k|9\rangle \\ 0 & 0 & 0 & 0 & 0 & N_9 & \langle 9|\hat{H}_k|7\rangle & \langle 9|\hat{H}_k|8\rangle & \langle 9|\hat{H}_k|9\rangle \end{array} \right). \quad (2.63)$$

Diagonalizing \hat{H}_k , we obtain the lowest m eigenvalues and the corresponding improved eigenvectors representing the new optimized A -tensors of site k . Together, they form the optimized array $\tilde{\mathbb{A}}^k$ whose components are orthonormal to each other by construction. Since H_k in general is small and all its matrix elements are calculated during the construction of the Krylov space basis, the calculation time is dominated either by the stabilized Gram-Schmidt process or by the construction of the basis set. While the stabilized Gram-Schmidt process scales with $\mathcal{O}((nm)^2 D^2 d_k / 2)$ where $(nm)^2 / 2$ describes the necessary number and $D^2 d_k$ the numerical costs of one operation, the construction itself is dominated by the application of \hat{H}_k on the A -tensors and scales with $\mathcal{O}(D^3 d_k nm)$. Thus, depending on the ratio $nm/2D$ the necessary time for the optimization procedure is dominated by the former or the latter process.

Because we want the effective right and left basis to be the same for all components of \mathbb{A} , we cannot switch to the next site by a simple SVD. Instead in the spirit of targeting multiple DMRG states, we form the reduced density matrix. For this, we contract each element of $\tilde{\mathbb{A}}^k$ (Fig. 9(i)) with the A -tensor of the next site

$$\left(\mathbb{B}_i^{k,k+1} \right)_{l_k, r_{k+1}} = \sum_j \left(\tilde{\mathbb{A}}_i^k \right)_{l_k, j} A_{j, r_{k+1}}^{[n_{k+1}]}, \quad (2.64)$$

where i indicates the elements of $\tilde{\mathbb{A}}^k$ and $\mathbb{B}^{k,k+1}$ (Fig. 9(ii)). Then, we determine the reduced density matrix of each component $\rho_{k,k+1}^{red,i}$ and sum them up (Fig. 9(iii))

$$\begin{aligned} \rho_{k,k+1} &= \sum_{i=1}^m \rho_{k,k+1}^{red,i} \\ &= \sum_{i=1}^m \sum_{n_1 \dots n_{k+1}} \sum_{n'_1 \dots n'_{k+1}} \left(A^{[n_1]} \dots A^{[n_{k-1}]} \mathbb{B}_i^{k,k+1} \right)^* \end{aligned} \quad (2.65)$$

$$\left(A^{[n_1]} \dots A^{[n_{k-1}]} \mathbb{B}_i^{k,k+1} \right) |n_1\rangle \langle n'_1| \dots |n_{k+1}\rangle \langle n'_{k+1}|. \quad (2.66)$$

As we already discussed in section 2.1.3, the spectrum of a density matrix and the singular values obtain by a SVD contain the same information about the entanglement of the system. Therefore, we diagonalize the resulting matrix $\rho_{k,k+1} = U^T D U$ and discard the eigenvectors in U corresponding to the smallest eigenvalues. Using the relation $\tilde{U}^T \tilde{U} = \mathbb{1}$, the tilde indicating the truncated spectrum, we insert the transformation matrices on the left site of $\mathbb{B}_i^{k,k+1}$ (Fig. 9(iv)). Then, we interpret \tilde{U}^T as the new A -tensor of site k , while

$$\mathbb{A}_i^{k+1} = \tilde{U} \mathbb{B}_i^{k,k+1}, \quad (2.67)$$

forms the new \mathbb{A} -array in the local picture of site $k+1$ (Fig. 9(v)). The switching from site $k+1$ to site k can be defined analogously, leading to the same sweeping scheme as before.

The convergence criterion can be adopted from the VMPS procedure presented in chapter 2, but we now demand that each energy E_i with $i \in \{1, \dots, m\}$ is converged within an upper bound ϵ

$$\text{var}(E_k^i) = \frac{\sqrt{\frac{1}{N-1} \sum_k (E_k^i - \bar{E}^i)^2}}{|\bar{E}^i|} \leq \epsilon \quad (2.68)$$

separately.

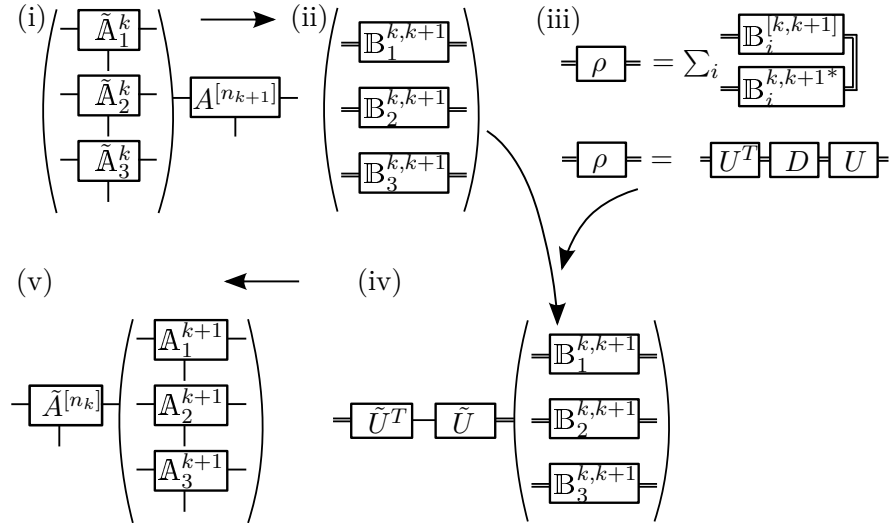


Figure 9: Update procedure to move from site k to site $k+1$ in the local picture of the modified MPS describing the lowest m levels. We start with an optimized site k (i) and contract each tensor of $\tilde{\mathbb{A}}^k$ with the A -tensor of the next site (ii), forming the array $\mathbb{B}^{k,k+1}$. Diagonalizing the reduced density matrix ρ_{red} , calculated by summing up the reduced density matrices of each element (iii), we obtain the transformation matrix U . Since we want to keep only states corresponding to eigenvalues values up to a fixed size, we truncate the transformation matrix (compare Sec. 2.1.3). In the next step, we insert the projection $\mathbb{1} = \tilde{U}^\dagger \tilde{U}$ (iv) on the left site of $\mathbb{B}^{k,k+1}$, where the tilde indicates the truncation of the smallest eigenvalues. The matrix \tilde{U}^T represents the new site $\tilde{A}^{[n_k]}$ whereas the rest forms the array in the local picture of site $k+1$ (v).

3 Open Wilson Chains

Quantum impurity models describe discrete quantum degrees of freedom coupled to a continuous bath of excitations. As we already elaborated on in chapter 2, it is necessary to discretize the continuous bath spectrum before mapping it onto a semi-infinite Wilson chain in order to make it numerically accessible for the application of NRG or VMPS. Furthermore, the chain is truncated to a finite length N , with N chosen such that all relevant energy-scales are sufficiently resolved. Then, this "length- N " chain is used to calculate both dynamic and thermodynamic quantities in the framework of NRG or VMPS.

Although the Wilson chain setup is highly successful for numerous applications, it contains some potentially problematic features especially in the context of NRG. Since the bath is discretized at the outset, a Wilson chain of any finite length actually constitutes of a closed quantum system with a discrete spectrum. These spectra must be broadened by hand after the NRG calculations to obtain smooth spectral functions. Another problem in NRG applications arises from the fact that the system at site k of a length- N chain has no information on "truncated" bath modes (TBMs), consisting of the high-energy modes neglected at previous sites and the low-energy modes associated with all later sites. While the latter information is available in the VMPS procedure with exception of the low-energy modes of sites $k > N$, the former is still missing. For models with asymmetric bath spectral functions, TBMs induce systematic energy shifts for the on-site energies that are missing in standard Wilson chain setups. This occurs for example in case of the spin-boson model [15] and leads to wrong predictions for the temperature dependence of the static spin susceptibility.

In this chapter, we introduce an iterative construction of an open Wilson chain (OWC) first presented by Frithjof Anders [48], in which each site is coupled to a separate bath of its own, thus keeping track of TBMs and avoiding discrete bath modes. This procedure allows to implement the effect of TBMs on the one hand and offers possible prescription for a naturally broadening of discrete spectral data on the other hand. In this thesis, we focus on the implementation of TBMs and its influence on numerical results. How to use OWC to obtain a natural description of broadening is topic of further research.

3.1 Iterative construction of an OWC

For our construction of an OWC, we only consider quantum impurity models of the form

$$\mathcal{H} = H^{imp} + H^S \quad (3.1)$$

where H^{imp} describes the impurity located at site $k = -1$ and its coupling via $t_{-1}^S b_{S,-1}^\dagger$ and its hermitian conjugate to a free bath H^S (Fig. 10(i)). t_{-1}^S denotes the coupling strength and $b_{S,-1}^\dagger$ a normalized linear combination of bath operators defined later. For such models, the retarded bath correlator plays a central role because it incorporates the complete physics of the system. Therefore, the key idea for constructing an OWC is to represent the bath correlator of the impurity on site $k = -1$ in terms of a site

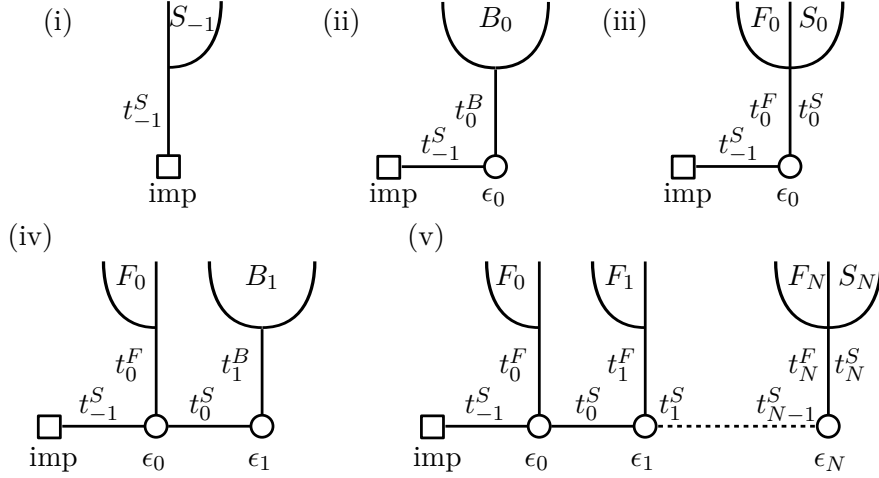


Figure 10: Iteration to construct an OWC. We start with the impurity coupled to a bath S_{-1} with coupling constant t_{-1}^S (i), which we replace by a new bath B_0 coupled to a single degree of freedom with energy ϵ_0 (ii) and coupling constant t_0^B . The impurity now couples only to the single site. In the next step, we split the bath into a part of fast (F_0) and a part of slow modes (S_0) (iii) and again replace the bath of slow modes by a single site and another bath B_1 (iv). Iterating this scheme N -times yields the OWC of length N , where each site is coupled to a bath of fast modes and the last site N additionally to a bath of slow modes (v). The parameters are determined such that the impurity correlator does not change, thus preserving the original physical behavior.

correlator associated with a specified site $k \neq -1$, coupled to a new bath. To simplify the notation we define the bath Hamiltonian \hat{H}_k^X and the normalized linear combination of bath operators \hat{b}_{Xk}^\dagger coupled to site k of an OWC

$$\hat{H}_k^X = \sum_q^X \omega_{qk} \hat{b}_{qk}^\dagger \hat{b}_{qk} \quad (3.2)$$

$$\hat{b}_{Xk}^\dagger = \sum_q^X \lambda_{qk}^X \hat{b}_{qk}^\dagger. \quad (3.3)$$

where X_k denotes the different baths occurring in the context of OWC, with X standing for B (bath), F (fast) and S (slow) and k denoting the site on which the bath couples. The sum indicates a summation over a specified energy range $\omega_{qk} \in I_k^X$ and the bath operators obey $[\hat{b}_{Xk}, \hat{b}_{Xk}^\dagger]_{\pm} = 1$ with a plus for the fermionic anticommutator and a minus for the bosonic commutator. Thus, we can write the retarded bath correlator $\mathcal{G}_k^X(\omega)$, describing the dynamics of the \hat{b}_{Xk} generated by H_k^X , as

$$\mathcal{G}_k^X(\omega) = \langle\langle \hat{b}_{Xk}; \hat{b}_{Xk}^\dagger \rangle\rangle_\omega = \sum_q^X \frac{|\lambda_{qk}^X|^2}{\omega - \omega_{qk} + i0^+} \quad (3.4)$$

which reduces for $k = -1$ and $X = S$ to the bath correlator of the impurity. Knowing the spectral function $\mathcal{A}_k^X(\omega) = -\frac{1}{\pi} \Im \mathcal{G}_k^X(\omega)$ which describes the coupling between site

k and the bath X_k , we know the correlator completely due to the Kramers-Kronig relation

$$\Re \mathcal{G}_k^X(\omega) = \int d\omega' \frac{\mathcal{A}_k^X}{\omega - \omega' + i0^+} . \quad (3.5)$$

We define the weight and the average energy ϵ_k^X of the spectral function by

$$1 = \int d\omega \mathcal{A}_k^X(\omega) \quad (3.6)$$

$$\epsilon_k^X = \int d\omega \omega \mathcal{A}_k^X(\omega) . \quad (3.7)$$

The central iteration for constructing an OWC of arbitrary length is to express the dynamics of site $k-1$ encoded in \mathcal{G}_{k-1}^S by the correlator of the next site. Starting with \mathcal{G}_{-1}^S ($k=0$), we replace $\hat{b}_{S,k-1}^\dagger$ by a new operator \hat{f}_k^\dagger with $[\hat{f}_k, \hat{f}_k^\dagger]_\pm = 1$ and \hat{H}_{k-1}^S by a new Hamiltonian \hat{H}_k

$$\hat{H}_k = \epsilon_k \hat{f}_k^\dagger \hat{f}_k + (t_k^B \hat{b}_{Bk}^\dagger \hat{f}_k + h.c.) + H_k^B , \quad (3.8)$$

describing a discrete degree of freedom *site* k linearly coupled to a new bath B_k (Fig. 10(ii)). This generates the site correlator for \hat{f}_k^\dagger

$$\mathcal{G}_k^B(\omega) = \langle\langle \hat{f}_k; \hat{f}_k^\dagger \rangle\rangle = \frac{1}{\omega - \epsilon_k - \Sigma_k^B(\omega)} , \quad (3.9)$$

where we define the self-energy $\Sigma_k^X(\omega) = |t_k^X|^2 \mathcal{G}_k^X(\omega)$. To ensure that the described dynamics does not change due to this transformation, we have to assure that $\mathcal{G}_k^B(\omega) = \mathcal{G}_{k-1}^S(\omega)$ which gives

$$|t_k^B|^2 \mathcal{G}_k^B(\omega) = \omega - \epsilon_k - \frac{|t_{k-1}^S|^2}{\Sigma_{k-1}^S(\omega)} , \quad (3.10)$$

with the on-site energy ϵ_k determined from the imaginary part of the general relation $\int d\omega \mathcal{G}_k^B(\omega) \mathcal{G}_{k-1}^S(\omega) = 0$

$$0 = \Im \left(\int d\omega \mathcal{G}_k^B(\omega) \mathcal{G}_{k-1}^S(\omega) \right) \quad (3.11)$$

$$= \Im \left(\int d\omega \left[\left(\omega - \epsilon_k - \frac{1}{\mathcal{G}_{k-1}^S(\omega)} \right) \mathcal{G}_{k-1}^S(\omega) \right] \right) \quad (3.12)$$

$$= \int d\omega \omega \mathcal{A}_{k-1}^S(\omega) - \epsilon_k \int d\omega \mathcal{A}_{k-1}^S(\omega) \quad (3.13)$$

$$= \epsilon_{k-1}^S - \epsilon_k . \quad (3.14)$$

Thus, Eq. (3.10) and the condition Eq. (3.6) on the imaginary part of the correlator determine both \mathcal{G}_k^B and $|t_k^B|$. Note that Eq. (3.10) implies that the spectral function \mathcal{A}_k^B has the same support as \mathcal{A}_{k-1}^S , i.e. $I_k^B = I_{k-1}^S$.

To ensure energy-scale separation at each iteration step, we have to split the bath into two subbaths, $B_k = F_k \cup S_k$ with $\hat{H}_k^B = \hat{H}_k^F + \hat{H}_k^S$ (Fig. 10(iii)). This is done by partitioning the energy range associated with bath B_k , i.e. $I_k^B = [\omega_{B_k}^-, \omega_{B_k}^+]$ into disjoint fast and slow subranges $I_k^F = [\omega_{F_k}^-, \omega_{F_k}^+]$ and $I_k^S = [\omega_{S_k}^-, \omega_{S_k}^+]$ with $I_k^B = I_k^F \cup I_k^S$ and $|\omega_{S_k}^\pm| \leq |\omega_{F_k}^\pm|$. The two subranges have to be chosen such that

$$\max(|\epsilon_k^S|, |t_k^S|) < \max(|\epsilon_{k-1}^S|, |t_{k-1}^S|) \quad (3.15)$$

holds. Depending on whether the initial coupling spectrum $\Gamma_{-1}(\omega)$ has a flat or power-law form or has a non-trivial structure, one would choose $\omega_{S_k}^\pm = \omega_{B_k}^\pm/\Lambda$ with $\Lambda > 1$ or would have to fine-tune the cutoff-frequencies ω_k^\pm in each step.

By defining the rescaled couplings $t_k^{F/S} = \alpha_k^{F/S} t_k^B$ with weights $|\alpha_k^{F/S}|^2 = \int_{I_k^{F/S}} d\omega \mathcal{A}_k^B(\omega)$, we can set $\lambda_{qk}^{F/S} = \lambda_{qk}^B/\alpha_k^{F/S}$ and decompose \hat{b}_{Bk}^\dagger into orthogonal fast and slow parts, and similarly for Σ_k^B

$$\hat{b}_{Bk}^\dagger = \alpha_k^F \hat{b}_{Fk}^\dagger + \alpha_k^S \hat{b}_{Sk}^\dagger \quad (3.16)$$

$$\Sigma_k^B(\omega) = \Sigma_k^F(\omega) + \Sigma_k^S(\omega) . \quad (3.17)$$

Now we are ready to perform the next iteration step. After every iteration, we obtain a bath of fast modes F_k and slow modes S_k and replace the slow mode bath by a new site $k+1$ coupled to a new bath B_{k+1} while ensuring $\mathcal{G}_{k+1} = \mathcal{G}_k^S$ (Fig. 10(iv)). Then, we split B_{k+1} again into a slow and fast part, etc.. After $N+1$ iteration steps, the initial \mathcal{H} has been replaced by $\hat{\mathcal{H}}_N^{OWC} = \hat{H}_N^{SWC} + \hat{H}_N^{TBM}$ where

$$\hat{H}_N^{SWC} = \hat{H}^{imp} + \sum_{k=0}^N \epsilon_k \hat{f}_k^\dagger \hat{f}_k + \sum_{k=0}^{N-1} t_k^S (\hat{f}_{k+1}^\dagger \hat{f}_k + \hat{f}_{k+1} \hat{f}_k^\dagger) \quad (3.18)$$

$$\hat{H}_N^{TBM} = \sum_{k=0}^N t_k^F (\hat{b}_{Fk}^\dagger \hat{f}_k + \hat{b}_{Fk} \hat{f}_k^\dagger) + \sum_{k=0}^N \hat{H}_k^F + t_N^S (\hat{b}_{SN}^\dagger \hat{f}_N + \hat{b}_{SN} \hat{f}_N^\dagger) + \hat{H}_N^S , \quad (3.19)$$

with \hat{H}^{imp} describing the impurity and the coupling to the fast bath F_{-1} (Fig. 10(v)). For any value of $N \geq 0$, $\hat{\mathcal{H}}_N^{OWC}$ and \mathcal{H} generate the same impurity dynamics by construction, since $\mathcal{G}_0 = \mathcal{G}_{-1}^S$. While \hat{H}_N^{SWC} has the structure of a length- N standard Wilson chain, \hat{H}_N^{TBM} describes the coupling to all fast fast mode baths $F_{k \leq N}$ and the coupling of the last site N to its bath of slow modes S_N . These truncated bath modes are normally neglected in a SWC, but can be kept track of in OWC.

3.2 General implementation

Iterating Eqs. (3.10) and (3.17) yields an exact continued fraction expansion (CFE) for \mathcal{G}_0 , e.g. for a length-2 OWC:

$$\mathcal{G}_{-1}(\omega) = \frac{1}{\omega - \epsilon_0 - \Sigma_0^F(\omega) - \frac{|t_0^S|^2}{\omega - \epsilon_1 - \Sigma_1^F(\omega) - \frac{|t_1^S|^2}{\omega - \epsilon_2(\omega) - \Sigma_2^F(\omega) - \Sigma_2^S(\omega)}}} . \quad (3.20)$$

The CFE can be used to numerically verify that the determined chain parameters indeed reproduce the initial bath correlator \mathcal{G}_{-1} . Furthermore, we can see the influence of the TBMs, namely that (i) the real part of the baths self energy shifts the energy of the corresponding local site and (ii) its imaginary part broadens the states of the corresponding Wilson shells.

For numerical calculations, we have to approximate the OWC to the structure of a reduced SWC (RWC), that can be treated with standard NRG or VMPS methods while incorporating the effects of the TBMs. The *static approximation* replaces the self-energies of the TBMs in the CFE Eq. (3.20) by their real part evaluated at $\omega = 0$

$$\tilde{\epsilon}_k = \epsilon_k + \delta\epsilon_k^F + \delta_{kN}\delta\epsilon_N^S, \quad \delta\epsilon_k^{F/S} = \Re\left(\Sigma_k^{F/S}(0)\right), \quad (3.21)$$

which lead simply to shifted on-site energies. Therefore, the real part of the zero-frequency correlator $\mathcal{G}_0(\omega = 0)$, is reproduced correctly for a RWC of arbitrary length, in contrast to a SWC, where the absence of the TBMs leads to the mass flow error for the sub-Ohmic spin-boson model [15]. If ones starts with a symmetric bath spectral function, $\Gamma_{bath}(\omega) = \Gamma_{bath}(-\omega)$, as it is the case for fermionic systems with particle-hole symmetry, the effect of the TBMs is negligible since contributions from positive and negative frequencies cancel, resulting in $\delta\epsilon_k^{F/S} = 0 \forall k$. The evaluation of the real part of the self-energies at $\omega = 0$ yield Wilson shell energies that become increasingly inaccurate for larger energies within the shell. However, it is a suitable approximation for the calculation of ground state properties.

In the following discussions we distinguish three different types of RWCs to compare our results and understand the influence of the TBMs. A C0 chain is a RWC without any energy correction due to the TBMs, whereas the baths of fast modes are incorporated via energy shifts of the on-site energies $\epsilon_k + \delta\epsilon_k^F$ and the bath of slow modes on the last site is neglected for a C1 chain. Finally, a C2 chain additionally contains the shift of the on-site energy on the last site N due to the influence of the bath of slow modes $\epsilon_k + \delta\epsilon_k^F + \delta_{kN}\epsilon_N^S$.

The implementation of higher order perturbation theory to capture the effects of the TBMs more correctly, is still topic of further research. Since we neglect the imaginary parts of all self-energies, dissipative effects are not captured, but they are a perfect starting ground for a natural broadening of the spectra obtained with NRG.

4 Applications

In this chapter, we use the concept of OWC introduced in chapter 3 to investigate two models, the dissipative harmonic oscillator (DHO) and the spin-boson model (SBM). Both models show qualitative erroneous behavior [9, 15] when investigated in the standard Wilson chain setup with NRG and VMPS. The DHO provides the possibility to compare numerical result with analytic calculations via exact diagonalization of the quadratic Hamiltonian, whereas the SBM is the first bosonic model which has been investigated and is analytically not solvable for the whole parameter regime. We show, that even the simple static approximation that leads us from open to reduced Wilson chains, solves the problems encountered so far with bosonic NRG and VMPS and reproduces the correct results confirmed by analytic calculations or other numerical methods like quantum Monte Carlo.

4.1 Dissipative harmonic oscillator

The dissipative harmonic oscillator describes a displaced, harmonic oscillator coupled to a bath of bosonic modes. In contrast to the SBM, it is exactly solvable since the Hamiltonian is bilinear. Thus, we are able to compare numerical with analytic results by exact diagonalization that do not suffer the errors due to the truncation of the local bosonic basis.

In this section, we first concentrate on the critical coupling of the DHO and then show some iteration details of the RWC, numerically confirming the ideas of the previous chapter and highlighting the effects of the TBMs on the CFE and Wilson chain parameters. Then, we present different methods to calculate the static susceptibility of the DHO and conclude that, so far, only VMPS is able to capture the effects of TBMs correctly. In the end of this section, we focus on the energy flow diagrams and compare the numerical results with the method of exact diagonalization.

4.1.1 Determination of critical coupling

The DHO is described by the Hamiltonian

$$\hat{H}_{\text{DHO}} = \Omega \hat{a}^\dagger \hat{a} + \frac{\epsilon}{2} (\hat{a} + \hat{a}^\dagger) + \frac{1}{2} \sum_q \lambda_q (\hat{a} + \hat{a}^\dagger) (\hat{b}_q + \hat{b}_q^\dagger) + \sum_q \omega_q \hat{b}_q^\dagger \hat{b}_q, \quad (4.1)$$

with $\Omega > 0$ denoting the impurity oscillator frequency, ϵ the field conjugate to the oscillator displacement and $\omega_q > 0$ the frequencies of the bath oscillators. The spectral density completely describes the interaction with the bosonic bath,

$$\Gamma(\omega) = \pi \sum_q \lambda_q^2 \delta(\omega - \omega_q), \quad (4.2)$$

since its fully determines the impurity correlator \mathcal{G}_{-1} . Similar to the SBM, we choose the typical parametrized power-law form

$$\Gamma(\omega) = 2\pi\alpha\omega_c^{1-s}\omega^s, \quad (4.3)$$

when focusing on the low-energy behavior, with the cutoff frequency $\omega_c = 1$ and α describing the dissipation strength. This model becomes unstable for $\alpha > \alpha_c$ [49] because the coupling to the bosonic bath renormalizes the oscillator frequency Ω which becomes zero at $\alpha = \alpha_c$. This characteristic behavior can also be observed by studying the susceptibility χ , associated with the displacement of the impurity oscillator

$$\chi = \frac{d\langle \hat{a} + \hat{a}^\dagger \rangle_T}{d\epsilon}, \quad (4.4)$$

where $\langle \rangle_T$ denotes a thermal average. Using the relation $\chi = \mathcal{G}_x(\omega = 0)/2$ with

$$\mathcal{G}_x(\omega) = \langle \langle \hat{a} + \hat{a}^\dagger; \hat{a} + \hat{a}^\dagger \rangle \rangle \quad (4.5)$$

$$= \frac{2\Omega}{\omega^2 + i0^+ - \Omega^2 - \Omega(\mathcal{G}_{-1}(\omega) + \mathcal{G}_{-1}(\omega))/2} \quad (4.6)$$

we obtain

$$\chi = \frac{1}{\Omega + \Re \mathcal{G}_{-1}(\omega = 0)}. \quad (4.7)$$

Note that the susceptibility is temperature independent and only determined by Ω and the real part of the bath correlator. The critical dissipation strength α_c is defined by $\Omega + \Re \mathcal{G}_{-1}(\omega = 0) = 0$ where the lowest eigenenergy turns negative and the susceptibility diverges. Knowing the spectral function, we can immediately determine the real part of the impurity correlator at $\omega = 0$

$$\Re \mathcal{G}_{-1}(\omega = 0) = \frac{2\alpha\omega_c}{s} \quad (4.8)$$

and thus have $\alpha_c = \frac{s\Omega}{2\omega_c}$. With the parameter choice $\alpha = 0.4$, $\epsilon = 0$ and $\Omega = 1$ the predicted critical coupling is $\alpha_c = 0.2$. Numerically, α_c can be found by determining the α -value for which the susceptibility Eq. (4.7) diverges or by studying the behavior of the energy-flow diagrams obtained with NRG or VMPS. The value of the impurity correlator at $\omega = 0$, by construction of the RWC, is independent of the chain length. It only depends on the tightness of the frequency grid ω representing the spectral function $\Gamma(\omega)$ via Kramers-Kronig. Therefore, the discrepancies between the numerical and the theoretical values of α_c can systematically be reduced, by improving the resolution of the frequency grid. Our best obtained value is $\alpha_c = 0.19997$ which can be improved straightforwardly. This is the first improvement to the DHO when investigated with SWC, where a different critical coupling of $\alpha_c \approx 0.228$ is obtained numerically [15]. In the following, we use a more coarser grid to reduce calculation times, which results in a critical coupling strength of $\alpha_c \approx 0.19986$. For VMPS calculation, we use $D = 40$ as upper dimension bond and $d_k = 12$ as dimension for the optimal bosonic basis.

4.1.2 Iteration details

We have explored two ways to construct a RWC, that differ only in the choice of the cutoff frequencies $\omega_{S_k}^+$. In the first version, we tuned the cutoff frequencies such that the resulting hopping elements t_k^S of the OWC agree with those obtained with the scheme

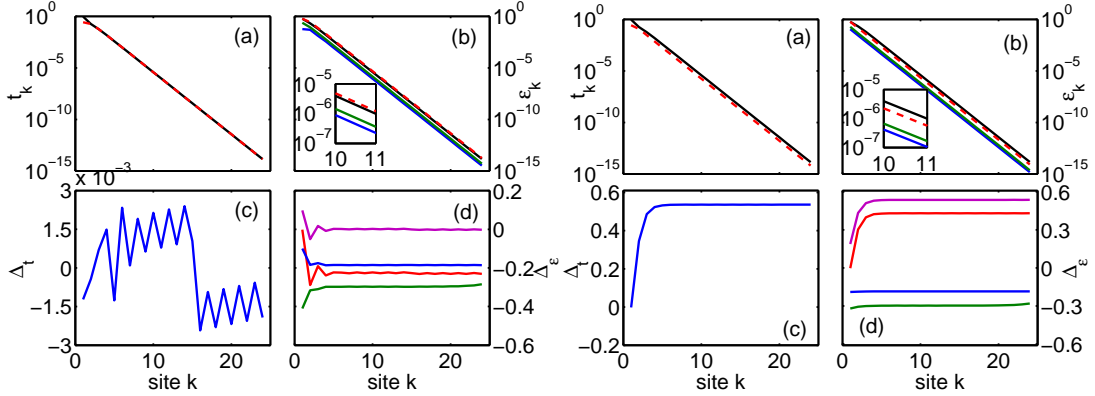


Figure 11: (a-d) Comparison of the Wilson chain parameters t_k and ε_k for $\alpha = 0.199$, obtained using the standard discretization scheme of BTV [9] for $\Lambda = 4$, or using two versions of the RWC-approach described above: for version 1 (left two columns), $\omega_{S,k}$ was fine-tuned to ensure that $t_k = t_k^{BTV}$; for version 2 (right two columns), we simply chose $\omega_{S,k+1} = \omega_{S,k+1}/\Lambda$. (a) t_k^{BTV} used by BTV (black) and our t_k (red dashed). (b) The on-site energies ε_k^{BTV} (black), our C0 on-site energies ε_k (red dashed), and the shifts $-\tilde{\varepsilon}_k^F$ (blue) and $-\tilde{\varepsilon}_k^S$ (green). Evidently, they all scale the same way with k . (c) Relative difference $\Delta_t = (t_k^{BTV} - t_k)/t_k^{BTV}$ in hopping elements. The noisy structure seen for version 1 (left) reflects the ω -discretization grid used to represent the bath correlators $\mathcal{G}_k^X(\omega)$ during the OWC construction. (d) Relative differences Δ_ε of various on-site energies: $\Delta_\varepsilon^{C0} = (\varepsilon_k^{BTV} - \varepsilon_k)/\varepsilon_k^{BTV}$ (red); $\Delta_\varepsilon^{C1} = (\varepsilon_k^{BTV} - \varepsilon_k - \delta\varepsilon_k^F)/\varepsilon_k^{BTV}$ (purple); $\Delta_\varepsilon^F = \delta\varepsilon_k^F/\varepsilon_k$ (blue); and $\Delta_\varepsilon^S = \delta\varepsilon_k^S/\varepsilon_k$ (green). For version 1 (left), the relative difference between BTV and C0 energies (no shifts) is quite significant throughout ($\Delta_\varepsilon^{C0} \simeq 0.2$). The relative difference between BTV and C1 energies (only fast shifts) is significant for early iterations, but becomes small ($\Delta_\varepsilon^{C1} \lesssim 10^{-3}$) once the iteration scheme reaches self-similarity. For version 2 (right), both Δ_ε^{C0} and Δ_ε^{C1} differ significantly from 0. Both the fast and last slow mode shifts are comparable in magnitude to the bare OWC energies, $\mathcal{O}(\Delta_\varepsilon^{F/S}) = 1$.

by Bulla, Tong, and Vojta t_k^{BTV} [15] with an relative error below 10^{-3} . With a finer ω grid in the calculation of the spectral functions $\Gamma_k(\omega)$ and more evolved integration methods, the agreement could be further improved. In the second version, we used the already suggested relation $\omega_{S,k}^\dagger = \omega_{Bk}^\dagger/\Lambda$. In panel (a)-(d) of Fig. 11, we show a comparison of the two different versions and note the following.

(i) All quantities decrease with the same exponential decay along the Wilson chain. Note that even the fast and slow shifts $\delta\varepsilon_k^{F/S}$ have the same order of magnitude as the bare OWC energies ε_n and are comparable in magnitude.

(ii) The on-site energies of a RWC without any correction on the last site $\tilde{\varepsilon}_k = \varepsilon_k + \delta\varepsilon_k^F$, (C1-chain), and with correction $\tilde{\varepsilon}_k = \varepsilon_k + \delta\varepsilon_k^F + \delta_{k,N}\varepsilon_k^S$ (C2-chain), are in general different from the SWC energies ε_k^{BTV} Fig. 11(d). Note that the relative difference becomes negligible after the first iterations. Nevertheless, the scheme developed by BTV does not incorporate the effects of the TBMs of the first sites and of the slow bath of the last site, which leads to wrong predictions.

(iii) The power-law coupling spectrum Γ takes on a self-similar structure after the first few iterations, i.e. $\Re(\Sigma_k^B(\omega)) / \max(\Re(\Sigma_k^B(\omega)))$ and $\Im(\Sigma_k^B(\omega)) / \max(\Im(\Sigma_k^B(\omega)))$, plotted against ω/ω_{Bk} , do not change with k (Fig. 12(a)-(b)). This can be used to ex-

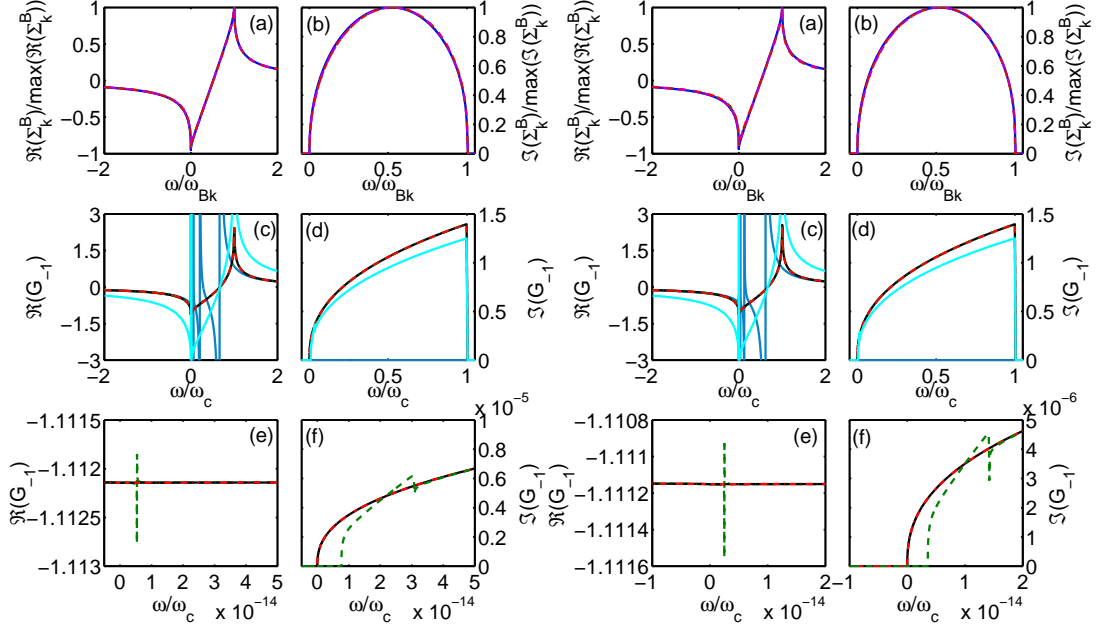


Figure 12: Similar to Fig. 11 the left columns depict the results for version 1, whereas the right columns illustrate the results for version 2. Both version yield qualitatively similar results: (a) $\mathfrak{R}[\Sigma_k^B(\omega)]/\max(\mathfrak{R}[\Sigma_k^B(\omega)])$ and (b) $\mathfrak{I}[\Sigma_k^B(\omega)]/\max(\mathfrak{I}[\Sigma_k^B(\omega)])$, plotted vs. $\omega/\omega_{B,k}^+$ for $k = 1, 2, 5, 10$ (different colors), showing that the spectral functions and self-energies have a self-similar structure. (c) $\mathfrak{R}[\mathcal{G}_{-1}(\omega)]$ and (d) $\mathfrak{I}[\mathcal{G}_{-1}(\omega)]$ vs. ω/ω_c , calculated directly from $\Gamma_{-1}(\omega)$ (solid black), or from the CFE (Eq. 3.20) with $N = 25$, while including both $\Sigma_k^F(\omega)$ and $\Sigma_N^S(\omega)$ (dashed red), only $\Sigma_k^F(\omega)$ with $N = 5$ (cyan) and $N = 25$ (green), or neither of the two (blue). In the latter case, the absence of any imaginary parts in the CFE causes $\mathfrak{I}[\mathcal{G}_{-1}(\omega)]$ to vanish and $\mathfrak{R}[\mathcal{G}_{-1}(\omega)]$ to have divergences. Behavior of (e) $\mathfrak{R}[\mathcal{G}_{-1}(\omega)]$ and (f) $\mathfrak{I}[\mathcal{G}_{-1}(\omega)]$ for $\omega \rightarrow 0$ with coloring as in (g). The missing slow-mode term in the CFE using only $\Sigma_k^F(\omega)$ (green) causes discrepancies only at the vicinity of $\omega = 0$ for both the imaginary and the real part.

trapolate the hopping elements t_n and bare on-site energies ϵ_k of an OWC, reducing the numerical costs to determine the chain parameters drastically. To avoid numerical calculations of the chain parameters $< 10^{-16}$ with quadruple precision, such extrapolation schemes are necessary.

(iv) The CFE with a chain length of $N = 25$ (Fig. 12(c)-(f)) reproduces $\mathcal{G}_{-1}(\omega)$ (solid black) exactly if $\Sigma_k^F(\omega)$ and $\Sigma_N^S(\omega)$ are included (dashed red). If the slow mode contribution on the last site is neglected, we observe in the reconstruction of the impurity correlator a dependence on the chain length. For $N = 25$ (dashed green), only in the vicinity of $\omega = 0$ we see discrepancies between the real and imaginary part of \mathcal{G}_{-1} (Fig. 12(e)-(f)) and the reconstruction. Reducing the chain length to $N = 5$ (cyan) increases the differences significantly to the whole frequency interval. If we do not consider the TBMs (blue), $\mathfrak{I}[\mathcal{G}_{-1}]$ vanishes because of the absence of imaginary contributions in the CFE, and $\mathfrak{R}[\mathcal{G}_{-1}]$ diverges. We see, that the TBMs are necessary to reconstruct the correct impurity dynamics in form of the impurity correlator \mathcal{G}_{-1} . The longer the chain, the less important is the influence of the slow bath on the last site of

the chain. However, in this case the fast baths contain already most of the information of the system dynamics and are thus crucial for NRG and VMPS calculations.

4.1.3 Susceptibility calculation

We now investigate, whether a RWC chain is able to determine the correct behavior of the susceptibility for the DHO, which poses an impossible task for a SWC [15].

To understand the influence of the TBMs, we used the three different types of RWCs and several different ways to calculate the susceptibility Eq. (4.4). On the one hand, we calculated the static susceptibility via the dynamical correlation function

$$C(\omega) = \frac{1}{2\pi} \int_{-\infty}^{\infty} e^{i\omega t} C(t) dt , \quad (4.9)$$

where $C(t) = \frac{1}{2} \langle [\hat{a} + \hat{a}^\dagger, \hat{a} + \hat{a}^\dagger] \rangle_T$ is the displacement correlation function. The dynamical susceptibility is then given by

$$\chi_{dyn}(T) = 4 \int_0^\infty \frac{C(\omega)}{\omega} d\omega , \quad (4.10)$$

which can be shown to be equal to the static susceptibility $\chi(T) = \chi_{dyn}(T)$. This can be used as an important consistency check for the numerical NRG calculations. For all three types of chains (C0,C1,C2), calculating $\chi(T)$ by evaluating the thermal average in a Wilson shell and using fdm-NRG to determine the dynamical susceptibility χ_{dyn} yield the same results. However, none of these approaches reproduce the exact result (Eq. 4.7).

On the other hand, we approximated the thermal expectation value by an expectation value with respect to one single state: the ground state $|G\rangle_{N_T}^W$ of a Wilson shell N_T , or the variational obtained ground state $|G\rangle_{N_T}^V$ of a length- N_T chain. N_T is the length of a RWC whose smallest excitation energies are comparable to the temperature

$$\max\{|\epsilon_{N_T}|, |t_{N_T}|\} \approx T . \quad (4.11)$$

In contrast to all other methods and types of RWC, using VMPS on a C2 chain reproduces the correct susceptibility χ , as we now will discuss in detail. Fig. 13 shows the calculated susceptibility for the three types of RWCs, C0 (blue), C1 (green), C2 (red), calculated in four different ways: Using the CFE (solid lines), a thermal average (TW, triangles), the expectation value with respect to the ground state of a Wilson shell (GW, squares) or with respect to the ground state obtained with VMPS (GV, circles). Additionally, we show the susceptibility calculated with the hopping elements and energies obtained with the scheme of BTV (dashed purple) and the exact results χ_{exact} (dashed black). All derivatives were evaluated numerically by using several ϵ values close enough around zero to fit the linear behavior of the expectation value. Note that for every epsilon value a separate calculation is necessary. To apply NRG on a C2 chain, the iteration presented in section 2.2 must be adapted slightly. For details see Appendix A.

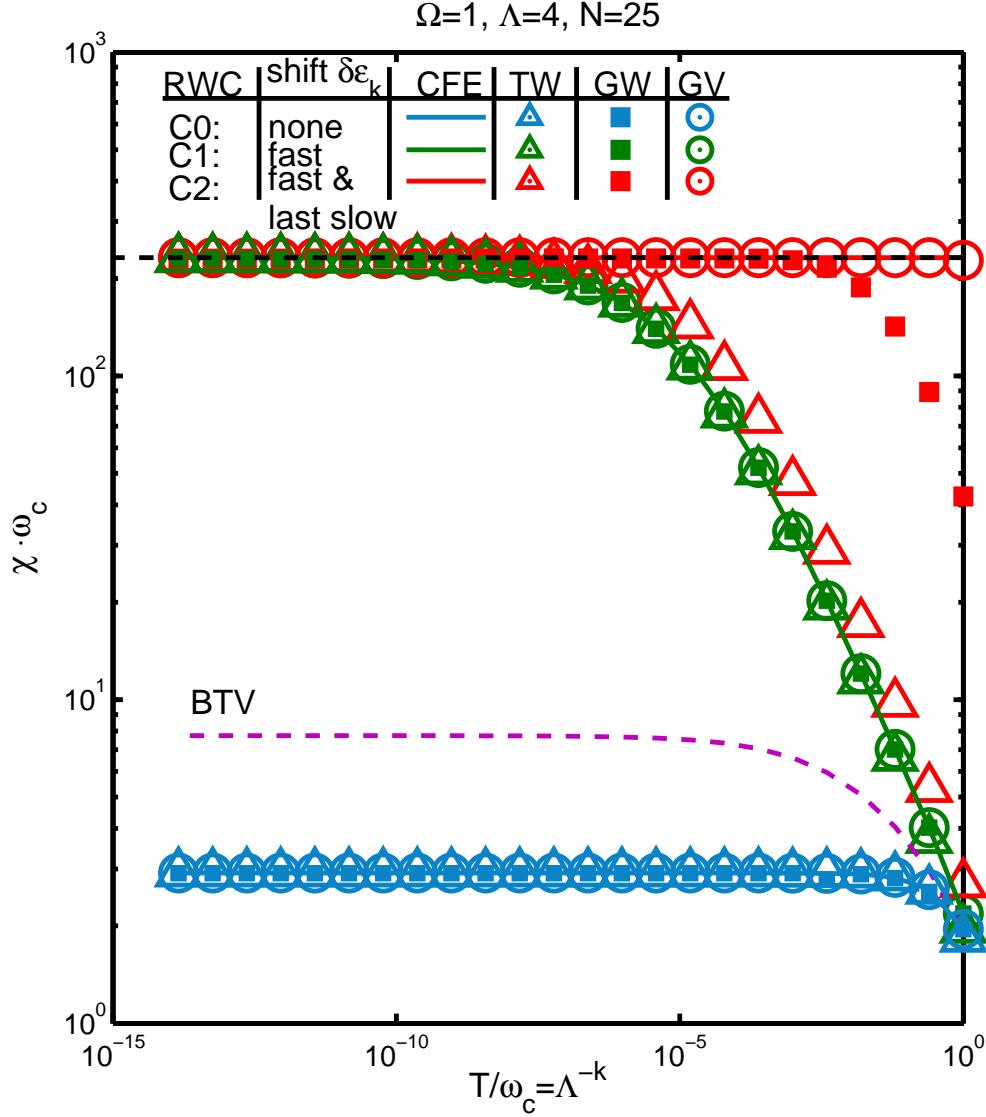


Figure 13: Static susceptibility $\chi(T)$ as function of temperature for $\alpha = 0.199$ and $s = 0.4$. The black dashed line indicates the exact result calculated from Eq. (4.7) while the dashed purple line is the solution obtained with the hopping amplitudes and on-site energies from the discretization scheme of BTV. The other data are numerical results for three types of RWC: C0 (blue), C1 (green) and C2 (red), calculated with 4 different methods. The solid lines are obtained with a CFE of length N_T to evaluate Eq. (3.20), the triangles by evaluating $\langle \rangle_T$ in Eq. (4.4) as thermal average over a Wilson shell (N_T), the circles by an approximation of $\langle \rangle_T$ by an expectation value with respect to the ground state $|G\rangle_{N_T}^W$ of a Wilson shell N_T and the squares by using the variational ground state $|G\rangle_{N_T}^V$ as approximation. In all cases, the derivative $d/d\epsilon$ was evaluated numerically using several ϵ -values close enough to zero. TW-, GW- and GV-averages require separate runs for each combination of T and ϵ .

First of all, all four methods consistently yield the same results for both C0 (blue) and C1 (green) but not for C2 (red) chains. Consequently, the only difference between the methods is their treatment of the slow modes on the last site, which are only present for C2 chains. Since the correction to the on-site energies due to the slow modes on the last site has the same order of magnitude as the bare on-site energy ϵ_N (see Fig. 11), this correction has influence on the previous sites. In contrast to NRG, where we diagonalize a sequence of Hamiltonians from the left end to the right end of the chain without any feedback of later to previous sites because of energy scale separation, VMPS sweeps several times along the chain. Thus, it carries the information of the slow modes on the last site to the previous sites, as needed to produce the correct temperature-independent behavior of χ .

Secondly, in the C0 case (red) where we have no information on any TBMs, we observe two important differences to the exact result: instead of being temperature independent, $\chi_{C0}(T)$ increases with decreasing T and saturates at a constant value orders of magnitude below the exact result χ_{exact} . The susceptibility calculated with the BTV energies and hopping elements shows the same behavior, but saturates at a higher value. Looking at Fig. 11(d), this makes sense since the on-site energies of a SWV obtained with BTV differ only on the first sites from those of a C1 chain. Therefore, BTV already incorporates some effects of the baths of fast modes on later sites. As we already investigated, the effect of the TBMs are important for the actual value of the critical coupling. Thus, because we used the same coupling strength $\alpha = 0.199$ for all types of RWCs, with a C0 chain we are farther away from the critical coupling strength than with a BTV chain, where we are the closest to α_c with a C1 chain. This results in lower saturation values of the susceptibility χ from C1 to BTV to C0 chains.

For a C1 chain, the temperature dependence of $\chi_{C1}(T)$ persist but the saturation value agrees with the exact value $\chi_{C1}(0) = \chi_{exact}$. Since the bath of slow modes on the last site of the chain has decreasingly influence with increasing chain length, as we can see in Fig. 12(c)-(f), in a C1 chain nearly the complete information of the TBMs is present for small temperatures. Thus, $\chi_{C1}(T)$ displays the correct behavior for small T .

In contrast, for the C2 chain two methods reproduce the full T -independent result $\chi_{C2}(T) = \chi_{exact}$, namely CFE and GV. Both methods incorporate the slow mode contributions completely, the one by construction (CFE) and the other because of the sweeping process and thus the ability to deal with the large energy shift on the last site of the RWC.

The other two methods, TW- and GW-averaging, fail to deal correctly with the large energy shift on the last site because no feedback to earlier sites is possible. We note that GW produces a better result than TW. Probably, the reason is that the static approximation leading from an OWC to a RWC focuses on $\omega = 0$, which seems to work less well when incorporating information from higher lying Wilson states, as done for a thermal average, than for the ground state $|G\rangle_{N_T}^W$.

Since the missing fast mode contribution in the BTV energies leads to a different critical coupling strength than for the C2 RWC, in Fig. 14 we show the susceptibility calculated with BTV and C2 GV for different α -values, chosen to yield comparable distances to the α_c -values of each method. One can easily see, that only the missing slow

mode correction and therefore the different amount of information on the environment for every chain length leads to the temperature dependent susceptibility. The slow mode correction becomes negligible for low temperatures such that the saturation value is approximately the same for both chains. Thus, the fast mode correction is necessary to predict the actual correct value of χ .

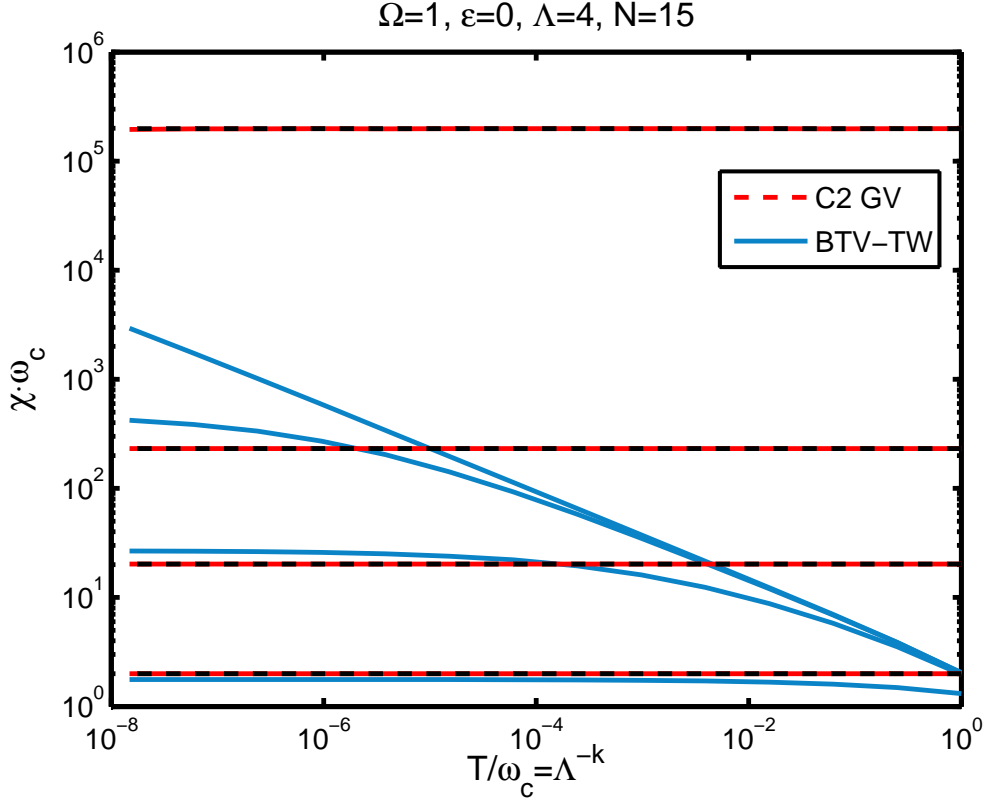


Figure 14: Susceptibility $\chi(T)$ as function of temperature, calculated using BTV couplings and on-site energies and standard NRG with TW expectation values (blue) for $\alpha = 0.1, 0.22, 0.228, 0.2284682$ (from bottom to top). The red lines show the results for C2 chains using GV expectation values for $\alpha = 0.1, 0.19, 0.199, 0.19986$ (from bottom to top) while the black dashed lines show exact results. The α -values are chosen such that the distance to the critical coupling strength is similar for both cases. BTV-TW incorrectly predicts a temperature dependent susceptibility, especially near α_c , but the same saturation value $\chi(T \rightarrow 0)$ as C2-GV. C2-GV correctly leads to a temperature independent susceptibility that agrees fully with the exact one.

4.1.4 Exact diagonalization

Before discussing energy-level flow diagrams, we will concentrate on the exact solution of the DHO. Since the Hamiltonian

$$\hat{H}_{\text{DHO}} = \Omega \hat{a}^\dagger \hat{a} + \sqrt{\frac{\eta_0}{4\pi}} (\hat{a} + \hat{a}^\dagger) (\hat{a}_0 + \hat{a}_0^\dagger) + \sum_{k=0}^{N-1} \epsilon_k \hat{a}_k^\dagger \hat{a}_k + \sum_{k=0}^{N-2} t_k (\hat{a}_k^\dagger \hat{a}_{k+1} + \hat{a}_{k+1}^\dagger \hat{a}_k), \quad (4.12)$$

is bilinear, we are able to transform it into diagonal form and incorporate the TBMs as energy shift on the on-site energies. The Hamiltonian has the general matrix representation

$$\hat{H}_{\text{DHO}} = \frac{1}{2} \vec{\alpha}^\dagger M \vec{\alpha} - \text{Tr}[A], \quad (4.13)$$

with the vector $\vec{\alpha}$ constituting of operators defined as

$$\vec{\alpha}^\dagger = \left(\hat{a}^\dagger \quad \hat{a}_0^\dagger \quad \hat{a}_1^\dagger \quad \dots \quad \hat{a} \quad \hat{a}_0 \quad \hat{a}_1 \quad \dots \right), \quad (4.14)$$

which obeys the bosonic commutation relation $[\vec{\alpha}_i, \vec{\alpha}_j^\dagger] = \mathbb{1}_-$ with

$$\mathbb{1}_- = \begin{pmatrix} \mathbb{1} & \\ & -\mathbb{1} \end{pmatrix}. \quad (4.15)$$

Because of the second term in Eq. (4.12), the matrix M is defined as

$$M = \begin{pmatrix} A & B \\ B^* & A^* \end{pmatrix}, \quad (4.16)$$

with the submatrices

$$A = \begin{pmatrix} \Omega & \sqrt{\frac{\eta_0}{4\pi}} & 0 & 0 & 0 \\ \sqrt{\frac{\eta_0}{4\pi}} & \epsilon_0 & t_0 & 0 & 0 \\ 0 & t_0 & \epsilon_1 & t_1 & 0 \\ 0 & 0 & t_1 & \epsilon_2 & t_2 \\ 0 & 0 & 0 & t_2 & \ddots \end{pmatrix}, \quad B = \begin{pmatrix} 0 & \sqrt{\frac{\eta_0}{4\pi}} & 0 & 0 & 0 \\ \sqrt{\frac{\eta_0}{4\pi}} & 0 & 0 & 0 & 0 \\ 0 & 0 & 0 & 0 & 0 \\ 0 & 0 & 0 & 0 & 0 \\ 0 & 0 & 0 & 0 & \ddots \end{pmatrix}, \quad (4.17)$$

obeying $A = A^\dagger$, $B = B^T$ and thus making M hermitian. We now employ a transformation that diagonalizes \hat{H}_{DHO} and preserve these commutation relation. This Bogoliubov transformation $\vec{\beta} = T \vec{\alpha}$ has the form

$$T = \begin{pmatrix} X & Y^* \\ Y & X^* \end{pmatrix} \quad (4.18)$$

and must obey

$$T \mathbb{1}_- T^\dagger = \mathbb{1}_- \quad (4.19)$$

to preserve the commutation relation. Since the matrix M is hermitian, there exists always a unitary transformation to diagonalize the Hamiltonian. In general, this transformation cannot fulfill Eq. (4.19) because the vector Eq. (4.14) now consist of operators and not complex numbers [50]. A possible solution is to diagonalize the dynamical matrix D instead (compare [50])

$$i \frac{d}{dt} \vec{\alpha} = D \vec{\alpha}, \quad (4.20)$$

with

$$D = \begin{pmatrix} A & B \\ -B^* & -A^* \end{pmatrix} = \mathbb{1}_- M \quad (4.21)$$

defined by the Heisenberg equation of motions

$$i \frac{d}{dt} \hat{a} = \Omega \hat{a} + \sqrt{\frac{\eta_0}{4\pi}} (\hat{a}_0 + \hat{a}_0^\dagger) \quad (4.22)$$

$$i \frac{d}{dt} \hat{a}_0 = \epsilon_0 \hat{a}_0 + \sqrt{\frac{\eta_0}{4\pi}} (\hat{a} + \hat{a}^\dagger) \quad (4.23)$$

$$i \frac{d}{dt} \hat{a}_n = \epsilon_n \hat{a}_n + t_n \hat{a}_{n+1}^\dagger + t_{n-1} \hat{a}_{n-1} \quad (4.24)$$

and $\frac{d}{dt} \hat{a}^\dagger = -\frac{d}{dt} \hat{a}$ because of the commutation relations. The dynamical matrix has a number of important properties [50]: (i) it is in general not hermitian, in contrast to the Hamiltonian H_{DHO} . (ii) D has $2N$ eigenvalues, of which only N are independent, with $\omega_n = -\omega_{k+N}^*$, $k \leq N$. (iii) If the matrix M has an eigenvalue equal or below zero, the transformation breaks down, in the sense that the eigenvalues of D become partly complex. We concentrate on the case where all eigenvalues of D are real and choose the first N eigenvalues to be positive. (iv) With this choice, the transformation matrix built up by the eigenvectors $T = [\vec{V}_1, \vec{V}_2, \dots]$ fulfills Eq. (4.19), yielding the transformation of the bosonic operators

$$\hat{b}_k^\dagger = \vec{\alpha}^\dagger \mathbb{1}_- \vec{V}_k \quad (4.25)$$

$$\hat{b}_k = \vec{V}_k^\dagger \mathbb{1}_- \vec{\alpha} . \quad (4.26)$$

(v) Additionally, T also diagonalizes M . The eigenvalues of the dynamical matrix $T^{-1}DT = \text{diag}(\omega_1, \dots, -\omega_1, \dots)$ and the ones of the original Hamiltonian $T^\dagger MT$ are related by

$$T^\dagger MT = T^\dagger \mathbb{1}_- DT = \mathbb{1}_- T^{-1}DT = \mathbb{1}_- \text{diag}(\omega_1, \dots, -\omega_1, \dots) , \quad (4.27)$$

where we used Eq. (4.19) in the second step.

Therefore, the diagonalization of the dynamical matrix D yields the eigenvalues ω_n of M as well as the Bogoliubov transformation of the bosonic annihilation and creation operators, such that Hamiltonian can be written in diagonal form

$$H = \sum_{k, \omega_k > 0} \omega_k \hat{b}_k^\dagger \hat{b}_k + E_0 \quad (4.28)$$

$$E_0 = \frac{1}{2} \sum_{k, \omega_k > 0} \omega_k - \frac{1}{2} \text{Tr}[A] . \quad (4.29)$$

Since α_c indicates the critical coupling strength for which the model becomes unstable, i.e. one mode becomes zeros, the transformation works for all $\alpha < \alpha_c$. In Fig. 15 the lowest eigenvalues of M are plotted against the length of the Wilson chain N for a C1 and a C2 chain and three different coupling strengths below α_c . For the C2 chain, we can see clearly that the lowest eigenvalue approaches zero for $\alpha \rightarrow \alpha_c$ while the higher eigenvalues do not change significantly. With increasing chain length, the lowest eigenvalue increases towards a saturation value slightly below that of the lowest eigenvalue of the C1 chain.

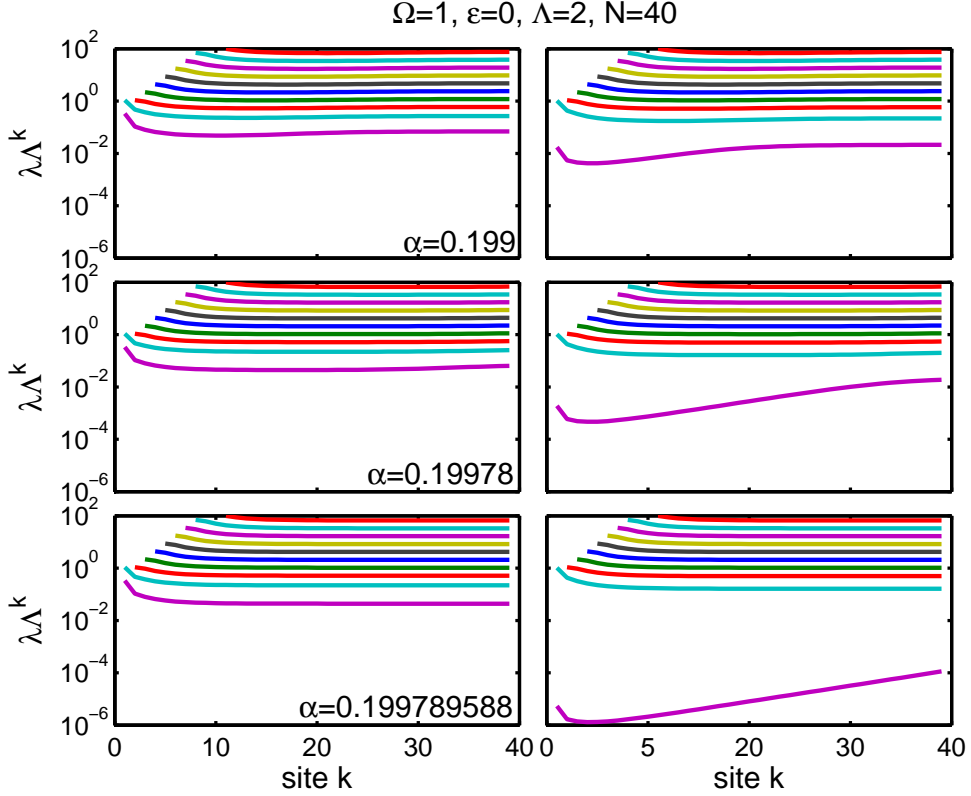


Figure 15: One-particle spectrum of the DHO obtained by diagonalizing H_{DHO} exactly for a C1 (left) and a C2 chain (right). If α approaches α_c (up to down), the lowest eigenvalue approaches zero for the C2 chain. With increasing chain length, the gap between the lowest two eigenvalues decreases. In the case of the C1 chain, the changes with increasing α value are small and not discernable in this figure.

4.1.5 Calculation of the occupation number

To see whether a variational calculation of the many-body spectrum is numerical feasible, we calculate the occupation number of the impurity and chain site for the DHO, following [46]. We start with occupation number given by the thermal expectation value

$$\langle \hat{n}_{imp} \rangle = \frac{\text{Tr}[e^{\beta \hat{H}} \hat{a}^\dagger \hat{a}]}{Z}. \quad (4.30)$$

To express the number operator $\hat{a}^\dagger \hat{a}$ through the new operators, we need to invert the transformation

$$\eta \vec{\beta} = V^\dagger \eta \vec{\alpha}, \quad (4.31)$$

with V having the form

$$V = \begin{pmatrix} X & Y^* \\ Y & X^* \end{pmatrix}. \quad (4.32)$$

This yields

$$a = \vec{X}_0 \vec{b} + \vec{Y}_0^* \vec{b}^\dagger \quad (4.33)$$

$$a^\dagger = \vec{Y}_0 \vec{b} + \vec{X}_0^* \vec{b}^\dagger, \quad (4.34)$$

where we defined \vec{X}_0 and \vec{Y}_0 to be the first column vector of X and Y respectively. Inserting this relations in the expression for the occupation number of the impurity Eq. (4.30), we obtain

$$\langle \hat{n}_{imp} \rangle = \sum_{k,k'} \underbrace{\frac{e^{-\beta \hat{H}} \hat{b}_k^\dagger \hat{b}_{k'}}{Z}}_{\delta_{k,k'} g(\omega_k)} X_{0k}^* X_{0k'} + \sum_{k,k'} \frac{e^{-\beta \hat{H}} \hat{b}_k \hat{b}_{k'}^\dagger}{Z} Y_{0k}^* Y_{0k'} \quad (4.35)$$

$$= \left(X \cdot \text{diag}(g(\omega_1), g(\omega_2), \dots) \cdot X^\dagger \right)_{00} + \sum_k \underbrace{\frac{\text{Tr} [e^{-\beta \hat{H}} \hat{b}_k^\dagger \hat{b}_k] + \text{Tr} [e^{-\beta \hat{H}}]}{Z}}_{g(\omega_k)+1=-g(-\omega_k)} Y_{0k}^* Y_{0k} \quad (4.36)$$

$$= \left(X \cdot \text{diag}(g(\omega_1), g(\omega_2), \dots) \cdot X^\dagger \right)_{00} - \left(Y \cdot \text{diag}(g(\omega_1), g(\omega_2), \dots) \cdot Y^\dagger \right)_{00}, \quad (4.37)$$

with $g(\omega)$ denoting the Bose function at temperature β . An analog calculation yields the occupation number of the different chain sites

$$\langle \hat{n}_k \rangle = \left(X \cdot \text{diag}(g(\omega_1), g(\omega_2), \dots) \cdot X^\dagger \right)_{k+1, k+1} - \left(Y \cdot \text{diag}(g(\omega_1), g(\omega_2), \dots) \cdot Y^\dagger \right)_{k+1, k+1}. \quad (4.38)$$

In Fig. 16, the calculated occupation number of the ground state of a C2 chain is plotted against the chain site for different chain lengths N and three coupling strengths. We observe an exponential increase of the occupation number towards the end of the chain. However, $\langle \hat{n}_k \rangle$ saturates on a moderate value at the critical chain length N^* , with N^* increasing when approaching the critical coupling strength α_c .

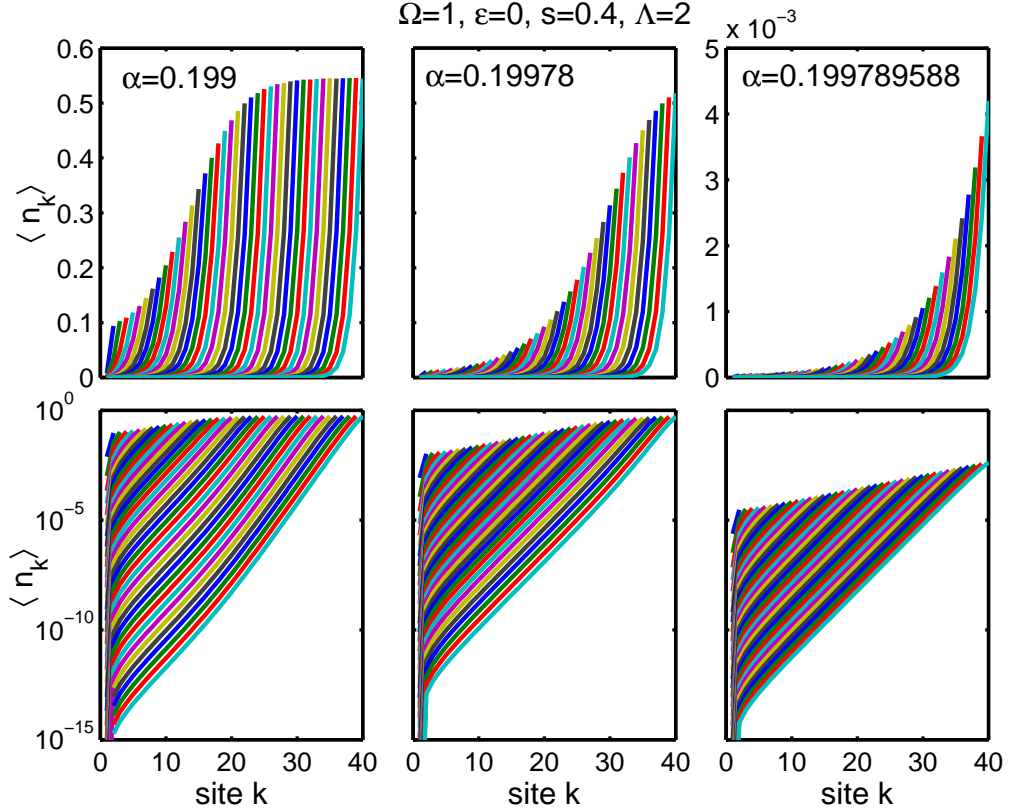


Figure 16: Calculated occupation number of the impurity and the chain sites plotted against the chain site n for different chain lengths N (colors) and three coupling strengths far from (left) and near (right) α_c in the upper row. In the lower row, semilogarithmic plot of the same data. While the occupation number of a special site decreases with increasing chain length, the occupation number of the last site grows exponentially with N , but saturates beyond a characteristic chain length N^* . This correspond to the one-particle spectrum of Fig. 15 where the lowest energy level saturates at the same chain length. N^* depends on the distance to α_c and increases when approaching the critical coupling strength.

4.1.6 Energy-level flow diagrams

After calculating the one-particle spectrum of the DHO via exact diagonalization and checking that the occupation number stays finite and thus a VMPS approach to the DHO is numerically promising, we apply the modified VMPS procedure presented in section 2.3.6 to calculate the energy-level flow diagrams of the DHO. Note that, because of the correction to the on-site energy on the last site of the C2 chain due to the TBMs, we have to run separate calculations for every chain length.

In Fig. 17 we show the energy-level flow diagram of the four lowest levels for three different values of α , both for a C1 and a C2 chain. Since a C1 chain is equivalent to a SWC with renormalized critical coupling strength α_c , we observe on the left side of Fig. 17 the typical behavior of an energy-level flow diagram of the DHO. In the critical regime the energy-levels are constant over a number of different chain lengths and equidistant, with an energy difference equivalent to the lowest energy-level of the

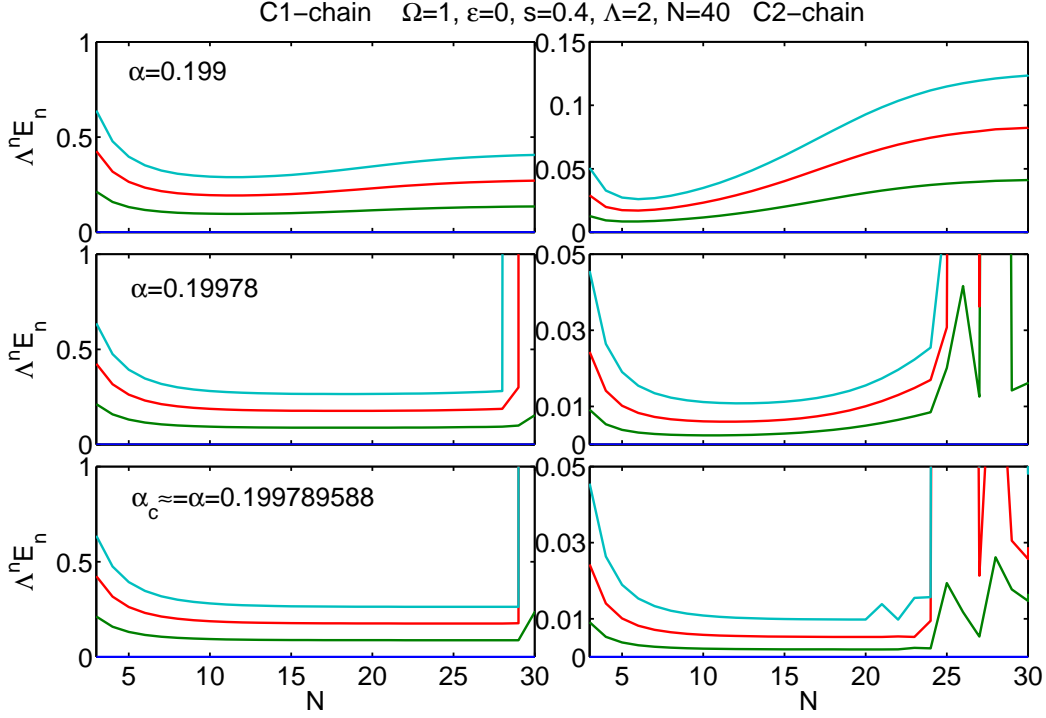


Figure 17: Energy-level flow diagrams with the four lowest lying energy-levels of the DHO calculated with the modified VMPS procedure of section 2.3.6 for a C1 chain (left) and a C2 chain (right). When the dissipation strength α approaches α_c (from top to bottom), we observe the development of a constant energy-level flow over a number of different chain lengths, for both C1 and C2 chains. For every chain length we need a separate calculation due to the energy correction on the last site of the chain. The non-smooth behavior for longer chain lengths is attributed to convergence problems.

one-particle spectrum λ_0 for all calculated α -values. E.g., for $\alpha = 0, 199789588$, we find $\lambda_0 = 8.783 \cdot 10^{-2}$, whereas the energies ε_n of the four lowest levels of the many-particle spectrum are $\varepsilon_0 = 0$ (blue line), $\varepsilon_1 = 8.783 \cdot 10^{-2} = 1\lambda_0$ (green line), $\varepsilon_2 = 1.757 \cdot 10^{-1} = 2\lambda_0$ (red line) and $\varepsilon_3 = 2.635 \cdot 10^{-1} = 3\lambda_0$ (cyan line) and can therefore be constructed exactly by taking the lowest eigenenergy of the one-particle spectrum zero times, once, twice, and three times.

For a C2 chain and $\alpha = 0.199$ far away from the critical coupling strength α_c , we also find that the energy-levels are equidistant and that the flow diagram can be constructed by taking the lowest energy-level of the one particle spectrum not once, once, twice and three times. However, moving closer to α_c , the equidistant behavior one would expect by studying the one-particle spectrum Fig. 15 vanishes. Instead, we observe for a chain length of $N = 20$ and $\alpha \approx \alpha_c$ a ground state energy of the one-particle spectrum of $\lambda_0 = 1.401 \cdot 10^{-5}$, whereas the energy-levels of the many-particle spectrum are $\varepsilon_0 = 0$ (blue line), $\varepsilon_1 = 1.968 \cdot 10^{-3} = \lambda_0$ (green line), $\varepsilon_2 = 5.239 \cdot 10^{-3} = 2\lambda_0$ (red line) and $\varepsilon_3 = 9.811 \cdot 10^{-3} = 3\lambda_0$ (cyan line). Since the lowest level of the one-particle spectrum increases with longer chain lengths and the many particle spectrum stays

constant for different chain lengths, these relations vary for different N . Studying the

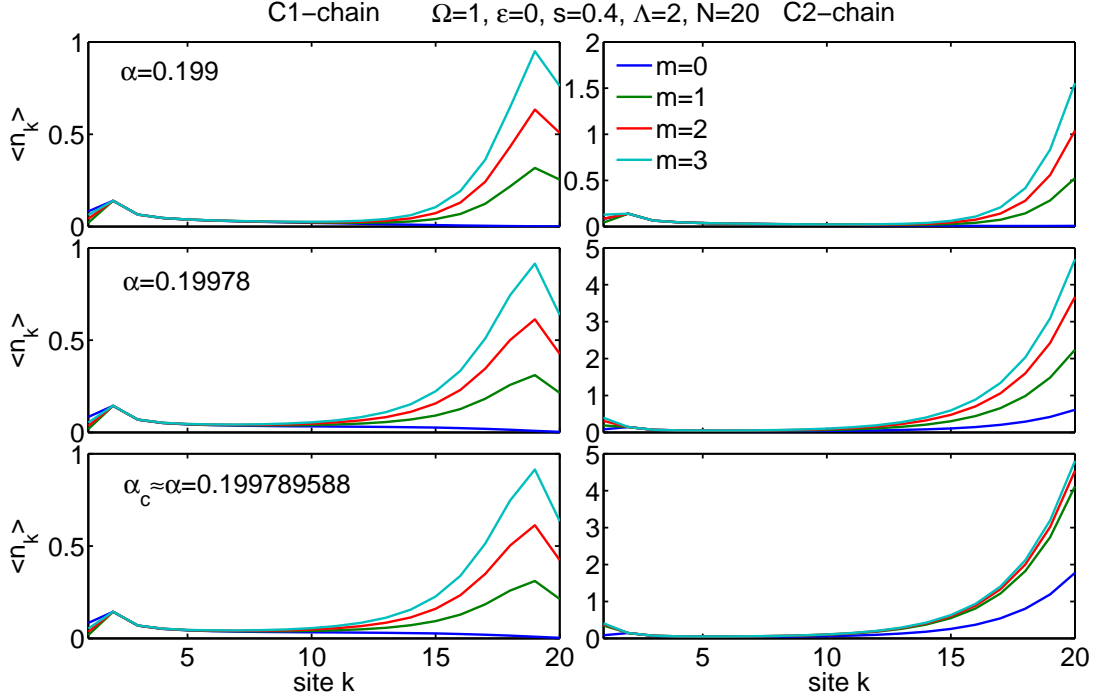


Figure 18: Occupation number $\langle \hat{n}_k \rangle$ along the chain of the $m = 4$ lowest levels obtained with the modified VMPS procedure for a C1 chain (left) and a C2 chain (right) for three different values of α . We note that the occupation number increases towards the end of the chain and that higher levels result in higher occupation numbers. While for a C2 chain, $\langle \hat{n}_k \rangle$ increases for all levels when approaching α_c , it stays the same in case of a C1.

calculated occupation number $\langle \hat{n}_k \rangle_m$ along the chain for the different levels displayed in Fig.18, we note that the occupation number increases with k towards the end of the chain and that $\langle \hat{n}_k \rangle_m$ is larger for higher lying levels. In case of the C1 chain and for results of the C2 chain with $\alpha = 0.199$, we observe a maximal occupation number of comparable magnitude, whereas, when approaching α_c for a C2 chain, the occupation number increases for all levels, even the lowest one. Note the saturation of the increase of $\langle \hat{n}_N \rangle_m$ with increasing m , indicating a possible lack of convergence. This could also be the cause of the unexpected behavior of the energy-level flow diagrams near α_c . However, increasing the upper bond dimension D and the dimension of the local bosonic bases d_k just confirmed previous results.

The non-smooth behavior of the energy levels for longer chains length is caused by convergence problems due to numerical imprecision. This is illustrated in Fig. 19, where we depicted the difference between the energy convergence of a short ($N = 20$) and long chain ($N = 30$). For the short chain, after the first 3 sweeps ($k = 60$ iterations), the energy levels are converged. For the longer chain, we observe jumps in all energy-levels mostly after sweeping back from the right to the left end of the chain. Those occur so often that the system cannot converge.

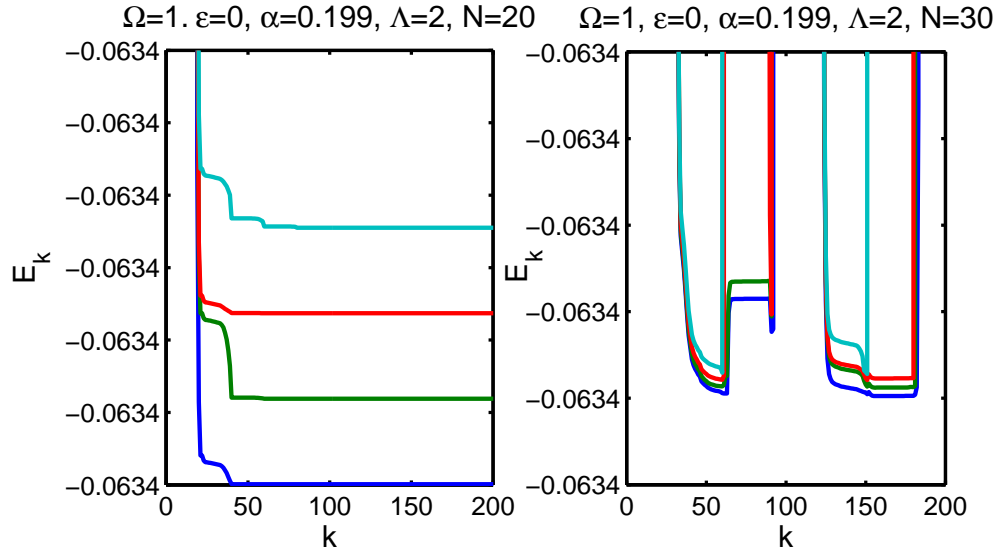


Figure 19: Energy E_k of the lowest four levels calculated at each site of the Wilson chain during several numbers of sweeps plotted against the iteration step k . To illustrate the convergence behavior, the results obtained during consecutive sweeps are merged. For a chain with length $N = 20$, we observe straight convergence of all energy-levels, whereas for $N = 30$ the energy-levels suddenly jump before convergence is reached.

4.2 Spin-boson model

The spin-boson model is one of the most simple non-trivial models for studying competing interactions and consists of a two-state system (e.g. a spin-1/2 impurity) coupled to a bath of non-interacting bosonic degrees of freedom. In the last years, the model has gained a lot of attention because of its wide range of applications for example in quantum dissipation [3, 51], interaction of qubits with the environment [52, 53], cold atom quantum dots [54] or trapped ions [55]. The SBM shows an impurity quantum phase

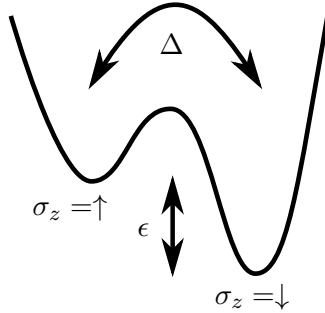


Figure 20: Illustration of the spin-boson model. The two states $\sigma_z = \uparrow$ and $\sigma_z = \downarrow$ differ in energy by the bias ϵ and are connected via the tunneling constant Δ .

transition at zero temperature, which corresponds according to quantum-to-classical correspondence (QCC) to the classical transition of an one-dimensional Ising chain with long ranged interaction. First results from NRG calculations [9, 12, 30] suggested a breakdown of the QCC principle but turned out to be affected by the bosonic truncation and mass flow error [15, 30, 56]. Subsequent works based on quantum Monte Carlo, exact diagonalization or VMPS confirm the validity of quantum-to-classical correspondence. However, the application of VMPS to the SBM is also affected by the neglected TBMs and thus yields the wrong critical exponent x for the susceptibility χ .

In this section, we first give a short overview of the different physical properties of the spin-boson model and show that also for this more complicated model the numerical results obtained with a RWC are in agreement with results from other methods like quantum Monte Carlo, thus confirming the effectiveness of OWCs.

4.2.1 Ground state phases

We already discussed the spin-boson model briefly in the section of bosonic NRG 2.2.1, where we started with the Hamiltonian

$$\hat{H} = \underbrace{\frac{\epsilon}{2}\hat{\sigma}_x - \frac{\Delta}{2}\hat{\sigma}_z}_{\hat{H}_{imp}} + \underbrace{\sum_q \omega_q \hat{a}_q^\dagger \hat{a}_q}_{\hat{H}_{bath}} + \underbrace{\frac{\hat{\sigma}_z}{2} \sum_q \lambda_q (\hat{a}_q + \hat{a}_q^\dagger)}_{\hat{H}_{coupling}} . \quad (4.39)$$

The impurity consist of a spin 1/2 system described by the Pauli matrices, coupled linearly to a bath of bosonic modes represented by harmonic oscillators with corresponding creation \hat{a}_q^\dagger and annihilation \hat{a}_q operators and frequencies ω_q . ϵ denotes an energy level bias in coupling direction while the tunneling amplitude Δ describes the interaction

of the two eigenstates of the spin-1/2 system. As already discussed in chapter 3, the system is completely described by the spectral function

$$J(\omega) = \pi \sum_q \lambda_q^2 \delta(\omega - \omega_q) . \quad (4.40)$$

Again, we choose the power-law parametrization for the low-temperature behavior up to a critical frequency $\omega_c = 1$

$$J(\omega) = 2\pi\alpha\omega_c^{1-s}\omega^s, \quad 0 < \omega < \omega_c, s > 0 . \quad (4.41)$$

The dissipation strength is given by the dimensionless parameter α while s takes on the role of an effective dimension, determining the low-energy density of states. We can distinguish three different parameter regimes for the SBM: *ohmic* ($s = 1$), *sub-ohmic* $s < 1$ and *super-ohmic* $s > 1$. To apply the VMPS procedure on the SBM, we discretize the model and map it onto a semi-infinite chain (see Sec. 2.2.2 and Sec. 2.2.3)

$$\hat{H}_{chain} = \hat{H}_{imp} + \sqrt{\frac{\eta_0}{\pi}} \frac{\hat{\sigma}_z}{2} (\hat{b}_0 + \hat{b}_0^\dagger) + \sum_{k=0}^{\infty} \left[\epsilon_k \hat{b}_k^\dagger \hat{b}_k + t_k (\hat{b}_k^\dagger \hat{b}_{k+1} + \hat{b}_{k+1}^\dagger \hat{b}_k) \right] . \quad (4.42)$$

In all following calculations, we choose the upper bond dimension $D = 40$ and the dimension for the optimal bosonic basis $d_{opt} = 16$, if not stated otherwise.

At zero temperature and zero bias, we can distinguish two different regimes differing by the type of the occurring ground state. In the first case, the interplay between the dissipation and the spin precession is dominated by the coupling α yielding a strongly localized ground state with finite magnetization $\langle \hat{\sigma}_z \rangle \neq 0$ because the spin localizes in direction of the bath coupling. In this case, the ground state is two-fold degenerate and exhibits spontaneous symmetry breaking. In the second case, the coupling is too weak to localize the spin, thus generating a weakly coupled, delocalized ground state with no magnetization $\langle \hat{\sigma}_z \rangle = 0$ and no degeneracy of the ground state. In Fig. 21, a VMPS energy-flow diagram for $s = 0.4$ is displayed, where we can see that both types of ground states correspond to stable fixed points.

The definition in mind, panel (a) shows the energy-flow in the delocalized regime with a non-degenerate fixed point at the latest iterations, while panel (c) shows the flow into the localized regime. Separating this two regimes, the quantum phase transition in the sub-ohmic case corresponds to another fixed point shown in panel (b), called critical fixed point. The fixed point behavior of the system depends on the the interplay between coupling α , tunneling coefficient Δ and the exponent of the spectral function

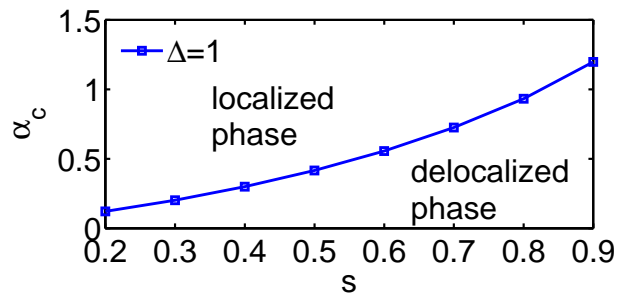


Figure 22: VMPS phase diagram showing a transition from the delocalized ($\alpha < \alpha_c$) to the localized phase ($\alpha > \alpha_c$).

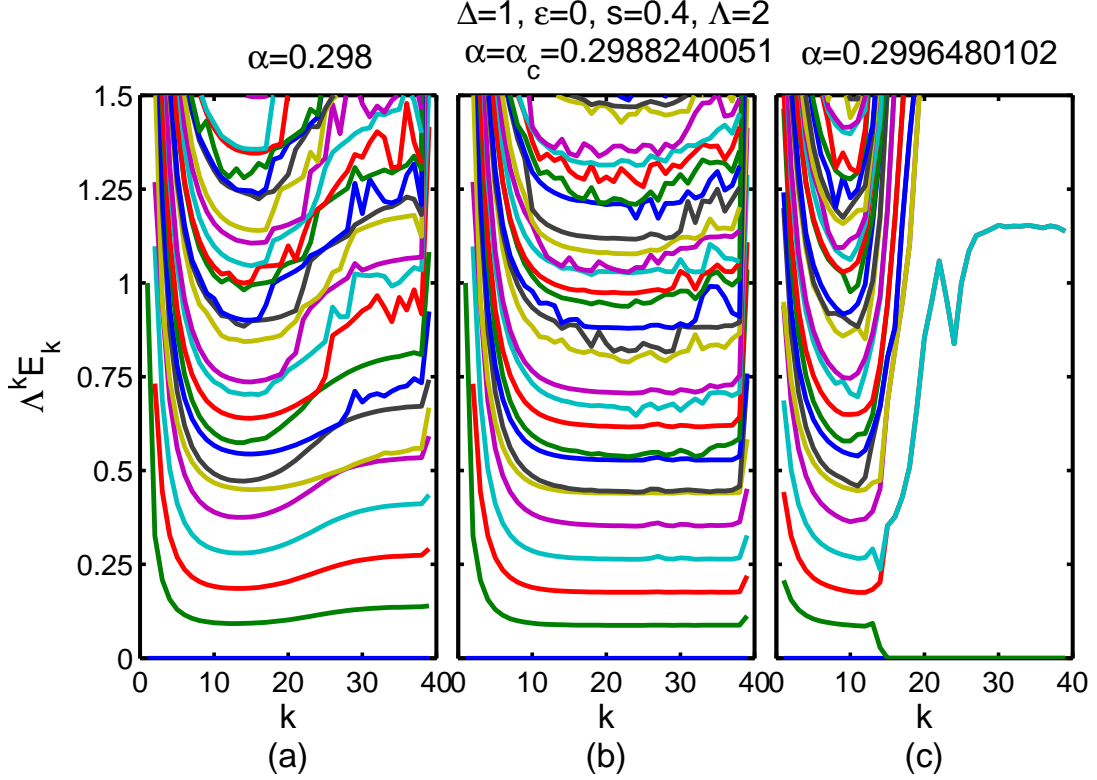


Figure 21: VMPS energy-level flow diagram for the sub-ohmic SBM with $s = 0.4$. Panel (a) and (c) show the flow from the critical towards the delocalized and localized fixed point respectively, while in (b) the system is located at the critical fixed point directly at the phase boundary. In this case, the smooth energy-level flow is characteristically.

s. Fig. 22 illustrates the resulting phase diagram. The critical coupling α_c denotes the appearance of the fixed point corresponding to the phase transition from the localized to the delocalized regime. Since the exponent s of the spectral function determines the density of states of the bosonic bath, it also influences how strong the coupling has to be in order to localize the spin. Thus, for larger s a larger dissipation strength α is required to localize the spin. The critical coupling reaches its maximum in the ohmic regime for $s = 1$, whereas in the super-ohmic regime no phase transition occurs since the system always delocalizes. The tunneling between the two eigenstates of the spin system has the opposite effect, i.e. a delocalization of the spin. Therefore, with increasing tunneling strength, α_c increases.

4.2.2 Determining the critical coupling strength

There exist a number of ways to determine the critical coupling strength α_c numerically. One approach developed by [57] is based on the behavior of the bosonic ground state occupation number $\langle \hat{n}_k \rangle$ along the chain. In the localized phase, the occupation number increases towards the end of the chain as illustrated in Fig. 23(a), whereas in the delocalized phase the number of bosons decays steadily. Thus α_c can be found by

tuning the coupling strength such that the occupation number stays constant along the chain, apart from the sharp decay at the end of the chain. However, this approach does not work any more when using OWCs which can be seen in Fig. 23(b). Since the energy corrections due to the TBMs lower the on-site energy of the last site of the C2 chain (Sec. 4.1.2), the occupation number always increases towards the end of the chain independent of the investigated parameter regime.

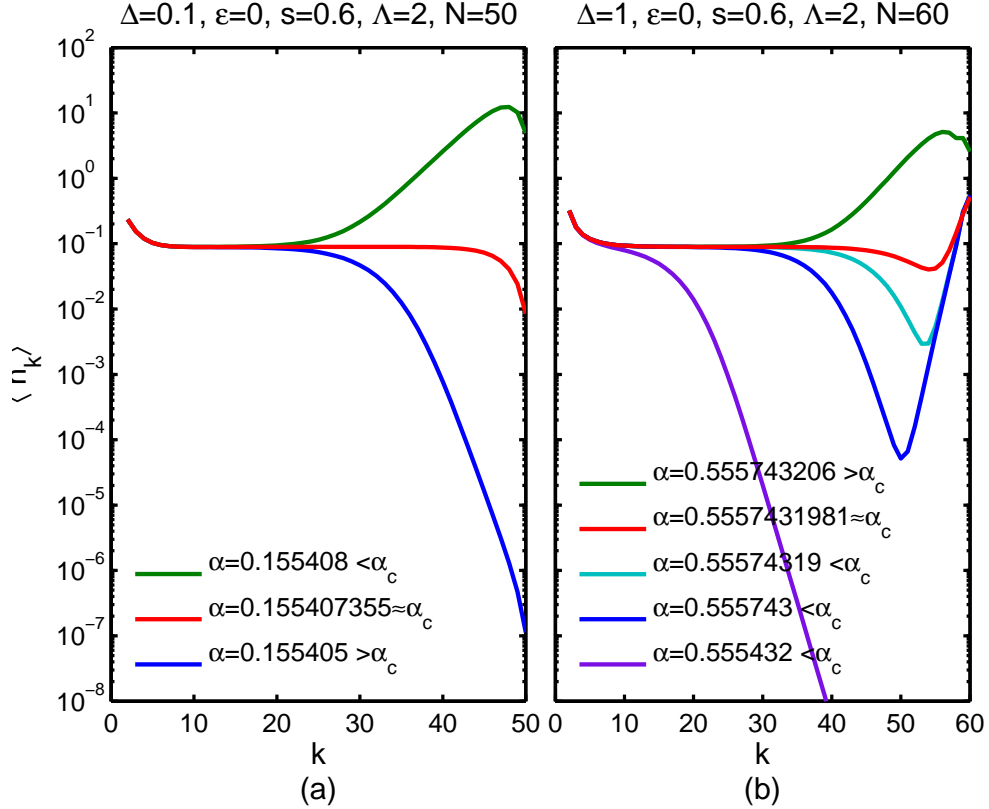


Figure 23: (a) Behavior of the bosonic occupation number $\langle \hat{n}_k \rangle$ along the SWC for the sub-ohmic SBM with $s = 0.6$ in the delocalized (blue), localized (green) phase and at the quantum phase transition (red). The characteristic behavior can be used to determine α_c for which the phase transition occurs, (b) Bosonic occupation number for a RWC with $s = 0.6$. While the behavior in the localized phase (green) does not change qualitatively compared to a SWC, the behavior in the delocalized regime is different. Far away from α_c the occupation number decreases exponentially along the chain, but near the critical coupling $\langle \hat{n}_k \rangle$ starts increasing towards the end of the chain (blue curves) with the same number of bosons on the last chains sites. For $\alpha \approx \alpha_c$ (red) determined via energy-level flow diagrams we observe the same behavior.

In the context of the dissipative harmonic oscillator, we encountered that the susceptibility shows a characteristically different behavior below and above the critical coupling strength. This is also the case for the spin-boson model. With decreasing temperature, the susceptibility $\chi(T)$ increases with a typical power-law behavior near the critical coupling strength $\alpha = \alpha_c$. The susceptibility saturates at a constant value for low temperatures in the delocalized regime and diverges in the localized regime.

Since there exists no analytic expression for the susceptibility, α_c has to be determined numerically by calculating $\chi(T)$ for different coupling strengths. However, this is numerically expensive, because we have to evaluate the derivative $\chi = \frac{d\langle\hat{\sigma}_z\rangle}{d\epsilon}$ numerically by calculating the expectation value $\langle\hat{\sigma}_z\rangle$ for different biases ϵ . Additionally, OWCs make it necessary to use separate VMPS calculations for different chain lengths corresponding to different temperatures T .

Another approach to determine α_c in the Wilson chain setup of the SBM uses the characteristics of the energy-level flow diagrams. As illustrated in Fig. 21, they display a crossover from the critical to the localized $\alpha > \alpha_c$ or delocalized ($\alpha < \alpha_c$) fixed point at site N^* . This crossover can be characterized by a low-energy scale $T^* \propto \Lambda^{-N^*}$ allowing us to determine α_c [20]. In the limit of $\alpha \rightarrow \alpha_c$, the system is located at the critical fixed point, hence $N^* \rightarrow \infty$. For our calculations we employ the latter method to determine α_c .

To access critical properties, we need a resolution down to the low-energy scale $T^* \propto |\alpha - \alpha_c|^\nu$ as discussed in [14], where ν is the critical exponent of the correlation length. Since the energy scale accessible by a Wilson chain scales with Λ^{-N} , both ν and N govern for the accuracy of the determination of α_c . Thus, for an accuracy of 10^{-a} we need a minimum length of

$$N \propto a\nu \frac{\ln(10)}{\ln(\Lambda)}. \quad (4.43)$$

4.2.3 Critical exponents

The physics of systems near critical points in continuous phase transitions is in general well described by the behavior of some basic variables. Near the phase transition, these variables can be characterized by their power-law exponents which are the so-called *critical exponents*. One appealing example is a ferromagnet, whose temperature is decreased until it reaches the critical temperature T_c . Above T_c , the magnetization m of the ferromagnet changes linearly with respect to a small applied magnetic field h . Below T_c , the magnetization follows a super-linear power-law. If we define the susceptibility $\chi = \frac{dm}{dh}$, we observe that $\chi \propto h^{1/\delta-1}$ for $h \rightarrow 0$ and can define the critical exponent δ . Such critical exponents describe the degree of singularity and specify the critical phenomena as we will see in the following discussion of the SBM. In table (1), we summarize the critical exponents used to describe the quantum phase transition of the SBM and their definitions. We mentioned already that the SBM displays a quantum

Table 1: Critical exponents used to describe the SBM.

physical Quantity	Definiton	Condition
Local magnetization	$\langle\hat{\sigma}_z\rangle \propto \alpha - \alpha_c ^{-\beta}$	$ \alpha - \alpha_c \rightarrow 0, \epsilon = 0, T = 0$
Local susceptibility	$\chi \propto \alpha - \alpha_c ^{-\gamma}$	$ \alpha - \alpha_c \rightarrow 0, \epsilon = 0, T = 0$
Local magnetization	$\langle\hat{\sigma}_z\rangle \propto \epsilon ^{1/\delta}$	$\alpha = \alpha_c, \epsilon \rightarrow 0, T = 0$
Correlation length	$\xi \propto \alpha - \alpha_c ^{-\nu}$	$ \alpha - \alpha_c \rightarrow 0, \epsilon = 0, T = 0$
Local susceptibility	$\chi \propto T^{-x}$	$\alpha = \alpha_c, \epsilon = 0, T \rightarrow 0$

phase transition in the regime of $0 < s < 1$ at zero temperature between the localized

and delocalized phase. Due to quantum-to-classical correspondence, it is possible to predict certain features of the SBM analog to the behavior of the one-dimensional Ising chain. First of all, since s determines the power law of the spectral function and thus the density of states near $\omega = 0$, it acts as an effective dimension with an upper and lower critical dimension at $s = 1/2$ and $s = 1$, as showed by Luitjen and Blöte [58]. Therefore, for $0 < s < 1/2$ the effective dimension is above the upper critical dimension, resulting in mean-field behavior for the SBM. This is reflected in the critical exponents being

$$\beta = \frac{1}{2}, \quad \delta = 3, \quad \nu = \frac{1}{s}, \quad \gamma = 1, \quad x = \frac{1}{2}. \quad (4.44)$$

If s lies between its upper and lower critical dimension, $1/2 < s < 1$, the system shows non-trivial critical behavior. The critical exponents obey so-called hyperscaling relations

$$\delta = \frac{1+x}{1-x}, \quad 2\beta = \nu(1-x), \quad x = s. \quad (4.45)$$

Finally, for $s = 1$ the quantum phase transition shows a diverging correlation length and the absence of a critical fixed point. This typical behavior when reaching the lower critical dimension is called a Kosterlitz-Thouless phase transition. As already

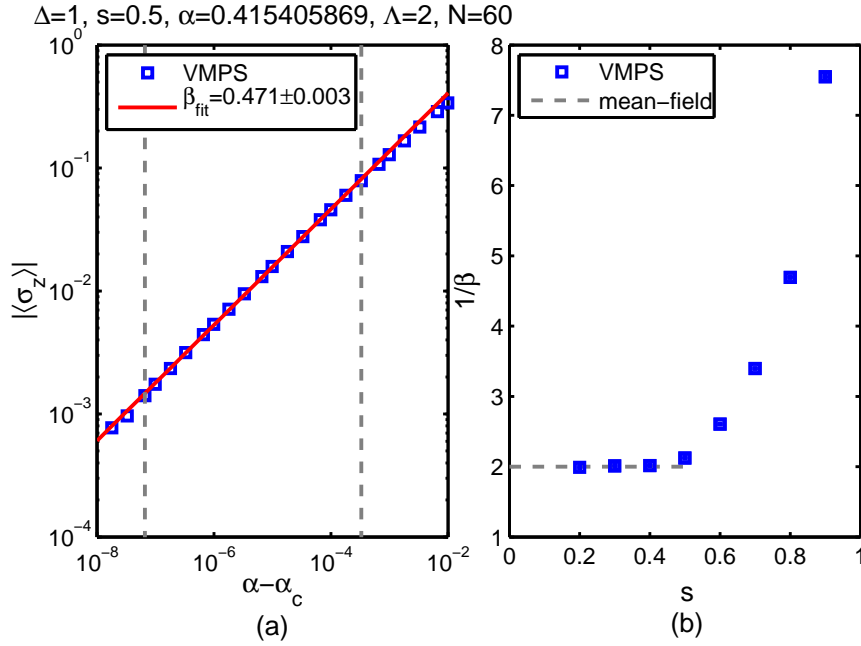


Figure 24: (a) Absolute value of the magnetization $|\langle \hat{\sigma}_z \rangle|$ for different values of α and $s = 0.5$ (blue squares). A non-linear fit (red) within the dashed lines shows the power-law behavior over four orders of magnitude with the exponent β_{fit} . Parameters above the panel. (b) Determined values of β (blues squares with error bars) for different values of s in the sub-ohmic regime of the SBM. The predicted mean-field behavior above the upper critical dimension $0 < s < 1/2$ is indicated by a dashed line and confirmed by the numerical results.

mentioned, the first NRG results from Bulla et al.[9] in 2003 confirmed the Kosterlitz-Thouless transition at $s = 1$ but predicted hyperscaling relations for the entire sub-ohmic regime $0 < s < 1$ thus contradicting the quantum-to-classical correspondence principle. These unexpected results, even reinforced by further works on the SBM and the Bose-Fermi Kondo model [10, 11], lead to further studies based on other numerical methods like quantum Monte Carlo [12], exact diagonalization [13] and VMPS [14] which found the predicted mean-field exponents for $0 < s < 1/2$. The reason for the misleading results of NRG were traced back to the two limitations of bosonic NRG: the truncation and the massflow error [13, 30]. Consequently, the mean-field value for the critical exponents $\delta = 3$ and $\beta = 1/2$ were found [14] with a displayed OBB according to Sec. 2.3.3. Fig. 24 and Fig. 25 displays δ and β as function of s obtained with VMPS and OWCs showing that our method is able to reproduce these results.

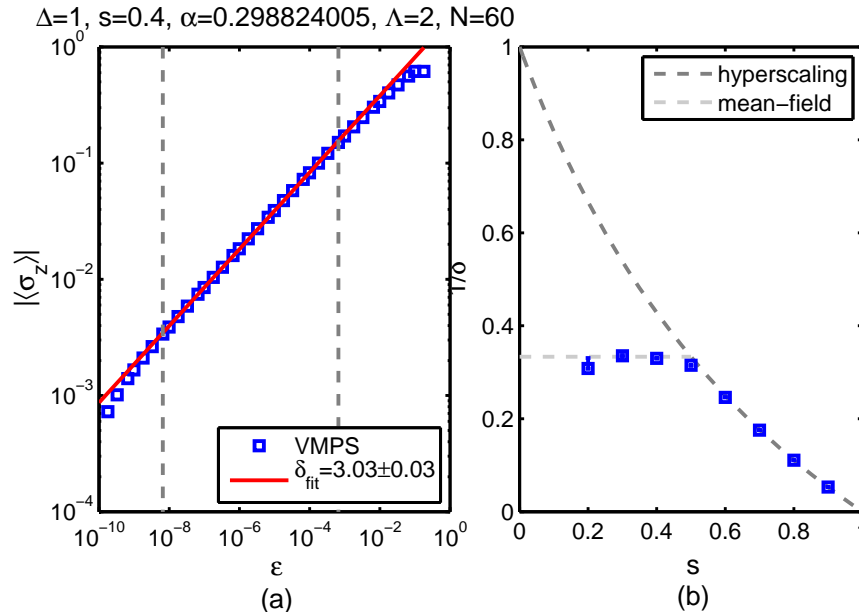


Figure 25: (a) Absolute value of the magnetization $|\langle \hat{\sigma}_z \rangle|$ for different values of ϵ and $s = 0.4$ (blue squares). A non-linear fit (red) within the dashed lines shows the power-law behavior over five orders of magnitude with the exponent δ_{fit} . Parameters above the panel. (b) Determined values of δ (blue squares with error bars) for different values of s in the sub-ohmic regime of the SBM. The predicted mean-field behavior above the upper critical dimension $0 < s < 1/2$ is indicated by a light gray dashed line while the hyperscaling relations for the regime between the lower and upper critical dimension $1/2 < s < 1$ is illustrated by the dark gray line. In both regimes the theoretical and numerical results are in agreement.

4.2.4 Determination of ν with spin-projected displacements

It is also possible to determine the other critical exponents x and ν in the VMPS framework. While x describes the temperature dependence of the susceptibility, ν determines the behavior of the correlation length and thus the low-energy scale

$$T^* \propto |\alpha - \alpha_c|^\nu, \quad (4.46)$$

for which quantum critical phenomena are observable. This energy-scale can be read off the energy-level flow diagrams because T^* is related via $T^* \propto \Lambda^{-N^*}$ to the chain site N^* where the transition from the critical to the localized or delocalized fixed point occurs. However, ν can also be determined from the behavior of the spin-projected displacements δ_i^\uparrow and δ_i^\downarrow . Decomposing the ground state $|G\rangle$ into the eigenbasis of the spin-1/2 system

$$|G\rangle = |G_+\rangle|\uparrow\rangle + |G_-\rangle|\downarrow\rangle, \quad (4.47)$$

we can define

$$\delta_i^\uparrow = \frac{\langle G_+|\hat{x}_i|G_+\rangle}{\langle |G_+|G_+\rangle} \quad (4.48)$$

$$\delta_i^\downarrow = \frac{\langle G_-|\hat{x}_i|G_-\rangle}{\langle |G_-|G_-\rangle}, \quad (4.49)$$

with i denoting the energy level of the discretized star Hamiltonian Eq. (2.27). Fig. 26 displays the spin projected displacements in the sub-ohmic regime near the phase transition, moving from the delocalized to the localized phase. For $\alpha < \alpha_c$ we observe that both spin parts of the ground state wave function have equal weight while the spin

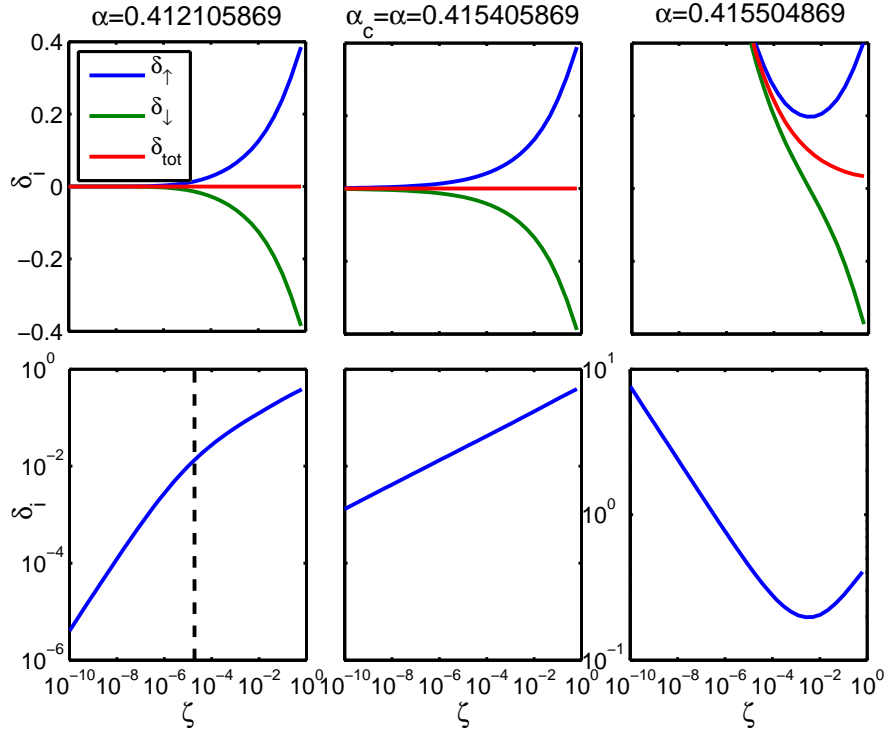


Figure 26: Spin-projected displacement δ_i versus energy ζ for three different α -values in the delocalized, critical and in the localized phase, for $s = 0.5$. Lower panels show the spin-up projected data in a double-logarithmic plot. The dashed black line indicates the transition energy ζ^* , which can be used to determine ν .

projected displacements δ_i^\uparrow and δ_i^\downarrow have opposite sign and same amplitude. This results in a total displacement $\delta_i = \langle G|\hat{x}_i|G\rangle$ of zero, as expected in the localized phase without bias. In the low-energy regime, the spin projected displacements vanish simultaneously, indicating the transition from the critical to the delocalized regime. Due to the last term of the Hamiltonian \hat{H}_{star} and the minimization property of the ground state, the spin-up displacement picks up a negative sign while the spin-down displacement is positive.

Moving closer to the critical coupling, the energy at which the spin-projected displacements vanish moves towards zero. This is the same behavior as for the energy-level flow diagrams where the transition from the critical fixed point to the localized or delocalized occurs at later iterations $N^* \rightarrow \infty$. In the localized phase for high energies, the spin-projected displacements have opposite sign as in the delocalized phase, resulting in a vanishing total displacement. For low energies, they coincide and increase towards low energies such that the total displacement also increases exponentially towards low energies, which corresponds to an increasing displacement toward the end of the Wilson chain. The energy, where δ_i^\uparrow and δ_i^\downarrow coincide, increases when moving away from α_c , indicating an earlier transition to the localized phase.

Studying the spin-projected displacements in the delocalized phase in a double-logarithmic plot (lower panels of Fig. 26), one can see that the low-energy behavior is governed by a different exponent than the high-energy behavior. The energy ζ^* where the behavior changes determines the critical exponent ν . In Fig. 27, we illustrated the calculated exponents for different values of s . The results are in agreement with the theoretical predictions for $0 < s < 1/2$ and follow the hyperscaling predictions in the regime $1/2 < s < 1$ as illustrated in Fig. 28(b).

4.2.5 Susceptibility calculation

Similar to chapter 4.1.6, we can calculate the susceptibility $\chi(T) = \frac{d\langle\hat{\sigma}_z\rangle}{d\epsilon}$ of the spin-boson model via a numerical derivative of the ground state expectation value of the magnetization $|\langle\hat{\sigma}_z\rangle|$, where $\langle\rangle$ indicates the expectation value with respect to the ground state of the VMPS calculation, for a C2 chain. Note that we use different chain lengths N such that the smallest excitation energies are comparable to the temperature T and thus have to run separate VMPS calculations for every temperature. Fig. 28(a) shows the susceptibility plotted over temperature for $s = 0.4$ with the corresponding non-linear fit to determine x . The value of the critical exponent is close the theoretically predicted value $1/2$. In Fig. 28(b), we illustrated x for different values of s . While we find excellent agreement between the hyperscaling relations and the numerical results, for $0 < s < 1/2$ the VMPS results with RWCs are slightly above the mean-field value $x_{MF} = 1/2$. Since the static approximation evaluates the real part of the self-energies at $\omega = 0$, the energy corrections of the on-site energies become increasingly inaccurate for larger energies. The implementation of higher order perturbation theory to capture the effects of the TBMs more correctly, could be improve the numerical results. However, the obtained results are clearly a huge improvement to previous VMPS results where x follows the hyper-scaling relations over the whole sub-ohmic regime.

Having calculated x , we can check the validity of the second hyperscaling relation $x = 1 - 2\beta/\nu$ (Fig. 28(b)). As expected, the results are in good agreement with the

theoretical predictions proving again the accuracy of the employed VMPS method.

VMPS applied to a SWC yields $x = s$ in the whole sub-ohmic regime $0 < s < 1$ by studying the finite-size scaling of the magnetization $|\langle \hat{\sigma}_z \rangle|$ [57]. This turns out to be correct for the hyperscaling regime $1/2 < s < 1$, but not for the mean-field regime $0 < s < 1/2$. The reason for the latter problem is the massflow error. We now present the method used by [57] and show that the finite size effects used to calculate x are not present when using a C2 chain. Assuming that in the limit of infinite system size $L \rightarrow \infty$ $|\langle \hat{\sigma}_z \rangle|$ approaches a well defined value $|\langle \hat{\sigma}_z \rangle|_0$, and that for finite systems we expect corrections to this limiting value in case of a SWC, we can deduce that

$$\begin{aligned} |\langle \hat{\sigma}_z \rangle| &= |\langle \hat{\sigma}_z \rangle|_0 + a \frac{1}{L^p} \\ &= |\langle \hat{\sigma}_z \rangle|_0 + a(\Lambda^{-N})^p . \end{aligned} \quad (4.50)$$

Here we used that the system size is related to the discretization parameter Λ and the length of the Wilson chain N as

$$\frac{1}{L} \propto \frac{1}{\Lambda^N} . \quad (4.51)$$

This behavior can be seen in Fig. 29(a). The magnetization of a gapped system close

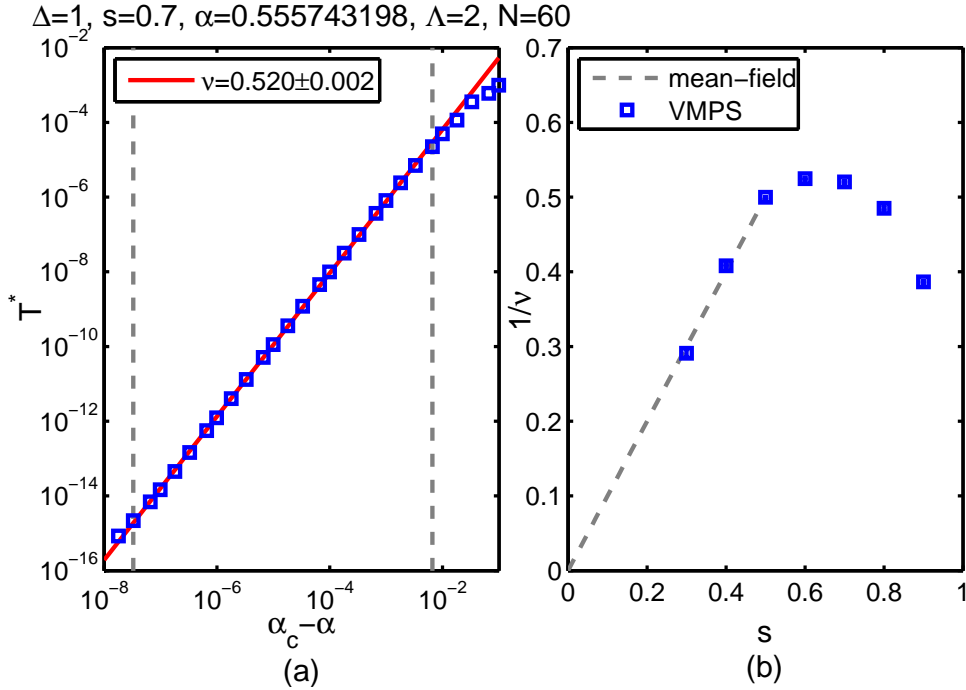


Figure 27: (a) T^* for different values of α and with $s = 0.4$ (blue squares). A non-linear fit (red) within the dashed lines shows the power-law behavior over five orders of magnitude with the exponent ν_{fit} . Parameters above the panel. (b) Determined values of ν (blue squares with error bars) for different values of s in the sub-ohmic regime of the SBM. The predicted mean-field behavior above the upper critical dimension $0 < s < 1/2$ is indicated by a light gray dashed line and in agreement with the numerical results.

to a critical fixed point scales as $|\langle \hat{\sigma}_z \rangle| \propto \bar{\Delta}^{(1-x)/2}$ [60], where $\bar{\Delta}$ is a finite energy gap. We can relate the exponent p of the finite size corrections in Eq. (4.50) to x , because for a SWC the low-energy cut-off Λ^{-N} acts as an effective energy gap [57],

$$(\Lambda^{-N})^p = (\Lambda^{-N})^{(1-x)/2}, \quad (4.52)$$

which gives $x = 1 - 2p$. In contrast, since for OWC the TBMs are included completely for any chain length N , the system stays at the critical coupling strength α_c . Thus, the finite size effect vanishes and $|\langle \hat{\sigma}_z \rangle|$ stays zero for all N . This behavior is indeed obtained numerically, as illustrated in Fig. 29(b).

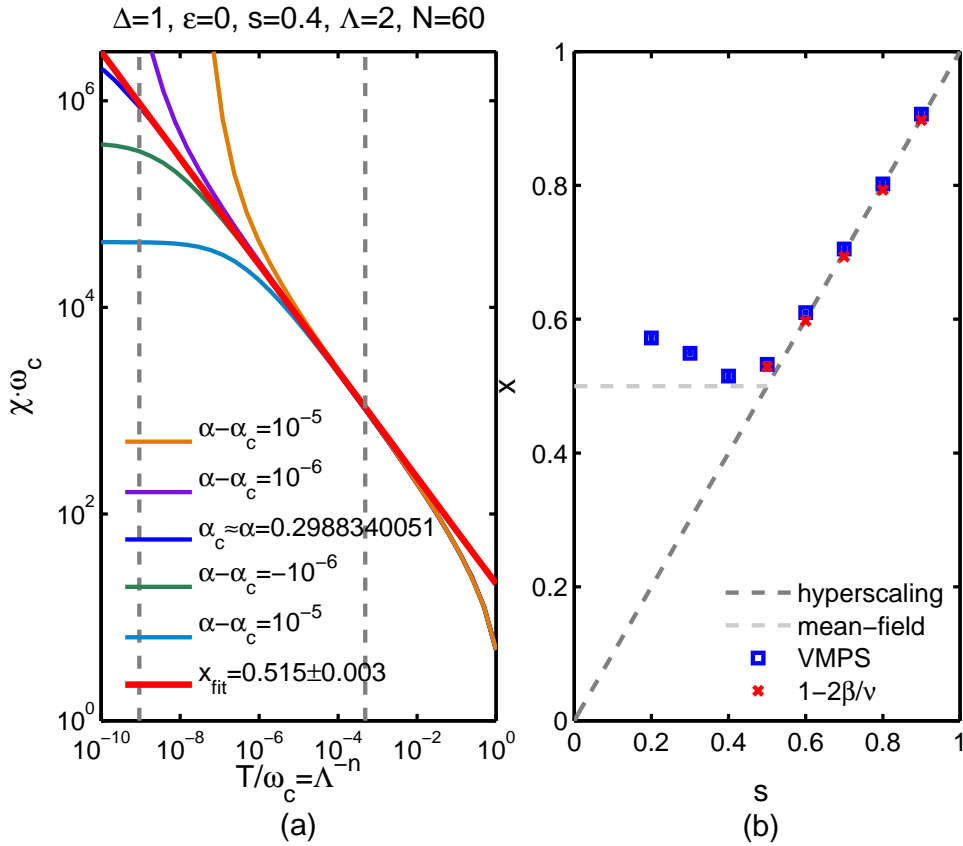


Figure 28: (a) Susceptibility χ for a RWC with $s = 0.4$ and α values below and above the critical coupling strength. For $\alpha \approx \alpha_c$ the susceptibility shows a power-law behavior with the exponent x which is determined by a non-linear fit (red). As α is lowered farther below α_c , the susceptibility becomes temperature independent for $T \rightarrow 0$ and saturates at a lower value of χ , in contrast, the susceptibility diverges if the dissipation strength is above α_c . (b) Behavior of the critical exponent x for different values of s obtained with VMPS (blue squares) and via the hyperscaling relation $x = 1 - 2\beta/\nu$ (red crosses). Using RWCs, the critical exponent is in good agreement with the hyperscaling predictions for $1/2 < s < 1$ and close to but above the analytic predictions in the regime $0 < s < 1/2$. The increasing discrepancies of theoretical predictions and numerical results for small s values is presumably due to the static approximation.

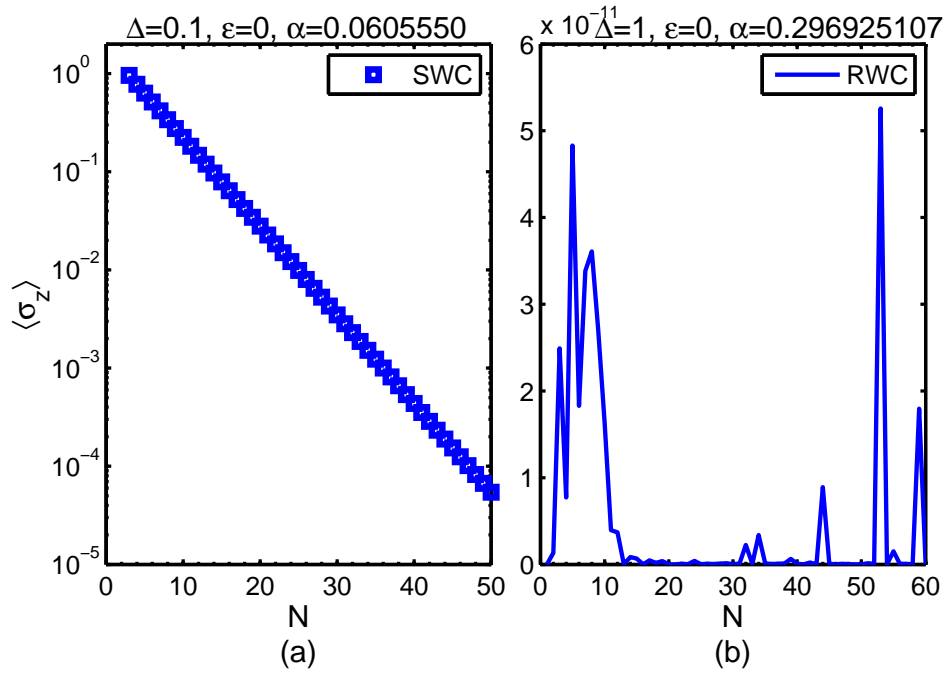


Figure 29: (a) Magnetization for different chain lengths for a SWC with $s = 0.4$ and $\alpha \approx \alpha_c$. The critical coupling strength is determined for a chain with length $L = 50$. Because of the missing TBMs, α_c is different for every chain with a different chain length. The slope of $\langle \sigma_z \rangle$ can be used to determine x which follows the hyperscaling relations over the entire sub-ohmic spectrum $0 < s < 1$. (b) Magnetization for different chain lengths for a RWC with $s = 0.4$ and $\alpha \approx \alpha_c$. Because the TBMs are included in the RWC, α_c is the same for every chain length. This results in $\langle \sigma_z \rangle$ being zero for all N .

5 Conclusion

Since Leggett et al. popularized the spin-boson model in 1987 in the context of quantum dissipation [3, 4], it has been applied to a variety of physical systems from biophysics (e.g. electron transfer processes in biomolecules [59]), over condensed matter (e.g. cold atom quantum dots [54]) to quantum information (e.g. noisy qubits [53]). Because an interacting systems is considered, the model displays a high degree of complexity, not solvable by most of the analytic approaches. To describe the underlying physics and especially critical phenomena of such bosonic models, one has to rely on numerical first-principle methods such as the Numerical Renormalization Group (NRG) [5, 6] and the Density Matrix Renormalization Group (DMRG) [7, 8].

However, the investigation on the first bosonic quantum impurity model showed huge discrepancies between analytic predictions and numerical results obtained with NRG [9, 10, 11], which could be partially be fixed by DMRG application [15, 57]. This thesis builds on this methodical problem and pursued two goals: (i) to present the construction of an improved Wilson chain, called open Wilson chain (OWC), which can be used for NRG and DMRG to capture the physics of impurity quantum systems completely. (ii) to investigate two bosonic quantum impurity model with OWCs, namely the dissipative harmonic oscillator and the spin-boson model.

We started this thesis (chapter 2) with an introduction to the numerical methods used in this thesis: Matrix Product States (MPS), the Numerical Renormalization Group (NRG) and Variational Matrix Product States (VMPS). Additionally, we presented a variation of VMPS to determine not only the ground state but an arbitrary number of the lowest lying states. Afterwards, we discussed the iterative construction of open Wilson chains (OWC) where each site is coupled to a bath of its own. The influence of those baths on the Wilson chain parameters is partly neglected in standard Wilson chains. A simple implementation of these truncated bath modes (TBM) into the setup of NRG and VMPS via a static approximation, dubbed reduced Wilson chains (RWC), was introduced in the end of the chapter.

In chapter 4, we used RWCs on two models: the dissipative harmonic oscillator (DHO) and the spin-boson model (SBM). Whereas the DHO investigated with VMPS or NRG and a standard Wilson chain (SWC) displayed a temperature depending susceptibility, we showed that VMPS and a RWC including all TBMs were able to describe the temperature-independent susceptibility correctly. Additionally, we demonstrated that the critical coupling strength of the DHO is in agreement with theoretical predictions when using RWCs.

The application of VMPS and a RWC to the spin-boson model showed that the critical properties of the system were in agreement with the predictions of the quantum-to-classical correspondence. While VMPS applied to a SWC were able to determine the critical exponent x of the susceptibility via finite-size effects for limited parts of the parameter regime, these effects were not present anymore using RWCs. Moreover, calculating the susceptibility directly, we demonstrated that the usage of RWC led to the predicted behavior of the critical exponent x in the whole sub-ohmic regime, with only small derivations for small bath exponents s .

Two possible path of topics for future research can be distinguished. On the one

hand, the improvement of the presented incorporation of the OWCs into NRG and VMPS in form of a more sophisticated usage of perturbation theory to calculate the effects of the TBMs. Although the simple static approximation led to theoretical predicted results in the case of the DHO, for the SBM we observed small derivations indicating that this approach possibly overestimates the influence of the TBMs. On the other hand, the bath describing the environment is discretized at the outset in NRG and DMRG applications such that a Wilson chain of any finite length actually constitutes of a closed quantum system with a discrete spectrum. These spectra must be broadened by hand after the calculations to obtain smooth spectral functions. The construction of OWC offers a natural prescription for broadening discrete spectra since the presented scheme keeps track of all TBMs.

A Appendices

A NRG and RWCs

The NRG scheme is based on repeating always the same iteration step, namely adding a new site of the Wilson chain and diagonalizing the resulting Hamiltonian. Therefore, all sites are treated similarly. Consequently, we obtain the results of all chain length $N' < N$ when using NRG on a standard Wilson chain of length N .

However, when using a RWC this is not possible anymore with the standard NRG scheme. The static approximation incorporates the effects of the TBMs by evaluation of the self-energies of the baths and slow modes at $\omega = 0$ and shifting the on-site energies of corresponding sites by this amount

$$\tilde{\epsilon}_n = \epsilon_n + \delta\epsilon_n^F + \delta_{nN}\delta\epsilon_N^S, \quad \delta\epsilon_n^{F/S} = \Re\left(\Sigma_n^{F/S}(0)\right). \quad (\text{A.1})$$

Note that the last site N takes on a special role since not only the fast modes but also the slow modes lead to an energy shift. Therefore, we must decide before starting the NRG calculation how long the RWC has to be. At iteration step $n < N$, the Hamiltonian has only information about the baths of fast modes but no information about the slow mode bath describing the low-energy spectrum.

To adapt the NRG procedure to RWCs, we modify the iteration step Eq. (2.33) relating two consecutive Hamiltonians by adding the slow mode shift of the current site and a counter-term to remove the slow mode correction of the previous iteration

$$\hat{H}_{N+1} = \Lambda(\hat{H}_N - \delta_N^S) + \Lambda^{N+1} \left[(\tilde{\epsilon}_{N+1}^F + \delta_{N+1}^S) \hat{b}_{N+1}^\dagger \hat{b}_{N+1} + t_N (\hat{b}_N^\dagger \hat{b}_{N+1} + \hat{b}_{N+1}^\dagger \hat{b}_N) \right]. \quad (\text{A.2})$$

Note that in the occurring energy $\tilde{\epsilon}_N^F = \epsilon_N + \delta\epsilon_N^F$ the fast mode shift is already embedded. With this modification, each site is treated similarly by the NRG procedure and the Hamiltonian H_N incorporates the TBMs via the static approximation in every iteration step.

This adaption is only possible if the basis of eigenstates generated by diagonalizing the Hamiltonian \hat{H}_N do not differ significantly compared to the case where no slow mode shift on the last site is inserted. In the case of the dissipative harmonic oscillator, the results for the susceptibility obtained with the adapted procedure in one calculation and the results of several standard NRG are in perfect agreement.

B Critical exponents SBM

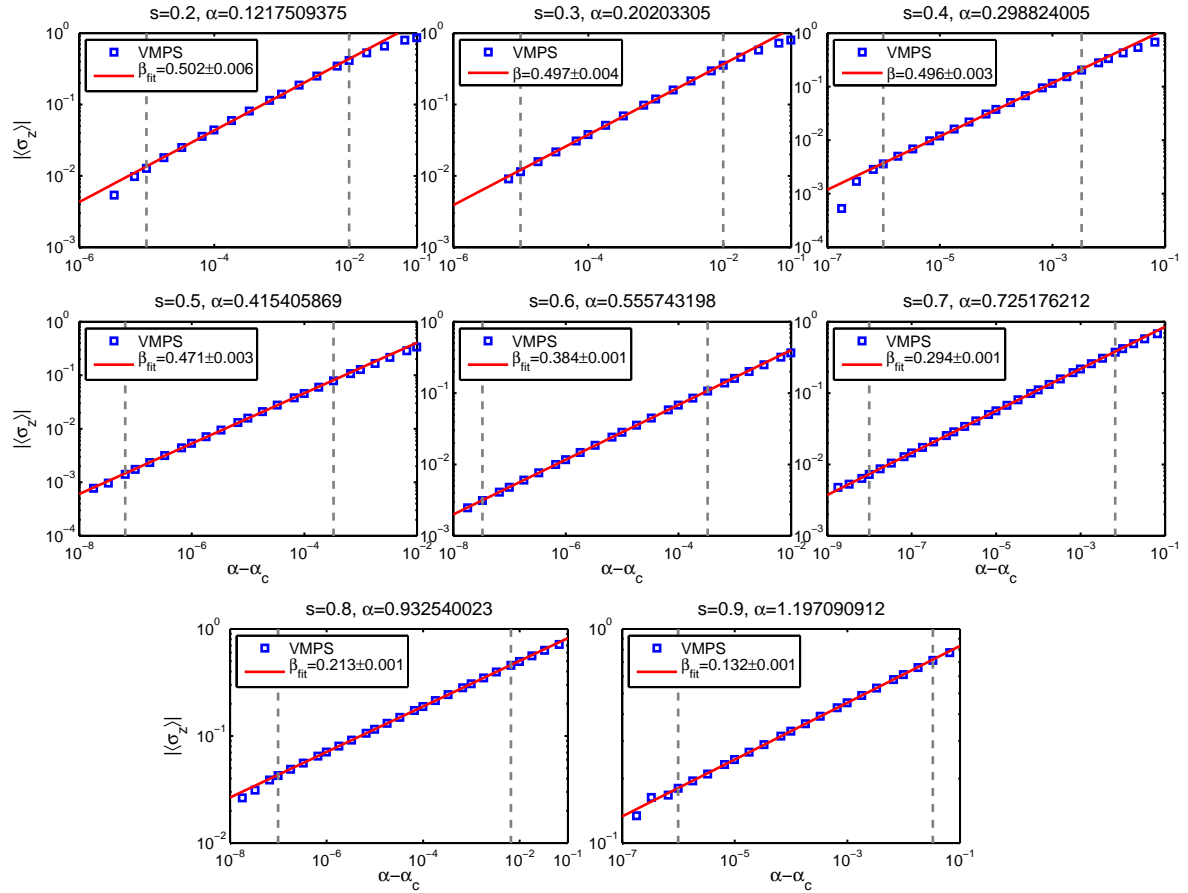
B.1 β 

Figure 30: Magnetization $\langle \sigma_z \rangle$ over bias ϵ for different values of s . The dashed lines show the range used for the non-linear fit (red) to determine the critical exponent β . Parameters used: $\Delta = 1$, $\alpha \approx \alpha_c = 0$, $\Lambda = 2$, $N = 60$.

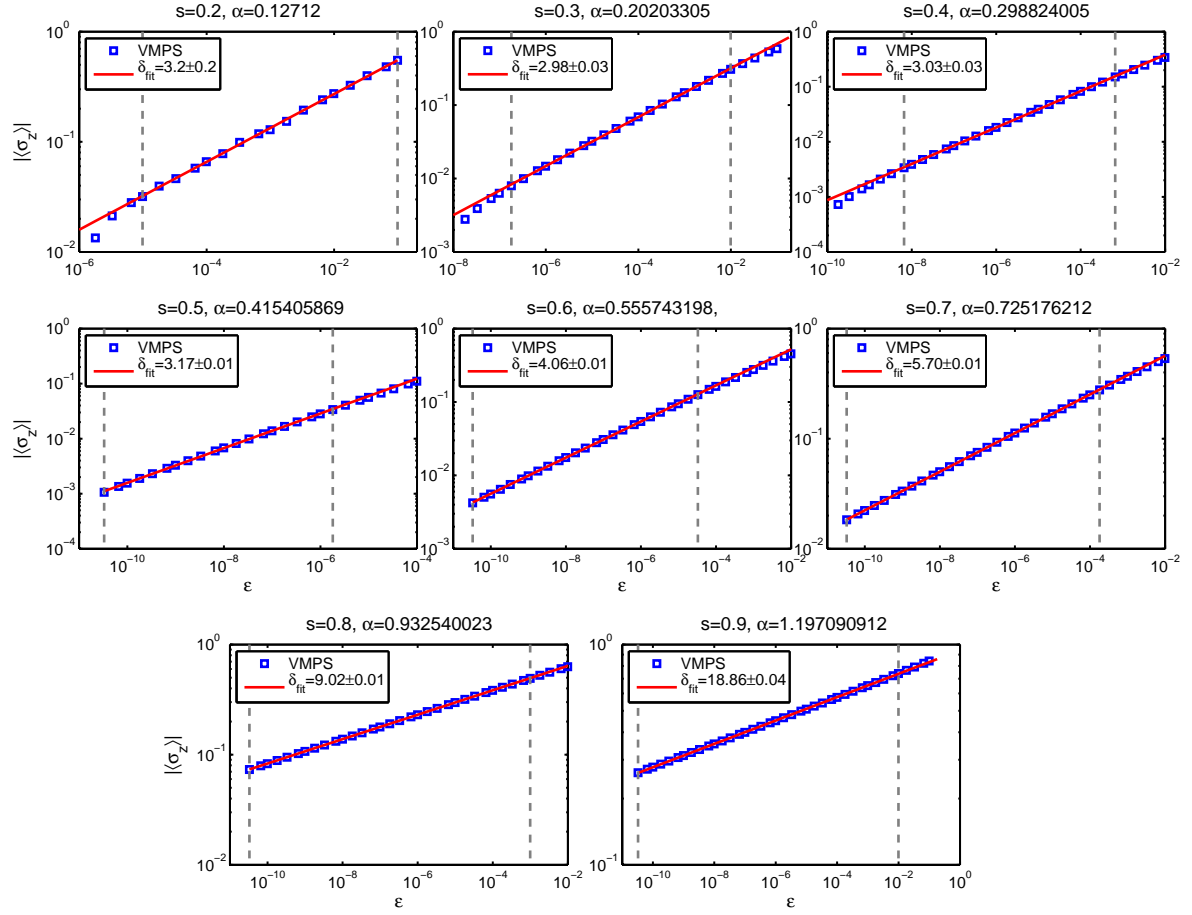
B.2 δ 

Figure 31: Magnetization $\langle \sigma_z \rangle$ over distance to the critical coupling strength α_c for different values of s . The dashed lines show the range used for the non-linear fit (red) to determine the critical exponent δ . Parameters used: $\Delta = 1$, $\epsilon = 0$, $\Lambda = 2$, $N = 60$.

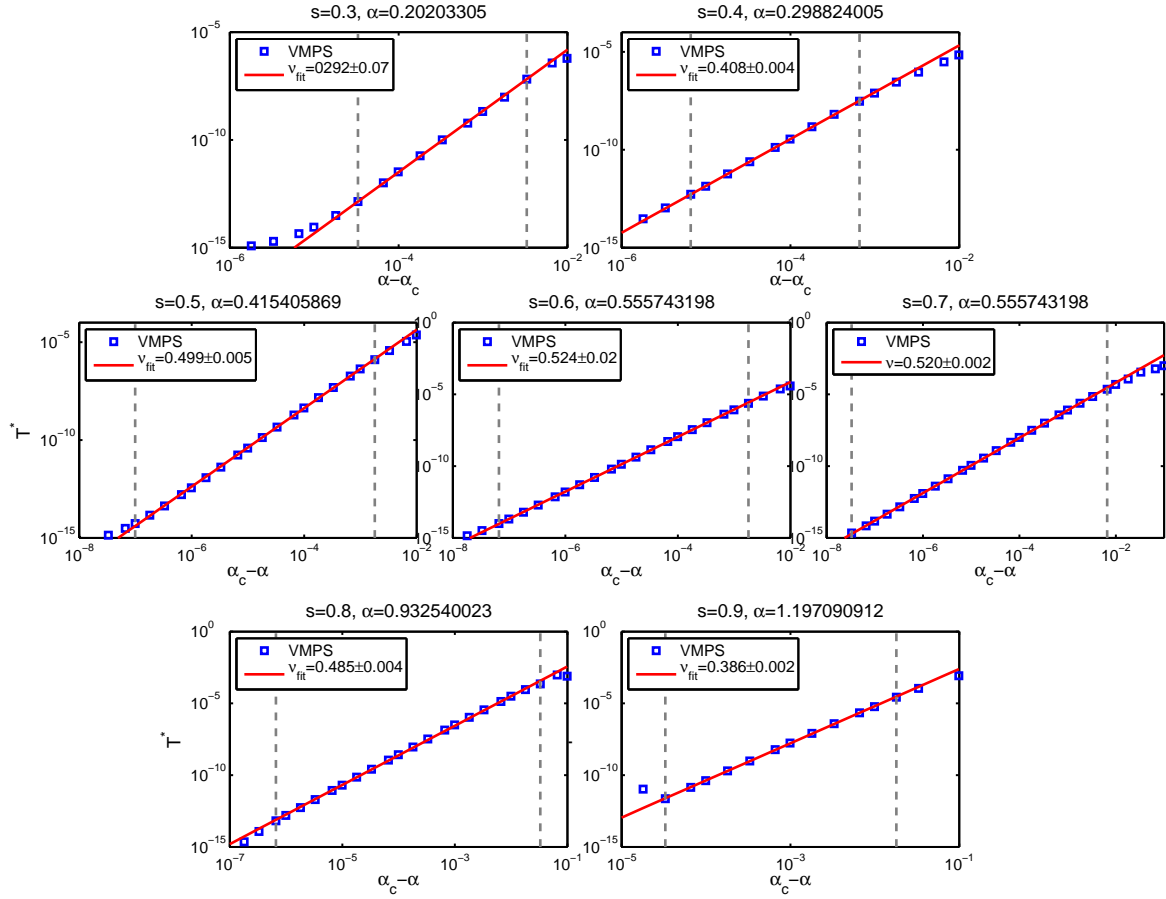
B.3 ν 

Figure 32: T^* over distance to the critical coupling strength α_c to determine the critical exponent ν for different values of s . The dashed lines show the range used for the non-linear fit (red) to determine the critical exponent ν . Parameters used: $\Delta = 1$, $\epsilon = 0$, $\Lambda = 2$, $N = 60$.

B.4 x

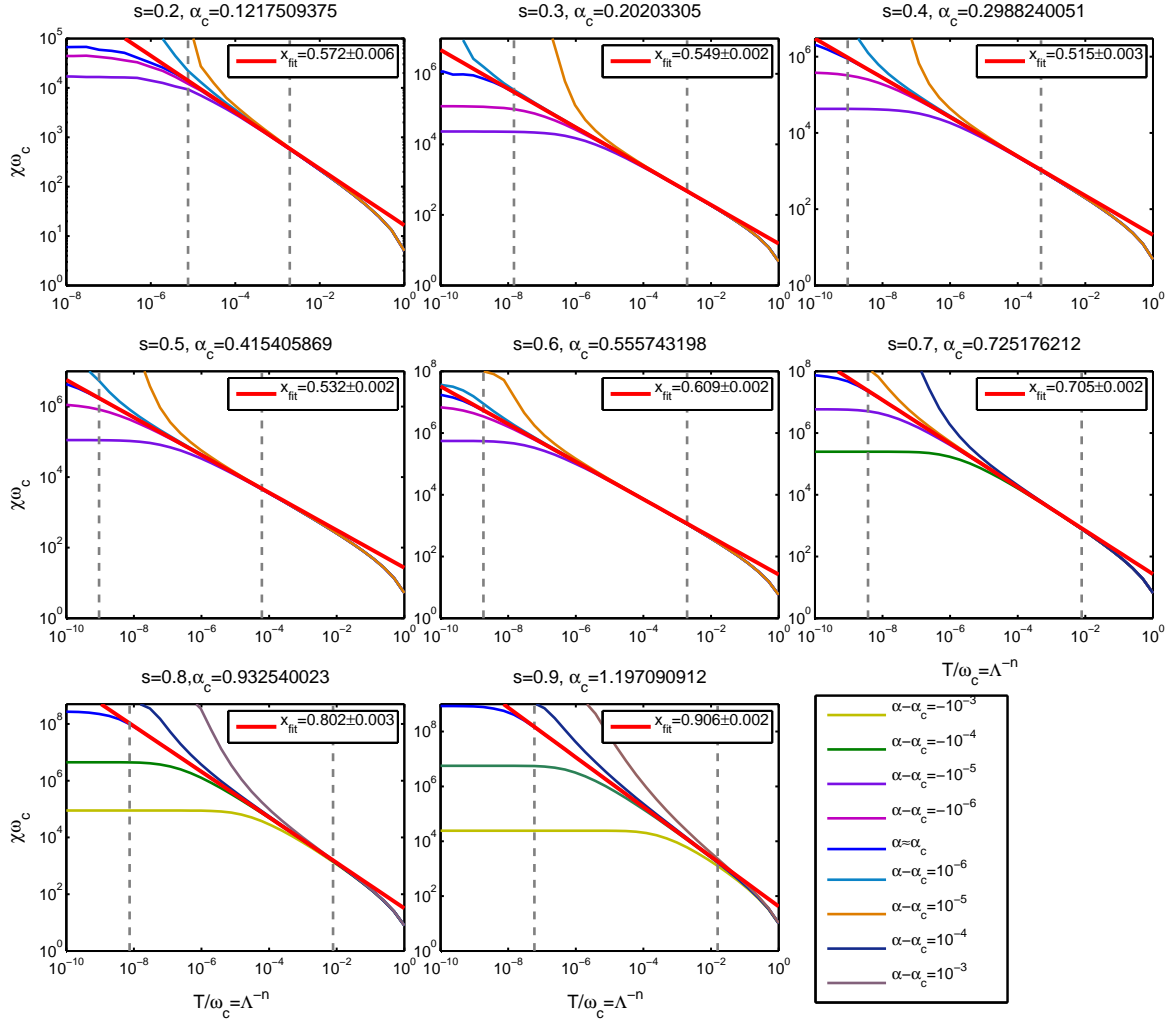


Figure 33: Susceptibility χ over temperature T above and below the critical coupling strength α_c for different values of s . The dashed lines show the range used for the non-linear fit (red) to determine the critical exponent x . Parameters used: $\Delta = 1$, $\epsilon = 0$, $\Lambda = 2$, $N = 60$.

List of Figures

1	Local and global picture of a MPS	4
2	Update formalism of a MPS	6
3	Spectral function of the SBM, discretized and mapped to the semi-infinite chain	11
4	NRG energy-flow diagram of the SBM	13
5	MPS with OBB and optimization procedure	18
6	Convergence of the magnetization and relative error between variational and analytic shift	20
7	VMPS energy-level flow diagram of the SBM	21
8	Variation of a MPS to describe the m lowest states	22
9	Update formalism of an m -level mps	24
10	Iteration to construct an OWC	26
11	Comparison of the Wilson chain parameters	32
12	Behavior of the self-energy and impurity correlator depending on the iteration number	33
13	Overview over different methods used to calculate χ	35
14	Comparison between C2 and BTV susceptibility	37
15	One-particle spectrum of the DHO	40
16	Occupation number of impurity and chain sites for different chain lengths and couplings	42
17	Energy-level flow diagrams for the DHO with the modified VMPS procedure	43
18	Occupation Number of the four lowest levels obtained with the modified VMPS procedure	44
19	Convergence behavior of the lowest four energy-levels for two different chain lengths	45
20	Illustration of the SBM	46
22	VMPS phase diagram showing a transition from the delocalized ($\alpha < \alpha_c$) to the localized phase ($\alpha > \alpha_c$).	47
21	Different fixed points in energy-level flow diagrams of the SBM	48
23	Expectation value of the bosonic occupation value along a SWC and a RWC for different α -values for the SBM	49
24	Critical exponent β for different values of s	51
25	Critical exponent δ for different values of s	52
26	Behavior of spin-projected displacements near the phase transition	53
27	Critical exponent ν for different values of s	55
28	Susceptibility χ for a RWC with $s = 0.4$ and α values below and above the critical coupling strength and behavior of the critical exponent x for different values of s	56
29	Magnetization $\langle \sigma_z \rangle$ for different chain lengths for a SWC and a RWC	57
30	Magnetization $\langle \sigma_z \rangle$ over bias ϵ to determine the critical exponent β for different values of s	61

31	Magnetization $\langle \sigma_z \rangle$ over distance to the critical coupling strength α_c to determine the critical exponent δ for different values of s	62
32	T^* over distance to the critical coupling strength α_c to determine the critical exponent ν for different values of s	63
33	Susceptibility χ over temperature T above and below the critical coupling strength α_c for different values of s	64

References

- [1] P. W. Anderson, G. Yuval, and D. R. Hamann, "Exact results in the Kondo problem. II. Scaling theory, qualitatively correct solution, and some new results on one-dimensional classical statistical models", *Phys. Rev. B* **1**, 4464-4473 (1970).
- [2] A. Hewson, "The Kondo Problem to Heavy Fermions, Cambridge Studies in Magnetism", Cambridge University Press (1997).
- [3] A. J. Leggett, S. Chakravarty, A. T. Dorsey, M. P. A. Fisher, A. Garg, and W. Zwerger, "Dynamics of the dissipative two-state system", *Rev. Mod. Phys.* **59**, 1-85 (1987).
- [4] U. Weiss, "Quantum Dissipative Systems (Second Edition)", Series in modern condensed matter physics, World Scientific Publishing Company, Incorporated (1999).
- [5] K.G. Wilson, "Renormalization group and critical phenomena. I. Renormalization group and Kadanoff scaling picture", *Phys. Rev. B* **4**, 3174-3183 (1971).
- [6] R. Bulla, T.A. Costi, and T. Pruschke, "Numerical renormalization group method for quantum impurity systems", *Rev. Mod. Phys.* **80**, 395-450 (2008).
- [7] S.R. White, "Density matrix formulation for quantum renormalization groups", *Phys. Rev. Lett.* **69**, 2863-2866 (1992).
- [8] U. Schollwöck, "The density-matrix renormalization group", *Rev. Mod. Phys.* **77**, 259-315 (2005).
- [9] R. Bulla, N.-H. Tong and M. Vojta, "Numerical renormalization group for bosonic systems and application to the sub-ohmic spin-boson model", *Phys. Rev. Lett.* **91**, 170601 (2003).
- [10] M. Vojta, N.-H. Tong, and R. Bulla, "Quantum phase transitions in the sub-ohmic spin-boson model: Failure of the quantum-classical mapping", *Phys. Rev. Lett.* **94**, 070604 (2005).
- [11] M. T. Glossop and K. Ingersent, "Numerical renormalization-group study of the Bose-Fermi Kondo model", *Phys. Rev. Lett.* **95**, 067202 (2005).
- [12] A. Winter, H. Rieger, M. Vojta, and R. Bulla, "Quantum phase transition in the subohmic spin-boson model: Quantum monte-carlo study with a continuous imaginary time cluster algorithm", *Phys. Rev. Lett.* **102**, 030601 (2009).
- [13] A. Alvermann and H. Fehske, "Sparse polynomial space approach to dissipative quantum systems: Application to the sub-ohmic spin-boson model", *Phys. Rev. Lett.* **102**, 150601 (2009).
- [14] C. Guo, A. Weichselbaum, J. von Delft and M. Vojta, "Critical and strong-coupling phases in one- and two bath spin-boson models", *Phys. Rev. Lett.* **108**, 160401 (2012).
- [15] M. Vojta, R. Bulla, F. Güttge and F. Anders, "The mass-flow error in the Numerical Renormalization Group method and the critical behavior of the sub-ohmic spin-boson model", *Phys. Rev. B* **81**, 075122 (2010).

- [16] A. Weichselbaum, F. Verstraete, U. Schollwöck, J.I.Cirac, and J. von Delft, "Variational matrix-product-state approach to quantum impurity models", *Phys. Rev. B* **80**, 165117 (2009).
- [17] U. Schollwöck, "The density-matrix renormalization group in the age of matrix product states", *Annals of Physics* **326**(1), 96-192 (2011).
- [18] A. Weichselbaum, "Tensor networks and the numerical renormalization group", Habilitation thesis, LMU Munich, (2012).
- [19] W. Muender, A. Weichselbaum, A. Holzner, J. von Delft and C. L. Henley, "Correlation density matrices for one-dimensional quantum chains based on the density matrix renormalization group", *New Journal of Physics* **12**(7), 075027 (2010).
- [20] R. Bulla, H.-J. Lee, N.-H. Tong and M. Vojta, "Numerical renormalization group for quantum impurities in a bosonic bath", *Phys. Rev. B* **71**(4), 045122 (2005).
- [21] M. B. Plenio, J. Eisert, J. Dreißig, and M. Cramer, "Entropy, entanglement, and area: Analytical results for harmonic lattice systems", *Phys. Rev. Lett.* **94**, 060503 (2005).
- [22] T. Barthel, M.-C. Chung, and U. Schollwöck, "Entanglement scaling in critical two-dimensional fermionic and bosonic systems", *Phys. Rev. A* **74**, 022329 (2006).
- [23] N. Schuch, M. M. Wolf, F. Verstraete, and J. I. Cirac, "Entropy scaling and simulability by matrix product states", *Phys. Rev. Lett.* **100**, 030504 (2008).
- [24] K. G. Wilson and J. Kogut, "The renormalization group and the epsilon expansion", *Physics Reports* **12**(2), 75-199 (1974).
- [25] H. R. Krishna-murthy, J. W. Wilkins and K. G. Wilson, "Renormalization-group approach to the Anderson model of dilute magnetic alloys. I. Static properties for the symmetric case", *Phys. Rev. B* **21**, 1003-1043 (1980).
- [26] B. A. Jones and C. M. Varma, "Study of two magnetic impurities in a Fermi gas", *Phys. Rev. Lett.* **58**, 843-846 (1987).
- [27] F. B. Anders and A. Schiller, "Real-time dynamics in quantum-impurity systems: A time-dependent numerical renormalization-group approach", *Phys. Rev. Lett.* **95**, 196801 (2005).
- [28] A. Weichselbaum and J. von Delft, "Sum-rule conserving spectral functions from the numerical renormalization group" *Phys. Rev. Lett.* **99**, 076402 (2007).
- [29] C. Latta, F. Haupt, M. Hanl, A. Weichselbaum, M. Claassen, W. Wuester, P. Falahi, S. Faelt, L. Glazman, J. von Delft, H. Türeci, and A. Imamoglu, "Quantum quench of Kondo correlations in optical absorption" *Nature* **474**(7353), 627-630 (2011).
- [30] M. Vojta, N.-H. Tong, and R. Bulla, "Erratum: Quantum phase transitions in the subohmic spin-boson model: Failure of the quantum-classical mapping [*phys. rev. lett.* 94, 070604 (2005)]", *Phys. Rev. Lett.* **102**, 249904 (2009).
- [31] A. Weichselbaum, F. Verstraete, U. Schollwöck, J. Cirac, and J. von Delft, "Variational matrix product state approach to quantum impurity models" arXiv preprint condmat/0504305, (2005).

- [32] A. Weichselbaum, "Discarded weight and entanglement spectra in the numerical renormalization group", *Phys. Rev. B* **84**, 125130 (2011).
- [33] S. Kirchner, K. Ingersent, and Q. Si, "Quantum criticality of the sub-ohmic spin-boson model", *Phys. Rev. B* **85**, 075113 (2012).
- [34] S. R. White, "Density-matrix algorithms for quantum renormalization groups", *Phys. Rev. B* **48**, 10345-10356 (1993).
- [35] K. A. Kallberg, "Density-matrix algorithm for the calculation of dynamical properties of low-dimensional systems", *Phys. Rev. B* **60**, 335-343 (1995).
- [36] T. D. Kuehner and S. R. White, "Dynamical correlation functions using the density matrix renormalization group", *Phys. Rev. B* **60**, 335-343 (1999).
- [37] R. J. Bursill, T. Xiang, and G. A. Gehring, "The density matrix renormalization group for a quantum spin chain at non-zero temperature", *Journal of Physics: Condensed Matter* **8**(40), L583 (1996).
- [38] X. Wang and T. Xiang, "Transfer-matrix density-matrix renormalization-group theory for thermodynamics of one-dimensional quantum systems", *Phys. Rev. B* **56**, 5061-5064 (1997).
- [39] S. R. White, "Spin gaps in a frustrated Heisenberg model for CaV4O9", *Phys. Rev. Lett.* **77**, 3633-3636 (1996).
- [40] S. R. White and D. J. Scalapino, "Energetics of domain walls in the 2d t-J model", *Phys. Rev. Lett.* **81**, 3227-3230 (1998).
- [41] V. Murg, F. Verstraete, O. Legeza, and R. M. Noack, "Simulating strongly correlated quantum systems with tree tensor networks", *Phys. Rev. B* **82**, 205105 (2010).
- [42] S. Depenbrock, I. P. McCulloch, and U. Schollwöck, "Nature of the spin-liquid ground state of the $s = 1/2$ Heisenberg model on the Kagome lattice", *Phys. Rev. Lett.* **109**, 067201 (2012).
- [43] S. Rommer and S. Östlund, "Class of ansatz wave functions for one-dimensional spin systems and their relation to the density matrix renormalization group", *Phys. Rev. B* **55**, 2164-2181 (1997).
- [44] H. Takasaki, T. Hikihara, and T. Nishino, "Fixed point of the finite system DMRG", *Journal of the Physical Society of Japan* **68**(5), 1537-1540 (1999).
- [45] H. Saberi, A. Weichselbaum, and J. von Delft, "Matrix-product-state comparison of the numerical renormalization group and the variational formulation of the density-matrix renormalization group", *Phys. Rev. B* **78**, 035124 (2008).
- [46] F. Güttge, "Real-Time Dynamics and Critical Phenomena of Quantum Impurity Systems", PhD thesis, TU Dortmund, (2012).
- [47] C. Zhang, E. Jeckelmann, and S. R. White, "Density matrix approach to local hilbert space reduction", *Phys. Rev. Lett.* **80**, 2661-2664 (1998).
- [48] F. B. Anders, Private communication, (2013)
- [49] U. Weiss, "Quantum Dissipative Systems", (World Scientific, Singapore, 1993).

- [50] M. Xiao, "Theory of transformation for the diagonalization of quadratic Hamiltonians", arXiv, 09080787 (2009)
- [51] A. O. Caldeira and A. J. Leggett, "Influence of dissipation on quantum tunneling in macroscopic systems" *Phys. Rev. Lett.* **46**, 211-214 (1981).
- [52] J. E. Mooij, T. P. Orlando, L. Levitov, L. Tian, C. H. van der Wal, and S. Lloyd, "Josephson persistent-current qubit", *Science* **285**(5430), 1036-1039 (1999).
- [53] Y. Makhlin, G. Schön, and A. Shnirman, "Quantum-state engineering with josephson-junction devices", *Rev. Mod. Phys.* **73**, 357-400 (2001).
- [54] A. Recati, P. O. Fedichev, W. Zwerger, J. von Delft, and P. Zoller, "Atomic quantum dots coupled to a reservoir of a superfluid bose-einstein condensate", *Phys. Rev. Lett.* **94**, 040404 (2005).
- [55] D. Porras, F. Marquardt, J. von Delft, and J. I. Cirac, "Mesoscopic spin-boson models of trapped ions", *Phys. Rev. A* **78**, 010101 (2008).
- [56] M. Vojta, "Numerical renormalization group for the sub-ohmic spin-boson model: A conspiracy of errors", *Phys. Rev. B* **85**, 115113 (2012).
- [57] B. Bruognolo, "Dynamical and Critical Properties of Bosonic Quantum Impurity Models", Master thesis, LMU Munich, (2013).
- [58] E. Luijten and H. W. J. Blöte, "Classical critical behavior of spin models with long-range interactions", *Phys. Rev. B* **56**, 8945-8958 (1997).
- [59] R. Marcus and N. Sutin, "Electron transfers in chemistry and biology", *Biochimica et Biophysica Acta (BBA) - Reviews on Bioenergetics* **811**(3), 265-322 (1985).
- [60] M. Vojta, C. Buragohain, and S. Sachdev, "Quantum impurity dynamics in twodimensional antiferromagnets and superconductors", *Phys. Rev. B* **61**, 15152-15184 (2000).

Acknowledgment

At the end of this Master thesis I wish to thank all those who supported me in one way or another. Special thanks go to following people:

1. First and most of all, I want to thank my supervising tutor Benedikt Bruognolo for all the small and big discussions during my year in this group. He was always a great help when I had problems with numerics, physics or my motivation. Furthermore, I want to thank him for his brave proofreading of the whole thesis.
2. I want to thank Jan von Delft for giving me the opportunity to write my Master thesis in his group and the ideas and work he put into my master thesis and Andreas Weichselbaum for the enlightening and helping discussions about numerics.
3. I want to thank Frithjof Anders for offering to collaborate on his unpublished idea of OWC.
4. Frauke Schwarz for her help concerning technical stuff and her patience when I was talking with Benedikt in the same office. And of course the whole group for the friendly, funny and helpful atmosphere during breaks and working hours. I felt always welcome.
5. Finally, my family and close friends who always supported me during my studies.

Statement of Authorship

I hereby certify that this thesis is the result of my own work. Used material from published or unpublished work of others is referenced clearly in the text.

München, September 22, 2014